

ALMA MATER STUDIORUM - UNIVERSITY DI BOLOGNA

---

ARCES - Advanced Research Center on Electronic Systems for  
Information and Communication Technologies “Ercole De Castro”

European Doctorate in Information Technology

Cycle XXV

09/G2 - Bioengineering; ING-INF/06

**SOLUTIONS TO COMMON ISSUES IN WIDEFIELD  
MICROSCOPY: VIGNETTING, MOSAICING  
AND DEPTH OF FOCUS**

**Filippo Piccinini**

*Coordinator*

**Prof. Claudio Fiegna**

*Tutor*

**Prof. Alessandro Bevilacqua**

*Co-Tutor*

**Prof. Mauro Ursino**

PhD course: January 1, 2010 - December 31, 2012

---

Final exam: April 19, 2013



*To Fabrizia (my mother), Lamberto (my father), Alessandra (my girlfriend).*



*When a door closes, another gate opens.*

*Si chiude una porta, si apre un portone.*

(Bruno Fabbrini)



External reviewers for the title of *Doctor Europaeus*:

Prof. **Emanuele Trucco**, University of Dundee, Scotland,  
email: manueltrucco@computing.dundee.ac.uk

Prof. **Walter G. Kropatsch**, Vienna University of Technology, Austria,  
email: krw@prip.tuwien.ac.at



# Keywords

IMAGE PROCESSING

FLUORESCENCE MICROSCOPY

BRIGHT FIELD

PHASE CONTRAST

BIOMEDICAL IMAGING



# Abstract (English version)

In this thesis we have studied and developed solutions to common issues regarding *widefield microscopes*, facing the common problem of the intensity inhomogeneity of an image and dealing with two strong limitations: the impossibility of acquiring either high detailed images representative of whole samples or deep 3D objects.

First, we cope with the problem of the non-uniform distribution of the light signal inside a single image, named *vignetting*, making the objects of the image hardly comparable. In particular we proposed, for both light and fluorescent microscopy, non-parametric multi-image based methods, where the vignetting function is estimated directly from the sample without requiring any prior information. After getting flat-field corrected images, we studied how to fix the problem related to the limitation of the field of view of the camera, so to be able to acquire large areas at high magnification. To this purpose, we developed *mosaicing* techniques capable to work on-line. Starting from a set of overlapping images manually acquired, we validated a fast registration approach to accurately stitch together the images previously flat-field corrected. Finally, we worked to virtually extend the field of view of the camera in the third dimension (i.e., the  $z$ -dimension), with the purpose of reconstructing a single image completely in focus, stemming from objects having a relevant depth or being displaced in different focus planes. To pursue this goal, a stack of images is typically acquired by scanning the objects in  $z$ . Several methods have been proposed in literature to estimate the in-focus regions in each image of the stack to reconstruct one image completely in focus. After studying the existing approaches for extending the *depth of focus* of the microscope, we proposed a general method that does not require any prior information. In order to compare the outcome of existing methods, different standard metrics (Universal Quality Index, Signal to Noise Ratio and Mean

Squared Error) are commonly used in literature, applied on stacks of synthetic images endowed with ground truth. However, no metric is available in real cases to compare different methods, where a reference ground truth is not at one's disposal. First, we validated a metric able to rank the methods as the Universal Quality Index does, but without needing any reference ground truth. Second, we proved that the approach we developed performs better in both synthetic and real cases.

The thesis contains data and methods that we have partly published in 3 scientific journals and 6 international conference proceedings. All the source codes and related material are achievable upon request.

# Abstract (Italian version)

In questa tesi abbiamo studiato e sviluppato soluzioni a questioni comuni in materia di *microscopia a campo largo*. In particolare abbiamo affrontato il problema della non omogeneità dell'intensità delle immagini acquisite e due forti limitazioni: l'impossibilità di acquisire immagini ad alto dettaglio rappresentative o dell'intero campione o di oggetti 3D con spessore non trascurabile.

Per prima cosa abbiamo studiato le caratteristiche del problema denominato *vignettatura*, relativo alla distribuzione non uniforme del segnale di luce all'interno di ogni singola immagine che rende gli oggetti presenti difficilmente paragonabili. In particolare abbiamo proposto, sia per la microscopia a luce sia per la microscopia a fluorescenza, metodi non parametrici dove la funzione di vignettatura è stimata utilizzando un insieme di immagini acquisite direttamente dal campione, senza richiedere alcuna informazione aggiuntiva. Dopo aver sviluppato metodi per ottenere immagini con distribuzione uniforme di intensità, abbiamo studiato come risolvere il problema legato alla limitata dimensione del campo di vista della telecamera, al fine di essere in grado di acquisire una singola immagine ad alto ingrandimento rappresentativa dell'intera area del campione osservato. A questo scopo abbiamo sviluppato tecniche di *mosaicatura* in grado di operare on-line con l'acquisizione delle immagini. Partendo da una serie di immagini acquisite manualmente, avendo cura che ci fosse sempre una certa percentuale di sovrapposizione tra due immagini seguenti, abbiamo validato un approccio di registrazione in grado di creare velocemente un mosaico allineando accuratamente le singole immagini acquisite, precedentemente corrette dall'effetto di vignettatura. Infine, abbiamo studiato come estendere virtualmente il campo di vista della telecamera lungo la terza dimensione (la dimensione  $z$ ), con lo scopo di poter ottenere singole immagini completamente a fuoco o di oggetti aventi uno spessore rilevante o di un insieme di oggetti posizionati su differenti piani di messa a fuoco. Gen-

eralmente, per raggiungere questo obiettivo una sequenza di immagini viene acquisita scansionando in  $z$  gli oggetti e diversi metodi sono stati proposti in letteratura per stimare prima le regioni a fuoco in ogni singola immagine e a seguito per ricostruire l'immagine completamente a fuoco sfruttando le regioni a fuoco precedentemente identificate. Dopo aver studiato i vari approcci esistenti per estendere la ***profondità di messa a fuoco*** del microscopio, abbiamo proposto un metodo generale che non richiede alcuna informazione a priori. Per confrontare i risultati dei diversi metodi, in letteratura sono tipicamente usate diverse metriche comuni (indice di qualità universale, rapporto segnale rumore ed errore quadratico medio) sfruttando immagini sintetiche dotate di verità di riferimento. Tuttavia nessuna metrica in grado di confrontare diversi metodi analizzando i risultati ottenuti usando immagini reali dove non è presente l'immagine di verità. In primo luogo abbiamo validato una metrica in grado di classificare i diversi metodi in accordo all'indice di qualità universale ma senza bisogno di alcuna verità di riferimento. Poi, sfruttando la metrica validata e sequenze di immagini sintetiche, abbiamo dimostrato che il metodo che abbiamo sviluppato risulta essere il migliore tra tutti quelli testati per estendere la profondità di messa a fuoco.

Questa tesi contiene dati e metodi in parte già pubblicati in 3 riviste scientifiche e 6 atti di conferenze internazionali. Tutto il materiale citato, compreso il codice sorgente dell'implementazione dei metodi, è fornito su richiesta.

# Contents

<b>Abstract (English version)</b>	<b>xi</b>
<b>Abstract (Italian version)</b>	<b>xiii</b>
<b>Contents</b>	<b>xv</b>
<b>1 Introduction and thesis overview</b>	<b>1</b>
<b>2 Vignetting in light microscopy</b>	<b>9</b>
2.1 Introduction . . . . .	10
2.2 State of the art . . . . .	14
2.3 Methods . . . . .	18
2.3.1 Background segmentation . . . . .	21
2.3.2 Dense background reconstruction . . . . .	22
2.4 Materials and tools . . . . .	23
2.5 Experimental results . . . . .	24
2.5.1 Quality of the background segmentation . . . . .	25
2.5.2 Vignetting function of image number and confluence . . . . .	28
2.5.3 Comparison of shapes of different vignetting functions . . . . .	30
2.5.4 Flat-field correction on single images . . . . .	32
2.5.5 Flat-field correction on mosaics . . . . .	35
2.6 Conclusion and future work . . . . .	41
2.6.1 Conclusion . . . . .	41
2.6.2 Future work . . . . .	43
2.7 Acknowledgments . . . . .	44
2.8 Copyright permission . . . . .	44
<b>3 Vignetting in fluorescence microscopy</b>	<b>47</b>
3.1 Introduction . . . . .	48

3.2	Methods compared in the experiments . . . . .	53
3.3	Materials . . . . .	56
3.4	Method based on linear correction . . . . .	58
3.4.1	Background modelling . . . . .	58
3.4.2	Vignetting estimation . . . . .	59
3.4.3	Linear flat-field correction . . . . .	61
3.5	Method based on non-linear correction . . . . .	62
3.5.1	Photobleaching modelling . . . . .	64
3.5.2	Vignetting functions estimation . . . . .	65
3.5.3	Non-linear flat-field correction . . . . .	66
3.6	Experimental results . . . . .	67
3.6.1	Flatness of the foreground signal . . . . .	68
3.6.2	Flatness of the whole images . . . . .	71
3.7	Conclusion and future work . . . . .	77
3.7.1	Conclusion . . . . .	77
3.7.2	Future work . . . . .	79
3.8	Acknowledgments . . . . .	80
<b>4</b>	<b>Mosaicing</b>	<b>81</b>
4.1	Introduction . . . . .	82
4.2	State of the art . . . . .	85
4.3	Methods . . . . .	91
4.3.1	Pre-processing . . . . .	91
4.3.2	Feature Detection . . . . .	93
4.3.3	Feature Matching . . . . .	95
4.3.4	Warping Model Estimation . . . . .	97
4.3.5	Image Warping and Stitching . . . . .	100
4.4	Materials . . . . .	102
4.5	Metrics . . . . .	105
4.6	Experimental results . . . . .	108
4.6.1	Flat-field correction . . . . .	108
4.6.2	F2M registration . . . . .	110
4.6.3	Warping models . . . . .	111
4.6.4	Results using the histological specimen . . . . .	114
4.6.5	Histological sample versus cell culture . . . . .	117
4.6.6	Computational performance . . . . .	118
4.7	Conclusion and future work . . . . .	119
4.7.1	Conclusion . . . . .	119

4.7.2	Future work . . . . .	120
4.8	Acknowledgments . . . . .	121
<b>5</b>	<b>Depth of focus</b>	<b>125</b>
5.1	Introduction . . . . .	126
5.2	State of the art . . . . .	129
5.3	Methods . . . . .	131
5.4	Quality metrics . . . . .	134
5.5	Materials . . . . .	136
5.6	Experimental results . . . . .	139
5.6.1	Experiments with the synthetic stacks . . . . .	140
5.6.2	Analysis of metrics for real stacks . . . . .	141
5.6.3	Experiments with real stacks . . . . .	144
5.7	Conclusion and future work . . . . .	145
5.7.1	Conclusion . . . . .	145
5.7.2	Future work . . . . .	147
5.8	Acknowledgments . . . . .	147
5.9	Copyright permission . . . . .	148
<b>6</b>	<b>Conclusion</b>	<b>149</b>
	<b>Appendix</b>	<b>153</b>
	Phase correlation . . . . .	153
	RANSAC . . . . .	156
	<b>List of figures</b>	<b>159</b>
	<b>List of tables</b>	<b>161</b>
	<b>Bibliography</b>	<b>163</b>
	<b>Personal publications</b>	<b>183</b>
	<b>Thanks</b>	<b>185</b>



# Chapter 1

## Introduction and thesis overview

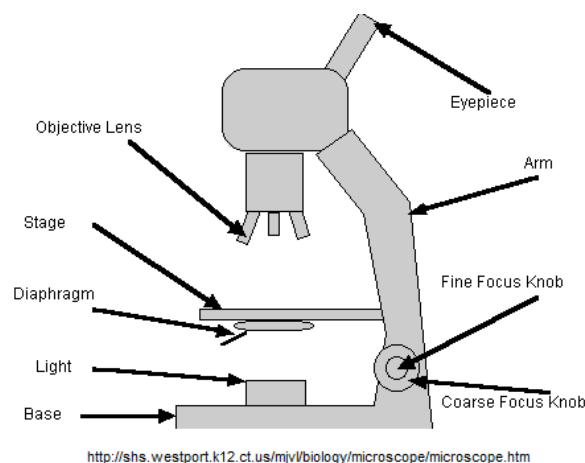


**Fig. 1.1:** Widefield microscope. Schematic representation of the principal components

Nowadays, the extent of human knowledge is widening by managing from macro to nano. In the infinite big, we are able to remotely drive a robot to collect materials on Mars. In the infinite small, we manage the human DNA to prevent severe illness. In particular, these great goals of the humanity are brought from a general improvement on every contributing science. And there is a common fundamental line in the improvement of every single science: the possibility to perform measurements. This is the fundamental key point of the

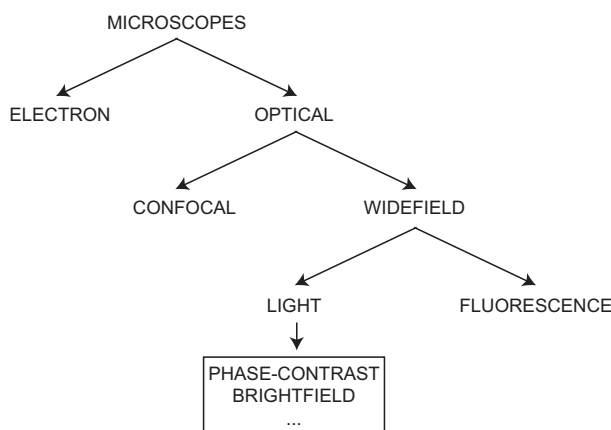


**Fig. 1.2:** Microscopes taxonomy. Simplified schematic tree diagram of common microscope types

general knowledge improvement. Measuring a phenomenon, we become able to study, and often also to control and modify that phenomenon. In particular, in this thesis we focus our attention on one limit of the human knowledge, the infinite small, where there is a main instrument of measurement: the microscope (Fig. 1.1) [1].

Lens systems and microscopes are used in science from the sixteenth century, always increasing their magnification capabilities [2]. Now, in the twenty-first century, we are in the middle of two Ages of microscopes: the Age of micro and the Age of nano. The magnification factor has become so high that we can look into a single micro cell and study nano particles [3]. Furthermore, so many variants of microscopes have been realized that is also difficult to define a proper taxonomy [4]. In Fig. 1.2 a simplified schematic tree diagram is proposed, organized in the upper part accordingly to the technology, then to the imaging techniques.

As expected, there is not a general microscopy technique suitable for all purposes [5]. Before choosing the microscope fulfilling our requirements, we need to define our goal: what do we want to see. For instance, looking at a high magnification the cell shape does not help for defining an animal species (Fig. 1.3). Accordingly, the wide range of different microscopes available is the answer to visualize different particular characteristics of the substances. Nevertheless, despite the wide availability of many different microscopes and the new technology continuously improving the performance of devices, there are still

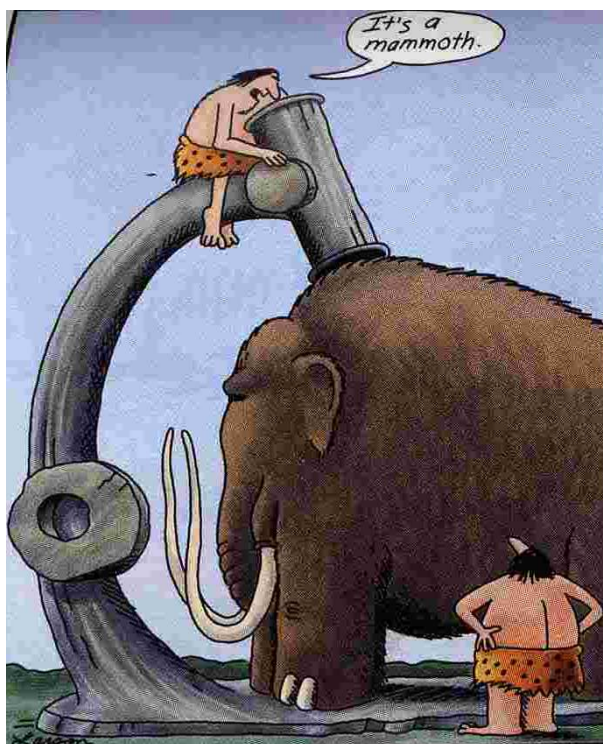


**Fig. 1.3:** Microscope and measure. The choice of the measurement instrument is always tight to what we want to measure. Cartoon by Gary Larson.

problems and limitations that have to be faced [6].

In this thesis, we focus our attention on optical widefield microscopy, the most present in biological laboratories. This class of microscopes can be subdivided into more groups according to the illumination source used to visualize the substance (Fig. 1.4), typically rays of given wavelength in the human visible spectrum (Light Microscopy [7],  $700 \text{ nm} - 400 \text{ nm}$ ) or, more extensively, from the infrared to the ultra violet (Fluorescence Microscopy [8],  $1000 \text{ nm} - 1 \text{ nm}$ ). These microscopes are principally used in brightfield and phase-contrast [9] to visualize the morphology of micrometric cells and, in fluorescence, to highlight nanometric particles or cell structures. As far as the general widefield microscopy is concerned, limitations are often related to the area's extension achievable in one single image at the desired resolution and to the visualization of deep objects, characterized by a relevant  $z$ -dimension (e.g., large 3D multicellular aggregates). Moreover, there are problems arising from the uneven distribution of the signal in the field of view. Furthermore, specifically in fluorescence microscopy, problems such as photo-bleaching and quenching effect

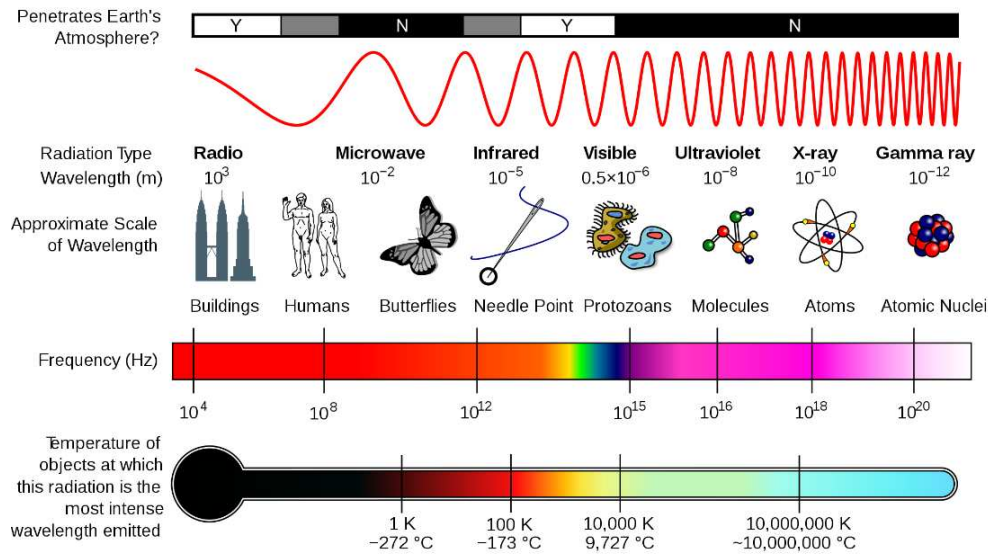


**Fig. 1.4:** Light spectrum. The Human visible light is between  $700 \text{ nm}$  -  $400 \text{ nm}$ .  
From Wikipedia: electromagnetic spectrum.

limit the concept to consider a microscope an instrument of measurement. The lofty objective of this thesis and of all the methods generally proposed in literature to fix problems or relax limitations, is to improve technology, techniques and knowledge in order to make the microscope more and more an accurate quantity measuring system [10].

This thesis deals with three main common issues of the widefield microscopy:

- correction for the uneven distribution of the signal
- acquisition of an image of a large area at a high magnification
- visualization of deep objects

The keywords related to these issues are respectively: *vignetting*, *mosaicing* and *depth of focus*.

**VIGNETTING:** the uneven fall-off of the image intensity (Fig. 2.1). This problem affects all the images acquired with a widefield microscope, making the distribution of the signal non homogeneous. If no correction is accomplished, the images are almost useless for quantitative analyses. Often, to correct for

vignetting, reference images are acquired in advance to characterize the signal distribution and use the function estimated as a normalization factor. Nevertheless, several reasons make this solution infeasible. The vignetting problem is analyzed in both light (brightfield and phase-contrast) and fluorescence microscopy and multi-image based methods to estimate the vignetting function from the sample itself are proposed.

**MOSAICING:** the stitching of a set of images aiming at virtually extending the limited field of view of the camera (Fig. 4.1). The final result is a mosaic having at least the same pixel resolution of the source images and a large final represented area. Mosaicing is a very common technique, used in many applications such as panoramic photography, satellite imaging and biological applications. Accordingly, many methods are proposed in literature to obtain accurate mosaics in microscopy. Several of them relied on priors, like the shifts between the images. A non-parametric method is proposed to stitch together images manually acquired with a standard widefield microscope, even though not coupled with a motorized  $x$ - $y$  stage.

**DEPTH OF FOCUS:** key parameter of optical system, sometimes also called *depth of field* (Fig. 5.1). In the data sheet of the lens, it is normally expressed in  $\mu\text{m}$ . It represents the distance between focal planes in the  $z$ -dimension, where objects keep sharp or *in focus*. An object is considered in focus when it is particularly sharp, clear and, in general, good-looking. This parameter is a strong limitation for the system, because it makes the acquisition of sharp images of deep objects infeasible. Several methods are proposed in literature to overcome this limit, but it is particularly difficult to compare the results due to the lack of the “ground truth”, that is a gold standard assumed to be the “truth”. In particular, a metric based on the Universal Quality Index that does not require the ground truth is validated. Then, the methods at the state of the art are compared meanwhile proposing a new solution that does not require prior information on the images acquired nor heavy computational burden.

This thesis is organized as follows:

Chapter 2 discusses the vignetting problem in all the details regarding light microscopy. After an introduction on causes and effects, the state-of-the-art methods are presented and compared. Then, a multi-image based method to

estimate the vignetting function from the sample itself is proposed, overcoming the other approaches considered.

In Chapter 3 the vignetting is analyzed in fluorescence microscopy. Usually, problems like photobleaching, quenching and background behaviour make the methods proposed in light microscopy ineffective. After an exhaustive analysis of the available solutions, two different methods to correct the images by the vignetting effect are proposed. In the first one, the vignetting function is estimated from a large set of images acquired in advance. In the second one, an ensemble of vignetting functions (instead of a single one) is estimated (registering a set of overlapping images) and a non linear correction is proposed instead of the linear one commonly used.

Chapter 4 presents the mosaicing technique as a solution to easily extend the field of view of digital cameras coupled with microscopes. In particular, although the images are acquired with a microscope not coupled with a motorized  $x$ - $y$  stage, the proposed general purpose registration approach works at subpixel, yielding highly accurate mosaics. The focus of this work it is not necessarily the advancing of the state of the art. Rather, it represents a functional stage for testing the different vignetting correction approaches. Nevertheless, at the same time a solution for building mosaics on-line using non-automated microscopes is proposed.

Chapter 5 is related to the depth-of-focus parameter. It is presented as a strong constraint of the microscopes for a certain type of biological analyses. A pretty fast method to extend the depth of focus is proposed. Furthermore, a new metric is proposed to compare the state-of-the-art methods without requiring the ground truth, typically not at one's disposal.

Concluding remarks and hints for possible future work are reported and discussed in Chapter 6.

The work developed in this thesis has been carried out with the:

- Computer Vision Group (CVG), II Faculty of Engineering, University of Bologna, Bologna, Italy. Director: Dr. Alessandro Bevilacqua

in partnership with the following institutions and laboratories:

- Osteoarticular Regeneration Laboratory, Rizzoli Orthopaedic Institute (IOR), Bologna, Italy. Director: Dr. Enrico Lucarelli
- Laboratory of Biosciences, Istituto Romagnolo per lo Studio e la cura dei Tumori (IRCCS-IRST), Meldola (Forlì-Cesena), Italy. Director: Dr. Wainer Zoli
- Laboratory of Radiobiology, Istituto Romagnolo per lo Studio e la cura dei Tumori (IRCCS-IRST), Meldola (Forlì-Cesena), Italy. Director: Dr. Anna Tesei
- Light Microscopy and Screening Center, Eidgenössische Technische Hochschule Zürich (ETHZ), Zurich, Switzerland. Responsible of Image Processing: Dr. Peter Horvath

the activities have been carried out in the following two projects:

- STAMINAL - characterization of STem cells through support for Automatic analysis of the MIcroscopic images in pre-clINicAL therapy (partially granted by IRCCS-IRST)
- ADVANCE - Automatic non-invasive system based on high content analysis to Detect and characterize VitAl meseNchymal stem Cells in a spatio-temporal contExt (partially granted by IOR)

In particular, I spent the first year for implementing and validating the mosaicing technique, then used to test the different vignetting correction approaches. In the following two years I have deeply explored the research field of vignetting correction in both light and fluorescent microscopy, yielding to innovate the state of the art. In the same time, I worked on the field of the extension of depth of focus for the visualization of deep objects, comparing the existing approaches and proposing a new effective solution. The developed methods and the obtained data have been partly published in 3 scientific journals and are presented in 6 international conference proceedings. All the source codes and related material are distributable upon request [11].

The 3-year PhD course in Information Technology was granted by the Advanced Research Center on Electronic Systems (ARCES), University of Bologna, Italy.



# Chapter 2

## Vignetting in light microscopy

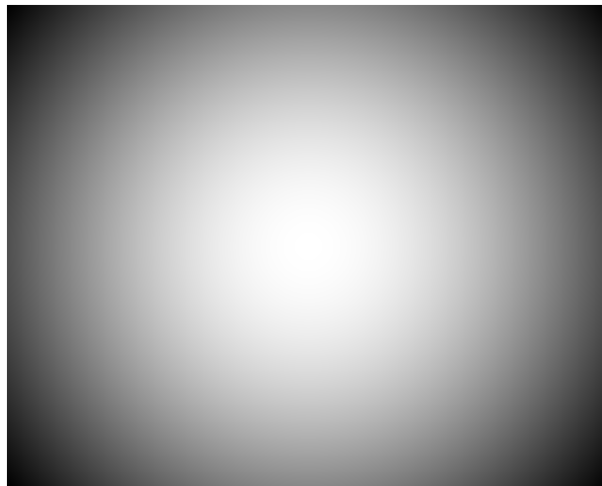


**Fig. 2.1:** Vignetting effect. Inhomogeneous distribution of the image intensity.

- F. Piccinini, E. Lucarelli, A. Gherardi, A. Bevilacqua, Multi-image based method to correct vignetting effect in light microscopy images. *Journal of Microscopy*, 248(1): 6-22, 2012
- A. Bevilacqua, F. Piccinini, Is an empty field the best reference to correct vignetting in microscopy? *7<sup>th</sup> International Workshop on Biosignal Interpretation (BSI)*, Como, Italy, July 2-4, 2012, pp. 267-270
- A. Bevilacqua, F. Piccinini, A. Gherardi, Vignetting correction by exploiting an optical microscopy image sequence. *33<sup>rd</sup> International Conference of the IEEE Engineering in Medicine and Biology Society (EMBS)*, Boston, USA, August 30-September 3, 2011, pp. 6166-6169
- A. Gherardi, A. Bevilacqua, F. Piccinini, Illumination field estimation through background detection in optical microscopy. *8<sup>th</sup> Annual IEEE Symposium on Computational Intelligence in Bioinformatics and Computational Biology (CIBCB)*, Paris, France, April 11-15, 2011, pp. 49-54

## 2.1 Introduction

Nowadays, light microscopes coupled with digital cameras are part of the ordinary basic equipment of all biological laboratories, where most of the biological routine examinations regard cell cultures and histological samples. The accuracy of the microscope system, meant as an ensemble of illumination source, condenser, filters, lens and camera sensors, has become particularly high even using cheap components, this making quantitative imaging examinations enter in daily routine [10]. Accordingly, great benefits in the biology research can derive from improvements in the image acquisition system as corrections of early errors still present [12].

Typically, the images acquired with light microscopes are characterized by a radial fall-off of brightness intensity from the principal point towards the image borders [13]. This undesirable property, intrinsic to optical systems, is known as vignetting and represents one of the most common early problems that affects digital imaging [14] and, in particular, subsequent processing stages such as segmentation [15] and object tracking [16]. The problem is far more emphasized in quantitative imaging, where taking into account the vignetting effect is mandatory to achieve reliable intensity measurements [17] or to compare images achieved in subsequent times [18]. From a visual point of view, the problem becomes particularly evident in mosaicing, where several images are stitched together to fix the problem related to the narrowness of the field of view of the camera [19, 20]. In fact, the registered images are not corrected for vignetting effects, the seams in the stitching zones become clearly notable [21], misleading visual and automated analysis [22, 23].

The ideal condition to have a negligible vignetting effect is called Köhler illumination [24, 25]. However, in real cases, many sources of vignetting contribute to find a fall-off of the image intensity [26]. In [27] are reported the main sources of vignetting classified according to the following four sources.

**Natural vignetting**, radial falloff due to geometric optics. Different regions of the image plane receive different irradiance. For simple lenses, these effects are sometimes modeled as a falloff of  $\cos^4(\theta)$  [28, 29], where  $\theta$  is the angle at which the light exits from the rear of the lens. Note that in all lenses, the distance from the exit pupil to the image plane changes when the focus distance is changed, so this component varies with focus distance. The  $\cos^4$  law is only

an approximation which often could not be enough to model properly camera and lenses in real applications.

**Pixel vignetting**, radial falloff due to the angular sensitivity of digital optics. This type of vignetting, which affects only digital cameras, is due to the finite depth of the photon wells in digital sensors, which causes light striking a photon well at a steeper angle to be partially occluded by the sides of the well.

**Optical vignetting**, radial falloff due to light paths blocked inside the lens body by the lens diaphragm. It is also known as artificial or physical vignetting. This is easily observed by the changing shape of the clear aperture of the lens as it is viewed from different angles, which reduces the amount of light reaching the image plane. Optical vignetting is a function of aperture width: It can be reduced by stopping down the aperture, since a smaller aperture limits light paths equally at the center and edges of frame. Some lens manufacturers provide relative illuminance charts that describe the compound effects of natural and optical vignetting for a fixed setting of each lens.

**Mechanical vignetting**, radial falloff due to certain light paths becoming blocked by other camera elements, generally filters or hoods attached to the front of the lens body.

To summarize, the term vignetting refers to radial falloff from many sources (sketched in Fig. 2.2). In light microscopy, the non-uniformity of the light rays, the interaction between light and sample, dust on the lens and lens's impurities, misalignments of components, angular sensitivity of the digital sensor and its response function, altogether alter the ideal effect of vignetting over the acquired image.

In the last decades, with the increase of microscopy image analyses, many approaches have been proposed to correct the effect of vignetting. The extensive list of methods is reported in Sect. 4.2. Each of them relies on some constraints or prior information and there is no general solution to fix the problem.

The most trivial but common approach is acquiring in advance an image of a homogeneous reference object. The curvature of the brightness intensity, perceptible in the captured images, can be considered a direct representation of the vignetting function and used to calibrate the system. To this purpose, images of Empty Field (EF) are typically used in light microscopy [30, 31].

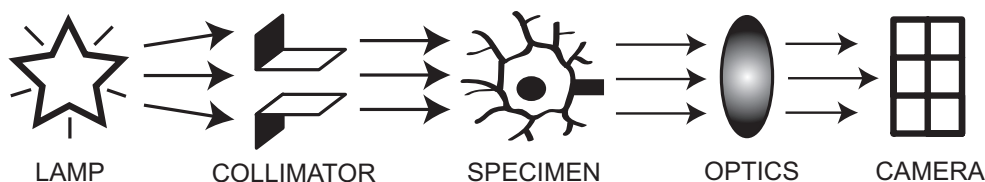


**Fig. 2.2:** Vignetting sources. In light widefield microscopy the light flow can be sketched as so: the light rays arising from a source, typically a standard lamp, are collimated to obtain a more flat wavefront to illuminate the specimen. After the light-sample interaction, the rays transmitted through optics (like the lens of the objective) reach the sensor of the image acquisition system, typically a CCD camera. Several sources of vignetting can be highlighted by analyzing the light flow: the light wavefront that reaches the specimen is not perfectly flat, the lens act according to the theoretical  $\cos^4$  law and the spatial sensitivity of the camera's sensor is not perfectly constant.

However, several reasons could make this approach difficult to apply [32, 31], besides considering that acquiring a reference image is an additional operation and it could be tricky for microscope users. First, the time elapsing between the acquisition of the image of the reference object and the subsequent images to be corrected could induce the systems conditions to change (e.g., due to drifts of some component) without the operators awareness. Also, a reference object could not be at one's disposal, for example, when using specific dyes in fluorescence microscopy or when the sequence to be corrected has been acquired elsewhere without any reference image. Finally, since acquiring a reference object and the target images must be accomplished in separate stages, freeing oneself from the need of using reference objects could open the door to useful applications. For example, in case of exploratory investigations of specimens, mosaicing could start at any time as soon as a region of interest is detected. On the contrary, it could be impracticable stopping the session, acquiring an EF and then retrieving the region of interest.

To overcome these problems, several methods have been devised which do not rely on reference images. Some approaches rely on parametric models and are typically grounded on theoretical and physical proprieties of the light distribution [33, 34], for example the  $\cos^4$  law of the scene radiance decreasing. However, this prior information neglects shape changes on the vignetting curve due to impurities on the lens, dust on lens, optical or mechanical non-idealities

like optical axis and holder being not perpendicular or the principal points not falling in the geometric center of symmetry of the image.

In order to include also the above mentioned sources of shape changes in vignetting estimation, several image based methods have been proposed. The most trivial ones are those based upon the assumption that the uneven illumination simply stems from an additive low frequency signal [14, 35]. Accordingly, low pass filtering techniques are proposed to extract such a signal from the image. Accordingly, they only work in situations where vignetting effects are very strong when compared to the range of the signal. Often, methods trying to estimate the vignetting function from a single image require the use of strong priors such as the radial symmetry of vignetting [36] or the center of the vignetting function coinciding with the numerical center of the image coordinates [37]. Furthermore, errors in crucial steps of the process, such as the segmentation of the image regions, lead to a large bias in the estimated vignetting function. Moreover, in some cases the information contained in the single image cannot be enough to estimate a dense vignetting function.

Using more images could permit to exploit more information, thus making the task to estimate the vignetting function faster [38], more reliable and more robust [39]. In fact, several multi-image based methods have been proposed to estimate the vignetting function starting from a sequence of images acquired under stable microscope set-up conditions. However, most of the approaches still rely on priors such as the need of overlapping views of an arbitrary static scene in order to have the same object acquired under different points of view [40, 27]. Accordingly, this restricts the applicability of these methods: as a matter of fact, only a few of them can be generically employed in widefield microscopy and even fewer can work in brightfield and phase contrast images characterized by a very low contrast [41, 42, 38, 43]. A more extensive analysis of these multi-image based methods is reported in Sect. 2.2.

In order to relax the priors of the methods analyzed, we propose a nonparametric multi-image based method, conceived for light microscopy applications even though the images are characterized by a very low contrast. The vignetting function is simply estimated starting from a sequence of images acquired under the same microscope setup conditions. It is computed over a background (consisting of regions free of interesting objects like cells or tissue) built incrementally using a background segmentation algorithm developed on purpose

and validated with extensive test experiments. The method is based on the assumption that the background is more homogeneous than the foreground. The estimated function is then used to correct the brightness intensity curvature of the images. It is worth noticing that no prior information about the microscope optics or the acquisition system is required. The method is then suitable to tackle the vignetting problem even in real-time applications. In fact, the images used to determine the vignetting function can be acquired after starting normal operators inspection activities, and then kept and corrected in their turn. For instance, this could be useful to build mosaics in real time. The experiments were carried out using both cell cultures and histological specimens, which cover the most relevant part of the biological routine examination performed with widefield microscopes. Also, a thorough and interesting comparison with results achieved using reference vignetting functions is discussed. Besides offering visual evaluation, we also propose a quantitative analysis using several different metrics that proves the effectiveness of our method in reducing vignetting: in fact, several times it results to be the best, even outperforming the correction based on EF.

## 2.2 State of the art

To face the vignetting effect many different approaches have been published. Each of them relies on some constraints or prior information. There is no a general solution to fix the vignetting problem in each case, but for every situation there are several paths that can be followed. In this section, different meaningful approaches to face the problem regarding vignetting and flat-field correction are listed. Not all of them are easily applicable in widefield microscopy (considering both light and fluorescence microscopy) and even less are suitable for real-time applications, in which reducing the computational time is an important goal. Despite that in this section we give an extensive overview.

Depending on how the vignetting function is estimated, we classify the methods into three groups:

- using a reference object

- single-image based methods
- multi-image based methods

If a reference object is used, the fundamental step is the acquisition of an additional image that is considered a direct representation of the vignetting function. Typically, more images regarding the reference object are acquired and the median surface is computed to estimate a robust vignetting function. The first group can be further subdivided into categories depending on the type of the reference object used:

- empty field [32, 30, 44, 45, 46, 31, 47, 48]
- calibration slide [49, 50, 51, 52, 53, 54, 55, 56, 57, 58, 59, 60, 61]
- specific homogeneous object(s) [62, 63, 64, 65, 66, 67, 68, 69, 70, 71]

In the second group, we insert the methods that use only the information contained in a single image to reconstruct the vignetting function. They can be subdivided in the following methods:

- simply based on filtering steps [14, 72, 73, 74, 35]
- using images to determine the parameters' values of a pre-fixed vignetting model [75, 76, 33, 77, 78, 34]
- using particular advanced image processing to determine the vignetting function, typically exploiting the information based on the brightness distribution of the intensity values in segmented image regions [72, 36, 37, 79, 80]

However, the limited data contained in a single image makes a reliable estimate of the vignetting function difficult to be constructed.

Finally, we report some important multi-image based methods. These methods are particularly interesting because typically they can reconstruct an estimate of the vignetting function that is more robust than the methods listed above, also just for collecting a better statistic using a set of several images instead a single one. We can subdivide the multi-image based methods into the following

subclasses:

- methods based on the fundamental assumption that the vignetting is a simple additive low frequency signal [41, 42, 39, 38]
- methods that reconstruct a dense background surface and use it as the vignetting function, supposing that the background expresses the same illumination pattern of the foreground [43, 81, 82]
- methods where advanced image processing are required to estimate the vignetting function extracting information from image objects and/or different regions [83, 40, 84, 27, 85, 86]

In particular, only few multi-image based methods could be actually employed in widefield microscopy, especially in fluorescence microscopy:

- Can *et al.* (2008) [41]: here, the percentage of the foreground in the image sequence is assumed to be known and even constant among the different images. Moreover, the foreground objects (considered as regions containing cells or tissues) are assumed similar and quite homogeneous and the foreground values always higher than the background ones. Exploiting these priors, the authors propose an algorithm to define whether each image value belongs to foreground or background. For each  $(x,y)$  position the vignetting function is then calculated by computing the mean value of the foreground pixels. Exploiting the same ideas and the input parameter regarding the percentage of foreground, the approach could be also extended to estimate the background surface as the mean value of the lower-intensity pixels. The approach sounds good, although requiring as a prior the knowledge of the percentage of foreground is strong assumption. Furthermore, the percentage of foreground is assumed pretty constant in each image. An error in the percentage evaluation could mislead the estimation of the vignetting and the background surfaces, taking into account for both foreground and background only the subset of the most noisy values (if the percentage of foreground is under estimated) or outliers (if the percentage of foreground is up-estimated). The code is not available, and no hints are given for parameters set up (e.g., the order of the polynomial fitting). Accordingly, a specific study of the parameters should be carried out to make the method work with one's

own images.

- Jones *et al.* (2006) [42]: in this work, a sequence of images is analyzed in  $z$  and the mean value for each  $(x,y)$  pixel position is suggested as a good estimation of the vignetting function. The same approach is also followed by Shariff *et al.* [38]. The fundamental assumption is that in the image sequences the percentage of background areas is negligible in comparison to the foreground. If this does not happen the method, being based on the search of the  $z$ -mean values, works only if the ranges of foreground and background values are both evenly distributed around the same mean value. Although this last condition could be true for some cell cultures, it rarely holds in histological specimens since the range of tissue values is far different from the range of background values and typically is not uniformly distributed. The method is implemented in CellProfiler, a free open source image analysis software widely used in the medical-biological field [87, 88].
- Vokes and Carpenter (2001) [43]: the presented method is conceptually really trivial, because it is based just on a simple background estimation stage, assuming that in fluorescence the background values are always the lowest ones in the images. Although this is true in fluorescence images, in brightfield and phase contrast microscopy imaging this is not necessarily granted. For example, in cell culture images acquired in brightfield or phase contrast, often cells show intensity values lower than values of culture medium. To estimate the vignetting function the images are divided in small regions and the background is reconstructed using the minimum value for each region. Then, it is supposed that the background shows the same illumination pattern as the foreground and the images are simply flat-field corrected using the reconstructed background surface. The method is implemented in CellProfiler and to correct the images the authors offer the choice of subtracting or dividing by the reconstructed background.
- Lindblad and Bengtsson (2001) [82]: the vignetting function is assumed to be proportional to the curvature of the background surface, reconstructed from each input image and finally obtained by averaging the single surfaces. The crucial step is the foreground/background segmentation performed using a global thresholding approach. The authors

proposed an interesting segmentation solution based on the analysis of the standard deviation of the image histogram, but its applicability depends on number and size of the foreground objects. To reconstruct the dense background surfaces the authors presented an iterative fitting technique based on cubic B-spline applied on the sparse grid of background values. The surface reconstruction becomes more robust by weighting pixels that more likely are background. Similar approaches are present in the literature to estimate the vignetting function simply by median filtering or by fitting a polynomial surface [39].

## 2.3 Methods

Starting from the general camera image model proposed in [85, 86, 40, 83, 27, 84], we define a generic image  $I$  according to Eq. 2.1:

$$I(x,y) = r(G \cdot V(x,y) \cdot L(x,y)) \quad (2.1)$$

where  $r$  is the camera response function,  $G$  is the camera gain due to exposure,  $V(x,y)$  is the spatially variant vignetting function,  $L(x,y)$  represents the power radiated from the scene and  $(x,y)$  is the pixel coordinate. In particular, in brightfield microscopy  $L$  is function of the transmitted light and in phase microscopy it is the transmitted light spatially modified by the phase shift due to the refractive index of the specimen. Without loss of generality,  $r$  is here considered as being linear and spatially invariant, although Eq. 2.1 can be easily generalized for nonlinear response functions.

If the vignetting function is perfectly known, to correct the acquired images dividing them for  $V$  is enough. This pixel-wise division is known as flat-field [66, 64, 65, 68, 6] or retrospective correction [13, 89] and Eq. 2.2 represents the general form of the flat-field correction formula in widefield microscopy.

$$I_{FFC}(x,y) = \frac{I(x,y) - B(x,y)}{V(x,y) - B_V(x,y)} \cdot NC \quad (2.2)$$

$I_{FFC}(x,y)$  is the output image flat-field corrected.  $I(x,y)$  is the original input image undergoing vignetting.  $V(x,y)$  is the vignetting function.  $B(x,y)$  and  $B_V(x,y)$  represent the “background noise” referred to  $I(x,y)$  and  $V(x,y)$ , re-

spectively. In light microscopy,  $B(x,y)$  and  $B_V(x,y)$  are typically coincident and they are constituted by the image acquired closing the camera's shutter [66]. Their values are orders of magnitude lower than  $I$  and  $V$  and for this reason they are often neglected [34, 72], as in the present work. Instead, in fluorescence microscopy typically  $B(x,y)$  is an image reconstructed from empty regions in the specimen without cells, while  $B_V(x,y)$  is the noise related to the object, or the matter, used to estimate  $V(x,y)$ . For instance, if  $V(x,y)$  has been estimated using a homogeneous fluorescence calibration slide,  $B_V(x,y)$  is an image from a non-fluorescent object (usually, water). Often,  $B$  and  $B_V$  are considered as being Gaussian noise and they are replaced in the formula by their mean value [66]. Also in fluorescence microscopy sometimes they could be of the same nature and range values, thus assuming  $B$  and  $B_V$  being coincident [47, 68]. Or else, in some applications they could be negligible with respect to  $I(x,y)$  and  $V(x,y)$  and they are neglected, accordingly [90, 63, 72]. In the remaining cases, these terms are erroneously not considered. Finally,  $NC$  is a Normalization Constant used to adjust the range of  $I_{FFC}$  [65] and it is often computed as the formula denominator's mean value [51, 91, 69] or the median value [81] or the mean value of the vignetting function only [47]. Hereafter,  $V_N$  is referred as the vignetting function normalized to its mean value. Furthermore, to enhance the contrast of  $I_{FFC}(x,y)$ , for example to avoid reduction of the range of values after the flat-field correction, a simple image stretching stage could be performed using the min-max values of  $I(x,y)$ . In practice, the formula is often used according to the information at one's disposal.

To estimate the vignetting function, we start by analyzing a sequence of images acquired under the same microscopes set-up conditions. Ideally, an image can be always subdivided into two complementary regions, foreground and background, where the foreground usually represents the objects of interest. In optical microscopy, as already mentioned, the main part of the routine examination is performed on cell culture or histological samples. Accordingly, as the foreground we consider cells and tissues and as the background culture medium and glass, respectively (Fig. 2.3). It is worth noticing that the background is widely homogeneous compared to the foreground and using a homogeneous object to estimate the vignetting function is trivial, since the brightness intensity curvature is directly proportional to this function.

The fundamental step of the proposed method is the dense background reconstruction achieved through a nonparametric approach. The images of the

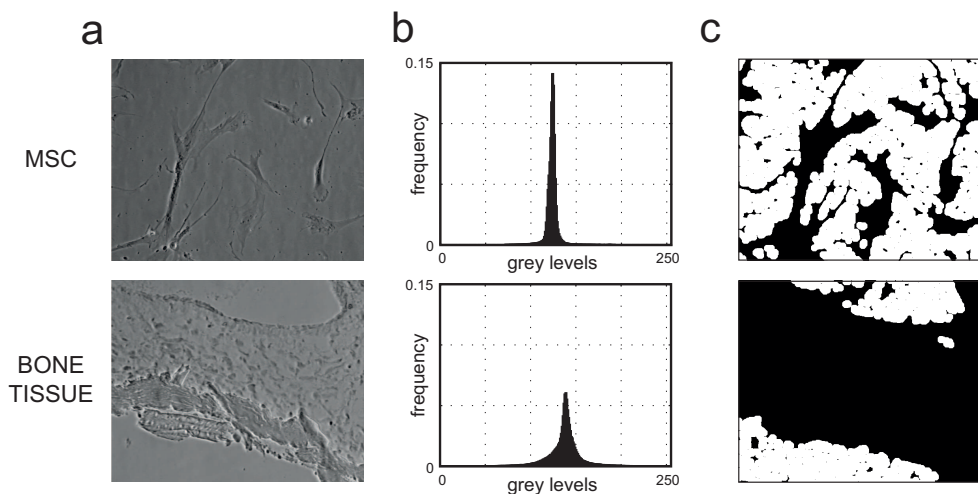


**Fig. 2.3:** Background segmentation. (a): two phase contrast widefield images: the first is related to a cell culture of mesenchymal stem cells (top), the second to a histological sample of a bone tissue (bottom). The contrast of the images has been stretched to improve visualization. (b): frequency of intensity levels of the images reported in Fig. 2.3a. In  $x$  the intensity values in grey levels. In  $y$ , the frequency values. In these types of images, the values of background and foreground lie in the same range. Thus, it is not possible to separate background from foreground using common approaches related to histogram analysis. (c): background image masks (in white) in Fig. 2.3a. These masks are obtained exploiting the proposed method to detect and segment the background values using a spatial approaches based on the first derivative.

sequence are first stored into a stack and the background is detected using a segmentation step based on the first derivative. Uncertain pixels, like those near the foreground regions, are discarded. A subsequent  $z$ -median filter is performed on the extracted regions and the obtained curve can be considered a good reconstruction of the background. Finally, in order to attenuate the noise typically present in the acquired images, a final spatial filtering is performed. The vignetting function is then estimated starting from the reconstructed background and subsequently normalized to the mean value of the obtained curve (see the algorithm pipeline highlighted in Fig. 2.4)).

In this approach, two particular stages must be analyzed in detail: the background segmentation, based on the first derivative of the single images, and the dense background reconstruction, necessary in case holes are present due to groups of  $(x,y)$  pixel position not having any correspondent background value.

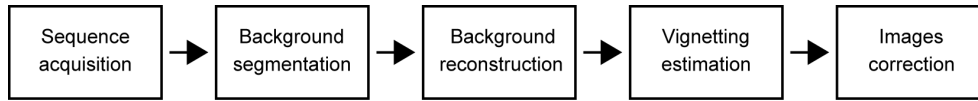


**Fig. 2.4:** Algorithm pipeline. Schematic flow chart of the proposed algorithms pipeline. Sequence acquisition: the method is multi-image based and exploits a sequence of images acquired under the same system set-up. Background segmentation: based on the first derivative mask. Background reconstruction: to obtain a dense surface through a  $z$ -median filtering and a low-order fitting. Vignetting estimation: to perform a spatial filtering of the dense background followed by a final normalization. Images correction: standard flat-field correction.

### 2.3.1 Background segmentation

Typically, to segment the background by excluding the foreground, the images histogram is analyzed to look for bimodalities and to see if two distributions exist that can be separated. In this case, several local [92, 93] or global [94] methods are used to define a suitable threshold value. Unfortunately, these approaches do not provide effective results if there is a large overlapping between the value distributions of background and foreground, which often happens in low contrast brightfield images (Fig. 2.3b).

To avoid these problems, in the proposed algorithm the histogram analysis of the original image is left out in favor of a spatial analysis: the assumption that in widefield microscopy the background is quite homogeneous yields the values of the first derivative in the background regions always lower than those in the foreground. Accordingly, the algorithm extracts the image background regions through analyzing the first derivative. Typically, not only the objects borders express a high first derivative, but also the objects internal structures can have values higher than the background. By processing the derivative masks through applying a global threshold, a subsequent strong morphological opening and a final removal of small size regions (area filtering), it is easy to obtain reliable masks where the presence of foreground and uncertain pixels is negligible (Fig. 2.3c). According to this approach, detecting all the background pixels is not crucial; what is fundamental is that all the pixels definitively detected, except a negligible number, belong to the background. However, at the same time we have to include enough background pixels so that the final reconstruction is dense.

Therefore, we have devised a strategy to achieve a suitable threshold value  $Th$  for derivative, that yields a good trade-off. To this purpose, we started by computing the mean value of the first derivative in a ROI manually selected from the image background. Subsequently, we chose for  $Th$  three times the value estimated that experimentally has been shown to be a suitable choice. Furthermore, it is worth remarking that this value is not too sensitive: using lower values (e.g., the double) could only yield slightly larger holes in the background masks.

### 2.3.2 Dense background reconstruction

One of the most important step of the proposed algorithm is the reconstruction of the dense 2D background surface. This stage is basically composed of three main operations:

- extraction of the background regions from all the single images of the sequence,
- calculation of the mean value for the  $(x,y)$  pixel positions using the pixel labeled as background only,
- closing any remaining holes due to lack of background in those  $(x,y)$  pixel positions.

In particular, the last step is required if some  $(x,y)$  pixel positions exist where no image contains background. In this case, the obtained curve would not be dense and would contain several holes. For instance, this happens when using images of a cell culture with 100% confluence (with the term confluence we mean the percentage of the area occupied by “objects”, i.e., not background. 100% confluence means completely full of cells).

To avoid this problem, the simplest solution is to ask the operator to acquire more images until each  $(x,y)$  pixel position of the entire area is covered with enough backgrounds contributions. When this is not possible, such as when the images are processed off-line, a fine choice is fitting the nondense 2D background surface with a low order polynomial and filling the holes with the estimated data without altering the values in the dense regions. Choosing a

low order polynomial is the best choice because the vignetting function typically assumes quite a regular trend: as a matter of fact, strong local changes can be attributed to lens impurities or dust. Nevertheless, to infer this missing information in correspondence of holes is almost always possible. That is, fitting gives good results only if holes are small and sparse. Otherwise, in case of too large holes, the lack of data would require parametric methods and our approach would lose its applicability.

## 2.4 Materials and tools

To test the method, 2 synthetic and 4 real-world image sets of different contents have been used. The synthetic images reproduce cell cultures at different confluences (60% and 80%). The real-world images regard living Mesenchymal Stem Cells (MSC), living Human Embryonic Kidney (HEK) cells and fixed histological specimens of bone and lung tissues. The cell cultures were contained in commercial plastic six-well plates and the histological tissues were placed on glass slides with mounting medium. The confluence of the MSC images used in the experiments was about 30%. All the images were acquired employing a diffused non automated widefield microscope, where the Köhler alignment is performed periodically. In particular, we used an inverted Nikon Eclipse TE2000-U endowed with a Nikon DXM1200 charge-coupled device (CCD) camera. The vision sensor is a 2/3" CCD, with approximately 1.3 Mpixels, square, with  $6.7\mu\text{m}$  side. The response function is almost linear, as it happens for most of the present industrial CCD cameras coupled with microscopes. The images were acquired either in phase contrast or brightfield. The objective used was always a Nikon Plan Fluor  $10\times/0.30$  Ph1 DLL  $\infty/0.17$ , a standard lens characterized by  $10\times$  magnification factor with a numerical aperture of 0.30 and the phase plate mounted in the lens focal plane. To acquire brightfield images no additional component was used, whereas the corrected condenser annulus diaphragm (Ph1) was aligned during the acquisition of phase contrast images. The final image size was fixed at  $512\times 640$  pixel resolution, and the images were saved as Bitmap (BMP format, RGB, 8-bit/channel). Each acquired image was then converted to grayscale using two open source image processing software widely cited in literature: ImageJ [95, 96] and GIMP (© The GIMP Team, [97]). The algorithm is written in MATLAB (© The MathWorks, Inc., Massachusetts, USA) and it is distributable upon request [11].

## 2.5 Experimental results

The experiments aim at assessing the improvements that the proposed method described above yields in terms of vignetting removal: the outcome is compared with those achieved by flat-field correcting the images using reference vignetting functions obtained from EF, culture medium free of cells and glass slide without any tissue.

Five different types of experiments were performed.

First, the method was assessed using different images, manually segmented by an expert operator, in order to get the backgrounds “ground truth”. The term “ground truth” is typically used in Pattern Recognition, mainly in supervised classification tasks, to define the pattern being considered as the true one. Hereafter, the definition is also extended to Image Processing mainly referring to the output of a manual segmentation task.

Second, the vignetting functions, estimated using stacks of synthetic images, and the ground truth ones, were statistically compared to evaluate how the confluence and the number of images could affect the reconstruction.

Third, the shapes of the vignetting functions, estimated using stacks of real world images, were compared with those of the reference vignetting functions.

Fourth, the flatness of the background of some representative images belonging to the real world sequences was evaluated before and after the flat-field correction, performed using the estimated and reference vignetting functions, according to the formula of Eq. 2.2.

Fifth, although the improvements in removing the vignetting effect yielded by our flat-field correction method can be perceived visually, they were even measured on both background and foreground, using sequences of overlapping images in mosaics.

### 2.5.1 Experiment 1: quality of the background segmentation

The goal of the proposed background segmentation is to detect the background while minimizing the false positive pixels. This means that discarding several background pixels is acceptable. The goal is that the pixels finally labelled as background ones are reliable, almost without any foreground pixels erroneously included in the segmented region. To prove the specificity of the background segmentation, the foreground ground truth of the representative images, related to different cell cultures and histological specimens, was obtained through a manual segmentation performed by an expert operator. It is worth noting that manual segmentation is a very time consuming task. For each image, the background automatically segmented with the proposed method and the foreground ground truth was compared. Of course, the best result is to obtain a background mask where no foreground pixels are included. In practice, this means that there should not be any overlapping region between the foreground mask manually segmented and the background mask obtained automatically.

To this purpose, the results regarding 4 different images, representative of those achievable with a widefield microscope in phase contrast or brightfield, are presented. In particular, these few images are really representative as the whole sets used because in cell culture images the main feature is represented by a very low contrast culture medium, while each histological sample shows the same texture in the whole specimen as far as the uniformity of background is concerned. The first image represents a culture of MSC (Fig. 2.3a top), the second regards fixed unstained bone tissue (Fig. 2.3a bottom), the third refers to HEK cells (Fig. 2.5a top) and the last regards lung tissue stained with Hematoxylin and Eosin (Fig. 2.5a bottom). In particular, the first two images are characterized by quite a general low contrast.

The first two columns of Tab. 2.1 report the threshold values of the first image derivative yielding 1% and 5% of foreground pixels erroneously detected as being background (false positives). Regarding the parameters of the proposed segmentation algorithm, in all the experiments we used a disk-shape kernel (morphological structuring element) with 9 pixels radius for morphological opening and then removed the regions smaller than  $15 \times 15$  pixels. In particular, the MSC images are typically characterized by a very low contrast,

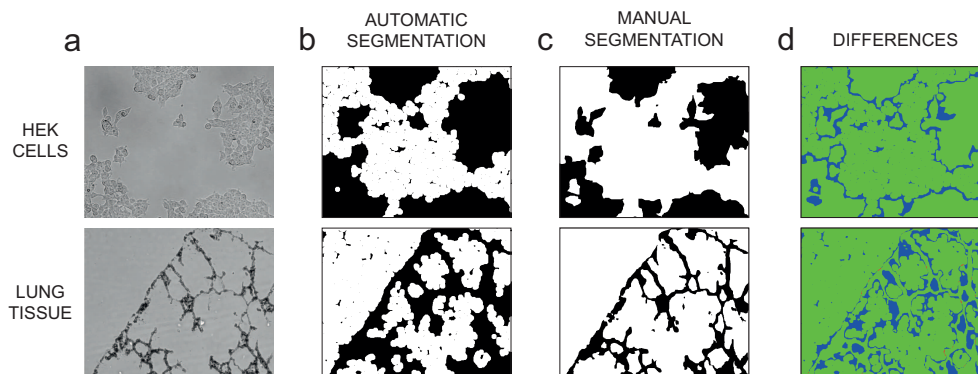


**Fig. 2.5:** Comparison between automatic and manual background segmentation. (a): images of HEK cells (top) and a lung tissue histology (bottom). The contrast of the images has been stretched to improve visualization. (b): background masks (in white), obtained using the proposed automatic background segmentation algorithm: the percentage of false positive is below 5%. (c): reference masks of background manually segmented by an expert microscopist. (d): images representing in different colours the differences between the masks obtained manually and automatically. In green the pixels where the masks present both background or both foreground values. In blue the pixels where the mask automatically obtained presents foreground and the mask manually obtained presents background values. In red the false positive pixels where the mask automatically obtained presents background and the mask manually obtained presents foreground values. Only few pixels for each figure result red.

set	threshold value [gray levels]		mean of the first derivative		
	limit false positive < 1%	limit false positive < 5%	area 1	area 2	area 3
MSC	5.5	7.5	2.2	2.1	2.1
HEK	22.5	37.5	2.4	2.2	2.3
BONE	8.5	11.5	2.3	2.2	2.3
LUNG	8.5	27.5	2.1	2.2	2.2

**Tab. 2.1:** Threshold values for the background segmentation. The foreground pixels erroneously included in the background masks (false positive) were counted using four different types of images depicting: MSC, HEK cells, bone tissue, and lung tissue. To this purpose, the masks obtained using the proposed algorithm to automatically detect and segment the background were compared with the ground truth. The first two columns report the first derivatives threshold value yielding a false positive rate of 1% and 5%. The last three columns report the mean values of the first derivative, calculated in three background ROIs manually selected.

even when acquired in phase contrast, mainly due to their nature of being flat adherent cells, therefore tending to settle in a very thin layer. For compar-

ison purposes, we acquired two images of nuclei and actina filaments, both referring to adherent cells, that is MSC and osteosarcoma bone cells (Saos-2 by ATCC, coming from standard commercial line, catalog no. HTB-85) using Nikon Eclipse Ti confocal microscope equipped with a digital CCD DS-QiMC camera and a Plan Apo VC 60 $\times$  Oil DIC N2 lens (Fig. 2.6). In these types

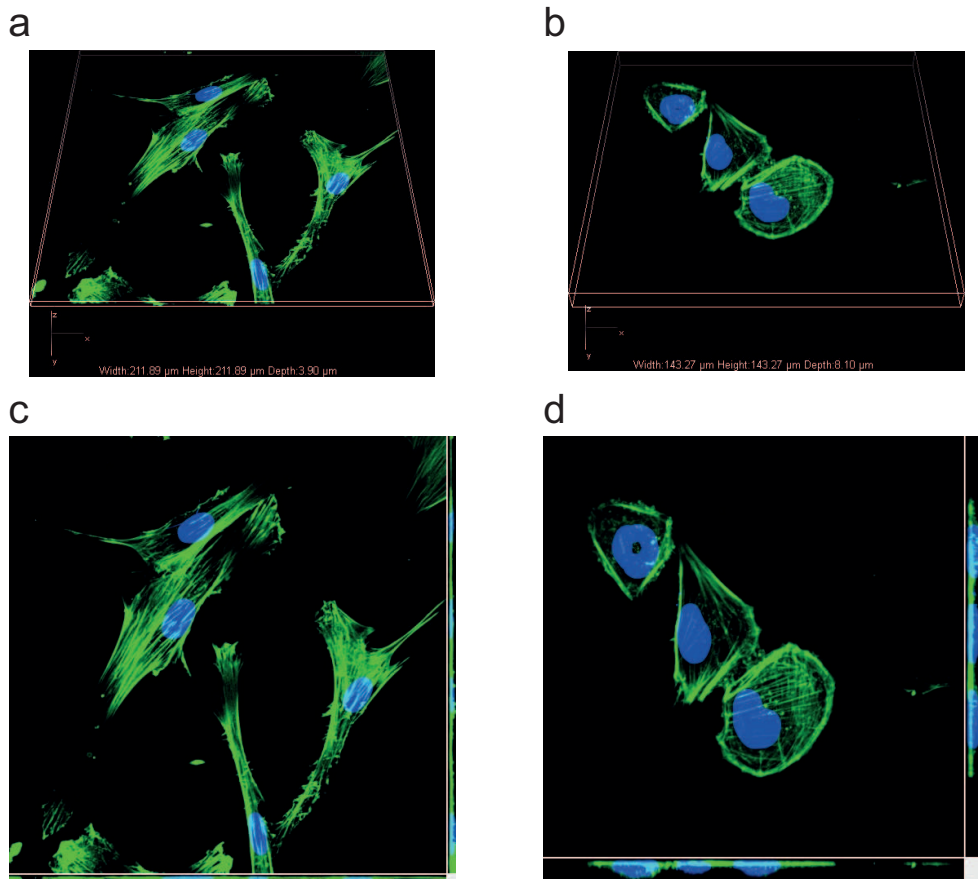


**Fig. 2.6:** Depth dimension of Mesenchymal Stem Cell. Comparison between fluorescence images regarding Mesenchymal Stem Cells (MSC) (**a**, **c**) and osteosarcoma bone cells (Saos-2) (**b**, **d**), acquired at 60 $\times$  using a confocal microscope. The cells nuclei are highlighted in blue, using DAPI, while in green the Actina filaments using FITC. (**a**) and (**b**) are 3D plots of the acquired stacks of slices. Images (**c**) and (**d**) report the top view and the  $(x,y)$  depth projections of the volume maximum intensities. The depth dimension of the MSC is about half of the Saos-2: 3.9 $\mu\text{m}$  and 8.1 $\mu\text{m}$  respectively.

of images, it is quite difficult even for an expert biologist to manually segment the foreground. This is the reason why the lowest values, reported in the first two columns of Tab. 2.1, are related to the MSC images. A derivative thresh-

old value  $Th = 7.5$  (expressed in gray levels) was experimentally proved as being the minimum value to obtain in each image a maximum false positive rate of 5%, which could be more than an acceptable value. Furthermore, it is worth noticing that for all the images used in the test, except for the MSC images, the false positives related to this threshold value are lower than 1%. As mentioned before, to define a fair threshold value for the first derivative, a correct strategy could be to manually segment some background ROIs in the image and to compute the mean of their first derivative. This value, multiplied by a positive correction factor, could be considered a good threshold. The last three columns of Tab. 2.1 report the mean values of the first derivative of three background regions, manually selected for each image. All the values are at least three times lower than  $Th = 7.5$  (i.e.,  $\leq 7.5/3$ ), hereafter chosen as the first derivative threshold for each image. Figs. 2.3c and 2.5b report the background masks determined using our algorithm and related to the four tested images.

## 2.5.2 Experiment 2: vignetting estimation in function of number of images and cell confluence

As already stated in Sect. 2.3, the confluence of images affects the reconstruction of the vignetting function. For instance, the proposed method fails in case of images of cell cultures with 100% confluence, where no background region is present. To analyze how confluence and number of images of the processed stack affect the reconstruction, we employed some stacks of synthetic images where cell cultures are artificially simulated. The images were built using an image generator implemented in MATLAB. Cells and debris are simulated, over a flat background, by randomly displacing in the field of view two different types of chessboard. The number of cells and debris depends on the required confluence. The vignetting function we built artificially, with the purpose of setting up a ground truth in the subsequent simulations, is then applied by multiplication to the synthetic images obtained, followed by the application of Added White Gaussian Noise (AWGN) with mean 0 and standard deviation (std) 4. We used the grey levels image generator to obtain stacks of images with  $512 \times 640$  pixel size at 60% and 80% cell confluences (Fig. 2.7a). In particular, the higher confluence value was selected as an upper bound, because in real world cases obtaining good results using a stack of images with higher

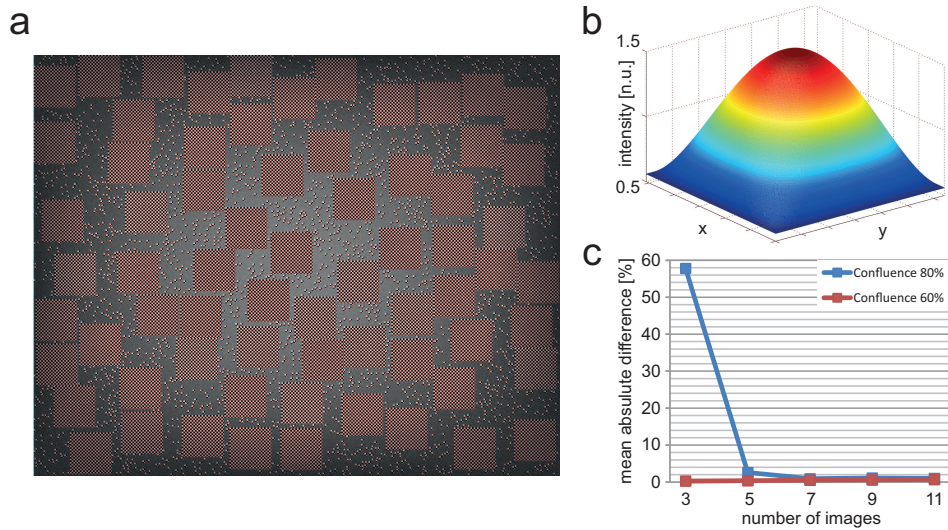


**Fig. 2.7:** Relation between vignetting, confluence and number of images. (a): a generated synthetic image characterized by a confluence value of 60%. (b): 3D plot of the biquadrate function used to simulate the vignetting in the synthetic images. (c): trends of the mean absolute difference between the vignetting functions estimated with the proposed method and the ground truth, related to the confluence and the number of images of the stack processed.

confluences is very challenging, due to the small percentage of background available. To build the images we used a perfectly flat background (gray value set at 85), while for cells and debris we used two different square-shape black and white chessboards (each black or white square of  $2 \times 2$  pixels), with external chessboards's side of 51 and 3 pixels, respectively. The values could be considered representative for MSC and debris visualized using  $10 \times$  microscope lens. The vignetting function was obtained using a 2D biquadric distribution (Fig. 2.7b) with normalized values ranging between about 0.5 and 1.5 and the maximum value in the center of the field of view. Finally, the vignetting functions, reconstructed using the proposed method and stacks of different number of images, were statistically compared with the vignetting function of ground truth by computing the pixel-wise mean absolute difference (the sign differences would compensate with each other giving a mean values near to zero). For each confluence (60% and 80%) and number of images (we choose sets of 3, 5, 7, 9, and 11 images) we built five different stacks.

The graph of Fig. 2.7c collects the worst achieved results among the five stacks

analyzed for each fixed number of images. Using lower confluence value (60%) the vignetting function estimated is very similar to the ground truth just using stacks of three images only. Using 80% confluence the results are expectedly worse, but with a stack of 7 images only the mean absolute difference with the ground truth is as low as 2%. These results prove that also when using high confluence images the proposed method is capable to excellently reconstruct the vignetting function, by always exploiting a very small number of images. The synthetic image stacks free of vignetting and noise are distributable upon request [11].

### 2.5.3 Experiment 3: comparison of shapes of different vignetting functions

The goal of this experiment is to estimate how much the vignetting functions estimated from the images themselves resemble the reference ones. To this purpose, we used several sequences of images acquired in the same day, by using the same equipment set-up, including lamp voltage and exposure time. In particular, we propose the results obtained using two sequences of images: the first one is made of 13 images of a MSC culture, while the second one is of about 15 images of a histological sample of bone tissue. For each sequence, the percentage of  $(x,y)$  pixel positions is less than 2% where at least three images gave a background contribution. The vignetting functions estimated with the proposed method were compared with the reference ones estimated from EF, culture medium only and a part of a glass slide where no tissues are present. To obtain the reference vignetting functions, dozens of images were acquired for each of them and a simple  $z$ -median filtering was performed for each  $(x,y)$  pixel position. It is worth noticing that the sequence of 13 MSC images and the images referring to the culture medium only came from two different wells of the same commercial plastic six-well plate and the images related to the glass slide came from the same specimen slide of bone tissue cited above, but from regions free of tissue. To be able to compare the different functions, each of them is first normalized by its mean value ( $Vi_N$ ). The Absolute Difference Normalized Metric (ADNM), an absolute pixel wise subtraction between two different surfaces, normalized by the range interval of the first one (according to Eq. 2.3), has been computed between each normalized vignetting function

and the one estimated from the EF, normalized by its mean value ( $EF_N$ ).

$$ADNM(x, y) = \frac{\|EF_N(x, y) - Vi_N(x, y)\|}{\max(EF_N) - \min(EF_N)} \quad (2.3)$$

The mean value and the std of the ADNMs give us information about the relative discrepancy [98] of the different functions.

Fig. 2.8 shows the different vignetting functions used for comparison. The

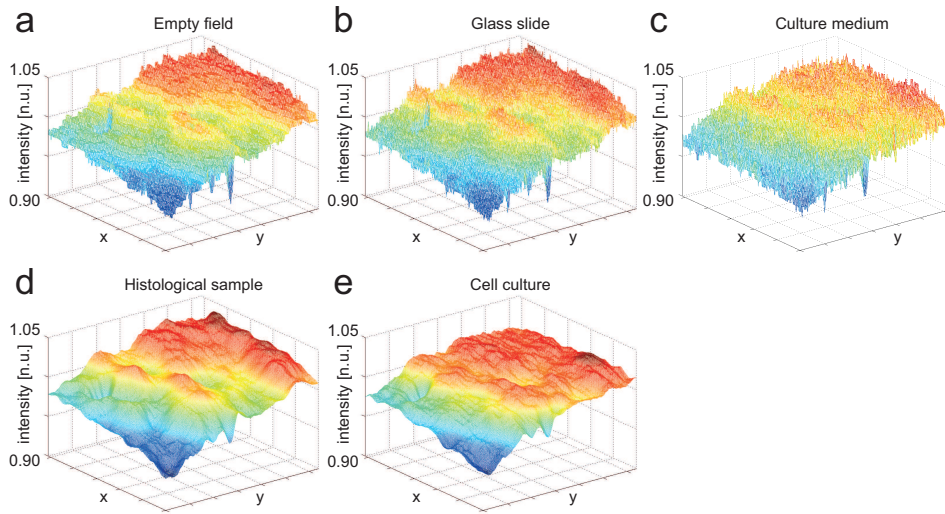


**Fig. 2.8:** Vignetting functions shapes. The first row reports the 3D plots of the surfaces of the vignetting functions estimated from: (a) EF, (b) glass slide free of tissue, (c) culture medium only. All these functions are obtained by performing a simple  $z$ -median filtering on a stack of acquired images. The second row reports the vignetting functions estimated from: (d) a histological sample of bone tissues, (e) a culture of MSC. The last two estimations were obtained using the proposed algorithm. All the functions were normalized to their specific mean value, so the  $z$ -axis of the 3D plots is relative to the normalized unit (n.u.) of the intensity values.

asymmetry is mainly due to the loss of the Köhler alignment. It is evident that the three reference vignetting functions (Figs. 2.8a and 2.8c) obtained using a simple  $z$ -median filtering are noisier than the two obtained using the proposed method (Fig. 2.8d and 2.8e). This is due to the fact that no spatial filtering was performed in the former functions. As a matter of fact, the following ranking based on the ADNMs evaluation was expected. From best (smallest mean and std values) to worst results: vignetting function estimated from a glass slide

free of tissue, the histological sample with bone tissue, the cell culture, the culture medium without any cell inside. The reason why the best result was achieved with the glass slide is obvious: a glass slide and an EF behave almost in the same way as far as the transit of the light is concerned. For the same reason, one could expect the second best results for the histological sample: the proposed algorithm reconstructs the function starting from the background region and in a histological sample the background regions are glass regions free of tissue. The culture medium present in both cell culture and culture medium is a very different substrate from an EF: in this case, the light must cross a significant volume of medium and the lower plastic support of the wells plate. The worst result is the one obtained using the culture medium only, without cells inside, because the vignetting function estimated from it was obtained with a simple median  $z$ -filter, without any segmentation step that removes the debris present in the medium. Instead, the algorithm performed in the second sequence, the one referring to the cell culture, contains a segmentation step where both cells and debris are removed: in this case the vignetting function is estimated from a less noisy subset of pixels. Tab. 2.2 reports the mean value and the std of the ADNMs computed for each  $Vi_N$  obtained.

ADNM		
set	mean [%]	std [%]
GLASS SLIDE	3.20	2.18
BONE TISSUE	3.35	2.67
MSC CULTURE	5.45	4.17
CULTURE MEDIUM	6.30	4.60

**Tab. 2.2:** The Absolute Differences Normalized Metric (ADNM, Eq. 2.3) was performed using the reference vignetting functions, estimated from EF images, and those estimated from: a glass slide without any tissue, a histological sample of a bone tissue, a culture of MSC, a culture medium without any cell inside. Columns report the percentage values of mean and std of the obtained ADNMs.

#### 2.5.4 Experiment 4: effectiveness of image correction using different vignetting functions

The flat-field correction, performed using the vignetting function, aims to compensate the fall-off of the images brightness. Theoretically, if the true function

is known, the correction would lead to obtain vignetting free images, with vignetting curve being perfectly flat. Therefore, to determine which functions lead to obtain the best result, the flatness of several images was evaluated using, in the flat-field correction, all the different five estimated vignetting functions, including the three of reference and the two estimated with our algorithm (that had already been compared in the experiment discussed in Sect. 2.5.3). An image of a perfectly homogeneous object, undergoing low vignetting effects, is characterized by a very narrow distribution of intensity values with a small std (due to the camera noise only). In widefield microscopy, the background in images regarding cell cultures and histological specimens can be considered a pretty homogeneous object. To assess which vignetting function leads to the best *flatness* (lowest value), the std of the distribution of the local mean values, computed on a square moving window, has being considered. As the side of the window we chose 10% of the largest side of the original images, this being compatible with the size of a cell visualized at a magnification factor  $10\times$ . To this purpose, 7 images of a MSC culture and 7 of a histological specimen with bone tissue were selected. These images were acquired by exploiting the same culture and specimen analyzed in Sect. 2.5.3, but they are not included in the sequence used to estimate the vignetting functions. Each image was manually segmented to extract some background regions that were then used to evaluate the *flatness*, before and after the different flat-field corrections. Actually, the size is the same for all the images and the *flatness* is always computed locally using a patch of the same size. This yields comparable results.

Fig. 2.9 presents the 3D visualizations of the local mean values of the background region manually segmented from one out of the fourteen images (Fig. 2.9a), selected as the representative. The vignetting effect is manifestly appraisable (Fig. 2.9b). After the flat-field corrections, it becomes particularly flat (Fig. 2.9c). No visual difference is visible between the 3D visualizations of the background after the different flat-field corrections.

Tab. 2.3 reports the *flatness* values of the background of all fourteen selected images, evaluated before and after the flat-field correction performed with the different vignetting functions. Of course, all the correction methods yield an improvement with respect to the values related to the original distributions where no correction was performed. Due to the small difference between some values for both types of images, dividing the tested vignetting functions into two groups for each type of images is fairer than decreeing a single winner.

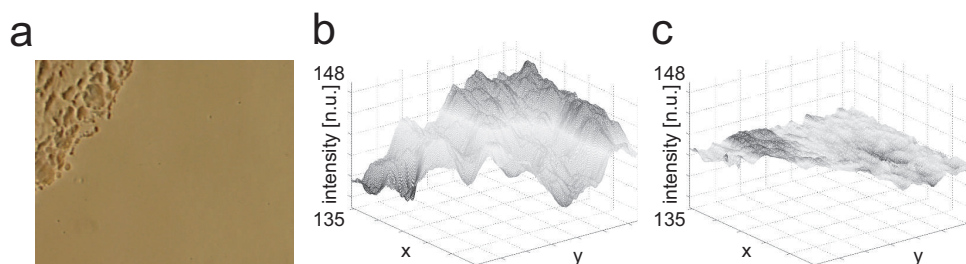


**Fig. 2.9:** Flat-field correction on single images. (a): an image of a histological specimen of a bone tissue (in the upper left corner). The background covers about 75% of the image. (b): 3D plot of the distribution of the local mean values of the background, calculated on moving square ROIs with size set at 5% of the maximum dimension of the original image. (c): the same 3D plot of the distribution of the local mean values, calculated using the image flat-field corrected with the vignetting function estimated from EF (Fig. 2.8a). The vignetting effects are strongly attenuated, yielding a pretty flatter means distribution.

		<i>flatness</i>						
set	vignetting function	image 1	image 2	image 3	image 4	image 5	image 6	image 7
MSC	no correction	2,03	2,10	1,49	1,88	1,84	1,65	1,93
	empty field	1,19	0,94	1,02	0,82	0,89	0,86	0,89
	glass slide	1,17	0,88	0,96	0,76	0,85	0,74	0,85
	culture medium	0,63	0,69	<b>0,71</b>	<b>0,45</b>	0,58	<b>0,65</b>	0,58
	bone tissue	1,24	0,99	1,15	0,85	0,96	0,83	0,97
	MSC culture	<b>0,54</b>	<b>0,49</b>	0,83	0,51	<b>0,48</b>	0,69	<b>0,47</b>
BONE	no correction	2,40	2,20	1,62	2,10	1,87	2,44	2,38
	empty field	0,26	0,29	0,63	0,57	0,29	0,24	0,24
	glass slide	<b>0,18</b>	<b>0,23</b>	<b>0,61</b>	<b>0,51</b>	<b>0,10</b>	<b>0,10</b>	<b>0,15</b>
	culture medium	0,78	0,72	1,12	1,08	0,94	0,75	0,64
	bone tissue	0,34	0,33	0,64	0,59	0,16	0,29	0,39
	MSC culture	0,76	0,86	1,13	1,12	0,97	0,71	0,63

**Tab. 2.3:** Image flatness using different vignetting functions. To evaluate which vignetting function yields the best results in terms of vignetting correction, the background region of 7 images of a culture of MSC and 7 images of a histological sample of bone tissue were analyzed. *Toflatness* of each image was evaluated before and after the flat-field correction performed using all the five different vignetting functions reported in Fig. 2.8. For each image, the best value obtained (i.e., the lowest one) is reported in bold. For each type of images, the values of the group achieving the better results are reported in green.

Therefore, the first group is composed of the vignetting functions that yield the best results (in Tab. 2.3 the values of the first group are reported in green), while the second group contains functions yielding the worst ones. As regards the 7 images of the MSC culture, the best values are achieved by the vignetting

functions estimated from the culture medium and from the images themselves. As regards the bone tissue, the best value is always achieved by the vignetting function estimated from the glass slide. Nevertheless, also those estimated from EF and the sequence itself lead to far better results than those estimated with the other two vignetting functions. In practice, the vignetting function estimated from the culture medium only and the vignetting function estimated from the background of the MSC images are estimated using always the same “object”, the culture medium. Accordingly, obtaining similar result using the two vignetting functions was expected. The same discussion is valid also for the three vignetting functions estimated using empty field, glass slide and background of the bone tissue images. In these cases, the vignetting function is estimated always from regions without anything in the light path, or at maximum a thin slice of glass. In particular, for both types of images, the vignetting functions estimated from the whole sequences (the testing images excluded) using our method fall into the group yielding the best results. From a general point of view, this produces a remarkable outcome: estimating the vignetting function from the images themselves always yields a good vignetting correction. Comparing the values of the two type of images reported in Tab. 2.3, it is worth noticing that after the flat-field correction the background of the MSC images are characterized by generally worse flatness values than the bone tissue images. The main cause is due to the background of the MSC images including “noise” (thick plastic plate and volume of culture medium with debris), while the background of the bone tissue consists of thin coverslip and glass slice only. Consequently, a more homogeneous background lowered *flatness*. In general, assuming a main linear behaviour of the vignetting function, a higher image mean value yields a more emphasized vignetting curvature. Also, when no correction is performed, the overall curvature of the vignetting gives the main contribution to the lack of *flatness*, accordingly. This is confirmed by comparing the values before correction in the “no correction” rows of Tab. 2.3) of MSC and bone tissue images, where the latter are always higher.

### 2.5.5 Experiment 5: numerical analysis of flat-field correction using mosaics

Besides studying and measuring the effects of vignetting correction in terms of global flatness, we focus our attention on the effect on a typical application

that emphasizes the effect of vignetting, that is mosaicing of images. In fact, when two or more images are stitched to create a mosaic, the seams in the stitching zones become particularly evident if the vignetting effects are not compensated. To build a mosaic using a manual stage, the single images to be stitched have to overlap and the overlapping regions represent a meaningful test-bed to assess the effectiveness of the vignetting correction. Theoretically, if the stitched images are previously perfectly flat-field corrected, no photometric misalignments should be visible. In this experiment, we compared mosaics of the same set of images, before and after being corrected using the five vignetting functions already used in the previous experiments. Several images, taken from the MSC culture and the bone tissue sample already used in the experiments dealt in Sect. 2.5.3 and Sect. 2.5.4, were aligned and analyzed both visually and numerically. The first group of mosaics created is composed of 7 MSC images while the second group is made of mosaics of 6 bone tissue images. The percentage of overlapped area in each couple of sequent frames is between 15% and 75%. The images used in the two groups of mosaics were acquired under the same setup conditions as the ones used to estimate the vignetting functions, but they are not included in the sets used before.

While Chap. 4 describes the whole mosaicing approach we conceived and implemented, in this section we provide just a summary of the main characteristics. The mosaics of images are built incrementally, finding out the transformation matrices that link couples of subsequent images (according to the Frame-to-Frame approach [99]). In particular, we used translative matrices and to find out the  $x$ - $y$  shift we found matches between significant features of the images (we used the Shi-Tomasi corner points [100] and the Lucas-Kanade tracker [101]). All the images are aligned in the domain of the reference frame (in our case, the first image acquired) and each new input image overwrites the mosaic being built. The transformation matrices have been estimated using the original uncorrected images, but they have been used to built all the mosaics, also those referring to corrected images, so to have the same probable geometrical misalignments. In this way, it is possible to separate photometric and geometric effects and to determine which mosaic yields the best tonal alignment.

In particular, we considered the Back Projection ( $BP$ ) of each original image ( $I$ ) aligned into the mosaic, and its part overlapped by the mosaic (Overlapped Part -  $OP$ ). Fig. 2.10 provides a visual schematic representation to understand

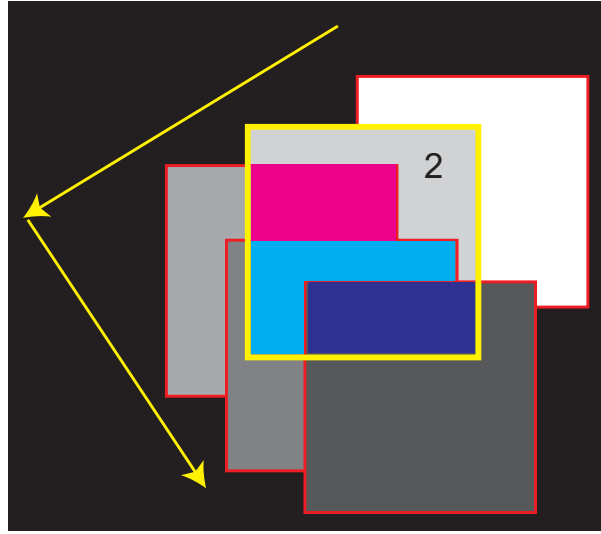


**Fig. 2.10:** Component images and overlapped parts of the mosaic. Here it is provided a visual schematic representation to understand better how  $OP_n$  is defined for each image  $I_n$  back-projected into the mosaic. In this example, the position of each image is coloured using different grey intensities and the borders are reported in red. The border of the image  $I_2$ , back-projected into the mosaic ( $BP_2$ ), is highlighted in yellow. The contained regions coloured in magenta, cyan and blue constitute  $OP_2$  and they represent the contained mosaic's regions overwritten by images  $I_i$ ,  $i > 2$ .

better how  $OP_n$  is defined for each image  $I_n$  back-projected into the mosaic. Practically speaking, every time a image  $I_n$  is back-projected (in Fig. 2.10  $BP_2$  is defined by the yellow border), we considered only the pixels of the mosaic in  $OP_n$  that are overwritten by subsequent images  $I_i$  with  $i > n$  ( $OP_2$  are the coloured regions in Fig. 2.10), since the difference between  $BP_n$  and  $OP_n$  where  $I_n$  contributes is always 0. Accordingly, using the warping matrices previously estimated, we back-projected on the mosaics all the stitched images, but the last one (no image overwrites the mosaic after the last is stitched).

To provide a numerical assessment of the effect of the different vignetting correction, three widely diffused metric indexes were used [102]. The first one is the Mean Squared Error ( $MSE$ ) [103], defined according to Eq. 2.4:

$$MSE_{(OP,BP)} = \frac{\sum_x \sum_y [OP(x,y) - BP(x,y)]^2}{P} \quad (2.4)$$

$P$  is the number of pixels of  $OP$  (and  $BP$ ). In particular, we define  $MSE_{(OP,BP)}$

as the  $MSE$  computed using  $OP(x,y)$  and  $BP(x,y)$ . The second index is the Signal to Noise Ratio ( $SNR$ ) [104] defined in Eq. 2.5:

$$SNR_{(OP,BP)} = 10 \log_{10} \frac{\sum_x \sum_y OP(x,y)^2}{P \cdot MSE_{(OP,BP)}} \quad (2.5)$$

The last index considered is the Universal Quality Index ( $UQI$ ), a quality index [105] which is designed by modeling any image distortion as a combination of three factors: loss of correlation, luminance distortion and contrast distortion (Eq. 2.6).

$$UQI_{(OP,BP)} = \left( \frac{v_{(OP,BP)}}{\sigma_{OP} \cdot \sigma_{BP}} \right) \cdot \left( \frac{2 \cdot \mu_{OP} \cdot \mu_{BP}}{\mu_{OP}^2 + \mu_{BP}^2} \right) \cdot \left( \frac{2 \cdot \sigma_{OP} \cdot \sigma_{BP}}{\sigma_{OP}^2 + \sigma_{BP}^2} \right) \quad (2.6)$$

$\mu_{OP}$ ,  $\mu_{BP}$ ,  $\sigma_{OP}$ ,  $\sigma_{BP}$  and  $v_{(OP,BP)}$  are mean, std and covariance, respectively, of  $OP(x,y)$  and  $BP(x,y)$ . Although the  $UQI$  is defined mathematically and no human visual system model is explicitly employed, the authors proved that it could evaluate the quality of images similarly to what the human visual perception does [106].

Fig. 2.11 shows the two mosaics created by registering the original, not corrected, images (Fig. 2.11a, Fig. 2.11c) and the ones flat-field corrected using the vignetting function estimated from EF (Fig. 2.11b, Fig. 2.11d). No difference is visible to the naked eyes between the mosaics created using the different tested vignetting functions (accordingly not shown). Nevertheless, the benefits introduced by the flat-field corrections are evident just at first sight: the seams are widely attenuated and the stitching zones can be hardly detected. Tab. 2.4 reports the values referring to the metric indexes calculated considering in the same time all the pixels of the back-projected and the overlapped parts of the built mosaics. In particular, only for this experiment we compared at the same time all the pixels of the back-projected and the overlapped parts of the mosaics, estimating for each index a single value only. These data are used to numerically evaluate which vignetting function yields the best results (lowest  $MSE$  and highest  $SNR$  and  $UQI$ ). As expected, the data show that all the corrections improve the mosaics created using the original images. First,  $MSE$  and  $UQI$  for the mosaics of the bone tissue are always higher because the dynamic range of the MSC images is limited as against the other images. In fact, under the same misalignment conditions, a wide dynamic range of the images causes higher local differences than a narrow range and the human visual

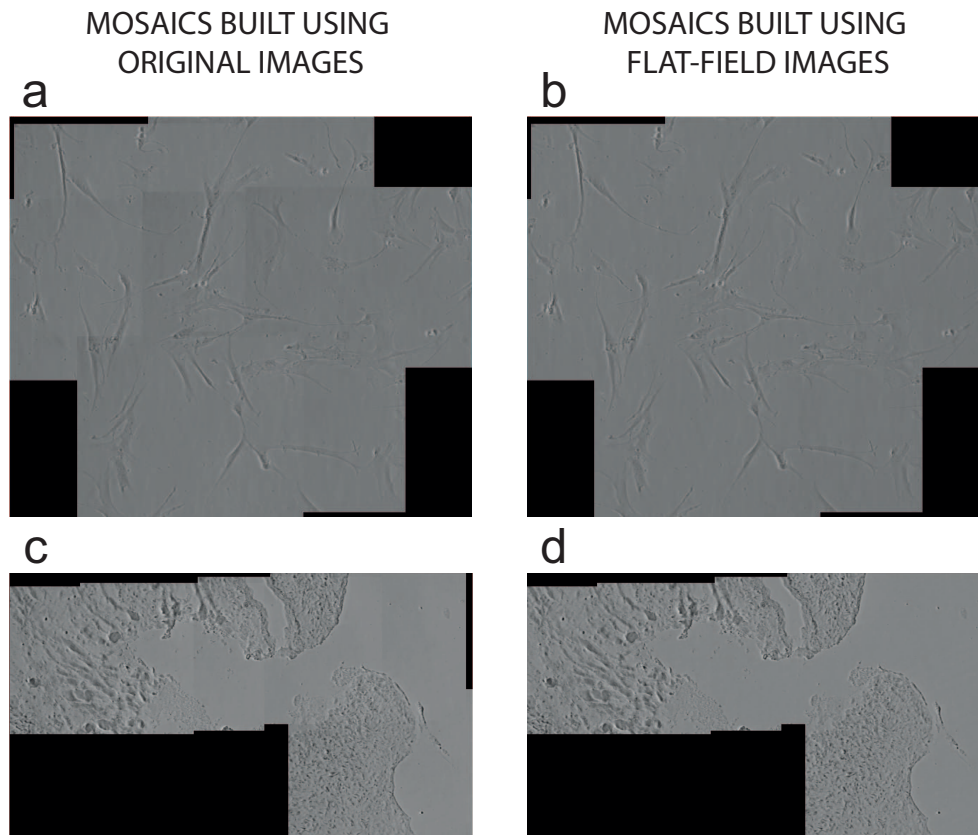


**Fig. 2.11:** Flat-field correction on mosaics. Mosaics created using two different sets of images: the first is made of 7 images of MSC, the second of 6 images of a bone tissue. The percentage of overlapped regions in couples of subsequent frames ranges from 15% and 75%. In (a) and (c) two mosaics built using original images are reported. In (b) and (d), the same mosaics built using the same set of images previously flat-field corrected using the vignetting function estimated from EF (Fig. 2.8a). No difference in visual quality is detectable at sight between the mosaics created using the different vignetting functions (shown in Fig. 2.8). The contrast of the images has been stretched (using the same Look-Up-Table for (a) and (b) and for (c) and (d)) to improve visualization.

perception is better for well contrasted images. Furthermore, according to the Eq. 2.4, images with a high  $MSE$  are characterized by a low SNR. Regarding MSC mosaic, there are no relevant differences between the results obtained with the different vignetting functions, but it is worth noticing that the best results are those related to the vignetting function estimated stemming from the images themselves. On the other side, it was quite unexpected to find out that the worst result is related to the vignetting function estimated from the culture medium. However, this could be due to the vignetting function

metrics				
set	vignetting function	$MSE$	$SNR$	$UQI$
MOSAICS MSC	no correction	18.15	29.31	0.7469
	empty field	8.30	32.78	0.8606
	glass slide	8.44	32.70	0.8587
	culture medium	8.78	32.50	0.8544
	bone tissue	8.21	32.83	0.8644
	MSC culture	<b>7.69</b>	<b>33.09</b>	<b>0.8691</b>
MOSAICS BONE	no correction	25.05	28.92	0.9490
	empty field	<b>12.06</b>	<b>31.97</b>	<b>0.9606</b>
	glass slide	12.22	31.92	0.9602
	culture medium	14.44	31.22	0.9549
	bone tissue	12.31	31.88	0.9598
	MSC culture	14.02	31.34	0.9558

**Tab. 2.4:** Quality of mosaics. Three different quality metric indexes,  $MSE$ ,  $SNR$  and  $UQI$  were evaluated on several mosaics created using two different sets of images: the first referring to MSC, the second to bone tissue. In order to determine which vignetting function leads to the best mosaic only in terms of tonal correction, they were built by keeping the registration matrices fixed for all of them. The data related to the not corrected images and to those flat-field corrected using five different vignetting functions (Fig. 2.8) are reported for both subsets of images. The best results (lower  $MSE$ , higher  $SNR$  and  $UQI$ ) are shown in bold.

being the one estimated from the noisiest images: for the culture medium a simple  $z$ -median filter was performed without any spatial filtering or outlier removal step and the images of culture medium are full of corpuscles and debris which were taken into account in the vignetting function estimation. This is also the most probable reason why this vignetting function yields the worst results even with the mosaic of the bone tissue. In fact, in this second mosaic the results obtained with the different vignetting functions are spread over a wider interval. As done for the experiment of Sect. 2.5.4, it is possible to split the results related to the different vignetting functions into two groups here too and, again, the best results are achieved by the vignetting functions estimated from EF, glass slide and images themselves. As a final remark, it is worth noticing how estimating the vignetting function with the proposed method starting from the images themselves almost always yields the best vignetting correction and, when not, it is comparable with that achieved with the reference functions.

## 2.6 Conclusion and future work

### 2.6.1 Conclusion

The main goal of this study is to make the users of light microscopes aware of a common problem typically neglected that affects all the acquired images: the uneven fall-off of the brightness intensity, namely vignetting. The effect of vignetting could be particularly problematic for quantitative image analyses and also several image processing steps like segmentation or object tracking can severely undergo this effect. The mathematical formulation of the vignetting problem, intrinsic to the image acquisition system, was explained before introducing the flat-field correction formula widely used in literature to correct for this unwelcome effect. The previous work was extensively analyzed, showing strengths and weaknesses of each class of methods. Usually, the approach widely used in literature and in the common practice in order to obtain the vignetting function is to acquire in advance an image of a homogeneous reference object. Despite the simplicity of this solution, the reference object is not always at one's disposal, besides requiring the microscope's user to perform one additional operation before each acquisition session. Furthermore, the estimated vignetting function could not be the best to correct images of cell cultures and histological samples, that represent the most used samples in the biological routine examinations.

Arising from these considerations, we focused our study on developing and assessing a novel method, also suitable for real-time applications, to estimate the vignetting function directly from the sequence of the images to be corrected. The fundamental task consists on an accurate yet simple background segmentation step based on the first derivative masks of the images of the sequence. The vignetting function is then estimated through a median filtering performed on the background regions extracted from the stack. Finally, the flat-field correction is accomplished normalizing each image by the vignetting function, according to the standard correction formula.

To prove the effectiveness of the proposed method, different types of experiments were performed.

The accuracy of our background segmentation algorithm was tested in the

first experiment, using representative microscopic images. The percentage of false positive pixels (i.e., pixels belonging to foreground) remained lower than 5% even for images with very a low contrast. This proves that the proposed segmentation algorithm can be used to detect reliable background pixels.

To evaluate how the image confluence and the number of images in the processed stacks affect the reconstruction result, several synthetic stacks were generated and analyzed. Just using stacks with 7 high confluence images only, the mean absolute difference between the estimated vignetting function and the ground truth stays below 2%. In practice, this means that the method can use even a very small set of images to estimate the vignetting function.

The performances of the flat-field correction was assessed using single representative microscopic images, where the background was manually segmented. The “flatness” of the background regions was computed before and after the different corrections. Our method almost always achieved the best result (or, at least comparable), this proving the effectiveness of our method to flat-field correct the background of images representative of a wide class of biological samples.

In the last experiment, we considered the mosaicing application as a useful benchmark to study the effects of vignetting on whole images. In particular, two mosaics were built with and without vignetting correction in order to measure the improvement of the different methods in the flat-field correction of the whole images. Different metric indexes were calculated in overlapping regions of mosaics, displaced in different parts of the field of view. Again, the best performances were obtained using our vignetting function estimation and, in a limited number of cases, they were comparable with those achieved with gold-standard functions.

On the whole, the experiments demonstrate that, for cell cultures, using the vignetting function built on a given sequence of images to correct the images themselves constitutes always the best solution, although it could not yield the flattest background. As far as the histological samples are concerned, the best corrections are obtained using reference objects, although the outcomes of our method are comparable.

The content of this chapter was partly published in [107, 108, 109, 110].

## 2.6.2 Future work

Several steps should be deepened to improve the overall performance of the proposed algorithm.

To increase the number of the background contribution for each  $(x,y)$  pixel position, an assisted approach could rely on the microscope user. For instance, the operator could be asked to move towards regions containing more background and then continue acquiring more images until a prefixed amount of contributions is achieved for each  $(x,y)$  pixel position. In order to achieve a completely automated solution to build the background, it is important to better analyze how much information is needed to obtain good statistics in order to reconstruct a more accurate background. This topic is strictly related to camera and system noise as well as to the nature of the background itself. In particular, the camera and system noise could be better simulated in the synthetic images used to analyze how confluence and number of images affect the vignetting estimation. Furthermore, a different approach, better than using a polynomial fitting to cope with probable holes in order to obtain a dense background, could be devised, this playing an important role on the estimation of the final vignetting function.

For a more detailed analysis of the quality of the obtained results, in terms of image correction achieved by different vignetting functions, a more specific quantitative index could be conceived to better represent the image flatness. The standard deviation of the distribution of the local mean values we proposed could be a good index to estimate the images “flatness”, but it is application or parameter dependent (the size of the object being analyzed) and could be improved.

Finally, the method could be further extended to be suitable to flat-field correct even fluorescence images. However, the nature of these images is very different from brightfield and phase contrast ones and the proposed algorithm should be arranged to comply with fluorescent images. First, the background in fluorescent images should be theoretically non fluorescent or, at least, characterized by a fluorescent signal very different from that “expressed” by the cells stained with specific dyes. Accordingly, the vignetting function must be estimated directly analyzing the foreground of each image, rather than from the background. Second, the foreground fluorescent signal is quite flat: the

present background detection strategy based on the first derivative could not work properly and the central part of the stained cells could be erroneously labeled as background. However, the current strategy for the background segmentation could be exploited to segment the boundary of the cells, characterized by a high gradient, for using their signal for the vignetting estimation.

## 2.7 Acknowledgments

I would like to thank Professor Davide Donati and his staff of the Osteoarticular Research Laboratory, Bologna, Italy, for providing the image acquisition facilities, and in particular Dr. Eleonora Pagnotta and Dr. Barbara Dozza for their comments on the manuscript, Dr. Serena Duchi for acquiring and providing me with the confocal microscope images, Panagiota Dimopoulou and Lauren DeMaria for the editorial assistance; Dr. Peter Horvath and Dr. Kevin Smith of the RNAi Image-based Screening Center, in the Light Microscopy Center at the Eidgenössische Technische Hochschule (ETH), Zurich, Switzerland) for helping me in the algorithm implementation and for the useful discussions regarding the extension of the work to fluorescent images.

## 2.8 Copyright permission

I declare that for using the material previously published in [110] I obtained the rights permission by co-authors and by the Publisher (the license details are reported in Tab. 2.5).

Licensee	Filippo Piccinini
License Date	Feb 20, 2013
License Number	3092921037913
Licensed Content Publisher	John Wiley and Sons
Licensed Content Publication	Journal of Microscopy
Licensed Content Title	Multi-image based method to correct vignetting effect in light microscopy images
Licensed Content Date	Aug 17, 2012
Licensed Portion	Full article
Type Of Use	Dissertation/Thesis
Order Reference	JOMVIGNETTING20130220

**Tab. 2.5:** License details by Journal of Microscopy.



## Chapter 3

# Vignetting in fluorescence microscopy

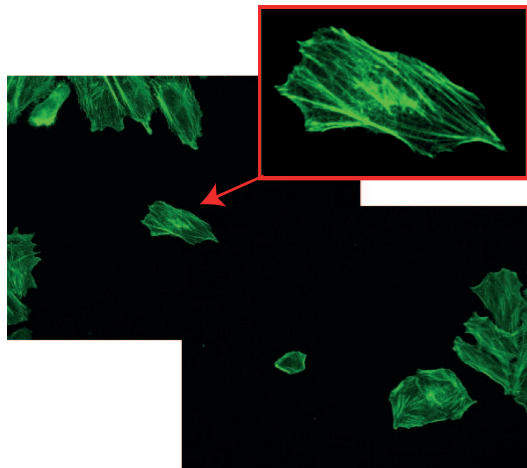


**Fig. 3.1:** Vignetting effect in fluorescence microscopy. The intensity of the cells is function of the coordinate position in the acquired images

- F. Piccinini, A. Bevilacqua, K. Smith, P. Horvath, Vignetting and photo-bleaching correction in automated fluorescence microscopy from an array of overlapping images. 10<sup>th</sup> IEEE International Symposium on Biomedical Imaging (ISBI), San Francisco, CA, USA, April 7-11, 2013

## 3.1 Introduction

As stated in Chap. 2, every image acquired using a widefield microscope is affected by *vignetting*. Such distortion is always present and often it is severe, despite the efforts of manufacturers to minimize it. The vignetting effect is particularly problematic if the images are acquired for quantitative analyses [6, 10], because the distribution of the signal into the single images is non-homogeneous and different represented objects could not be really comparable (Fig. 3.2). Accordingly, the presence of the vignetting effect can not be neglected in High Content Screening (HCS) analyses [38].

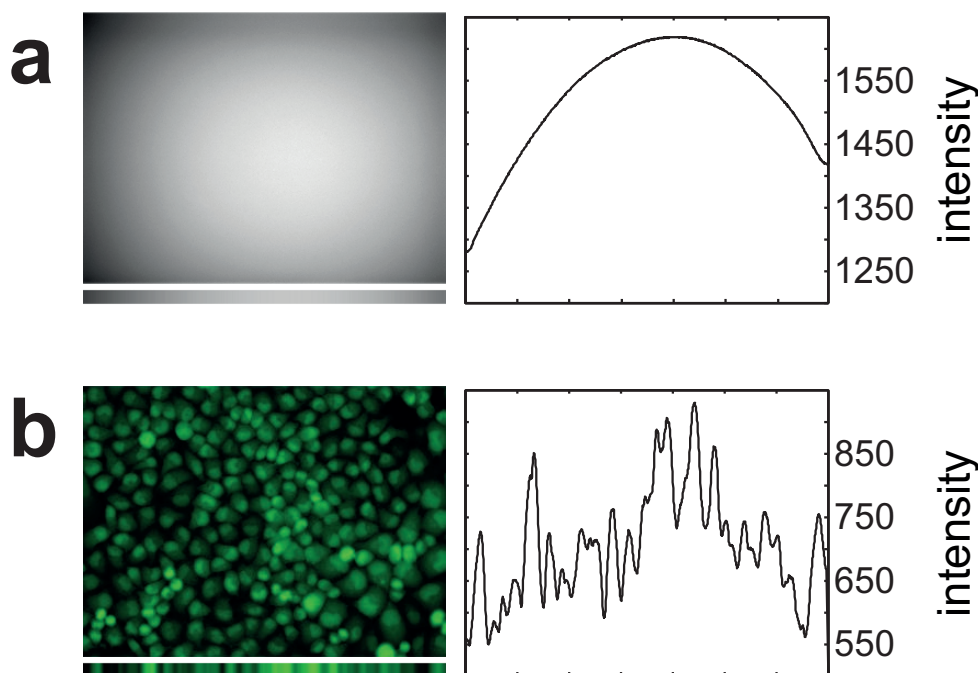


**Fig. 3.2:** Vignetting effect. Due to the vignetting effect, the distribution of the signal into the single images is non-homogeneous. In particular, (a) is related to an image of a fluorescent calibration slide, theoretically with a perfect homogeneous dyes distribution. Under the figure is reported the intensity plot of the average intensity along the  $x$  direction. The same curve is reported also in the plot in the right, where are reported the intensity values in grey levels. The distribution of the signal is far along to be flat. In (b) is shown a fluorescent image regarding the cell cytoplasm of a field of view full of cells. The conclusion for (a) is still valid.

HCS combines the efficiency of high throughput screening with the power of

---

fluorescence microscopy to extract quantitative data from complex biological systems with subcellular resolution [39]. HCS is applied from basic research to drug discovery, including genome-wide RNA interference screens, as well as compound screening. To correct the acquired images by the uneven distribution of the signal is fundamental to perform reliable measurements. In fact, in fluorescent microscopy inaccurate measures of the signal emitted from the single cells could severely mislead understanding of a whole experiment [111]. For instance, in genome-wide RNA interference screens, fluorescent-dye reporters are typically used to understand the role of the single RNA interferences. Cells are seeded in different wells and, for each well, a single RNA interference is used. Different intensity levels point out different behaviours of the cells and detecting a wrong intensity level could yield to attribute a wrong role to the specific RNA interference, hampering the whole screen [112]. Furthermore, other factors could affect the images making them not comparable [113], such as the intensity decay of the illumination source (arc lamps may decrease up to fifty per cent over their lifetime, e.g. over 1000 hours) and *photobleaching*. In particular, photobleaching is that phenomenon for which the intensity of the signal emitted by fluorescent proteins weakens due to photochemical destruction of the fluorophores due to multiple excitations.

In fluorescence microscopy (differently to what happens in light microscopy) the signal received by the camera is that emitted by the sample on a given wavelength after being activated by a different wavelength source. Typically emitting and activating signals are non-linearly related. Accordingly, in fluorescence microscopy the radiation-matter (i.e. sample) interaction plays a key role to determine an uneven signal distribution.

The different flat-field correction methods differ mainly in the approach used to estimate the vignetting function and in the underlying assumptions. In Chap. 2 Sect. 2.2 we gave an overview on the main classes and the flat-field correction formula used in widefield microscopy has been extensively explained in Chap. 2 Sect. 2.3. In general, in fluorescence microscopy the most widespread approach for estimating the vignetting function is through the acquisition of a reference image of a homogeneous fluorescent sample, for instance from a dye solution or a Fluorescence Calibration Slide (FCS). In principle, this is the most desirable approach because it directly measures the vignetting effect as deviations a deviation from an expected uniform illumination field. However, non-linearities and practical considerations make the estimation of the vignetting function *via*

a reference image problematic and, in fact, can risk a loss in the quality of the data. The fluorescent reference and the specimen have different biophysical properties and, consequently, they alter the illumination field differently. This results in a misestimation of the vignetting function. Furthermore, acquiring images of the reference is quite difficult and time-consuming, requiring an expert to carefully set the focus of the microscope, exposure time, etc. Lastly, the intensity of arc lamps, which are often used as light sources, decreases considerably over time. For large screens where image acquisition can last hundreds of hours, this can invalidate previous calibrations, making it necessary to periodically interrupt the automatic procedure to acquire new reference images.

To overcome these limitations, some methods estimate the vignetting function directly by image data. The most widely used flat-field correction approaches for HCS are the multi-image based methods implemented in CellProfiler [87, 88], two of which are described below. CellProfiler's default flat-field correction method, hereafter referred to as *CPmean*, estimates the vignetting function as the mean intensity computed over the collection of images [42]. This method makes the implicit assumption that the background signal (light emitted by the culture medium, shot noise, dark noise, and read noise) is negligible. However, in practice this assumption does not hold. In the second approach, hereafter referred to as *CPboth*, the vignetting function is estimated as in *CPmean*, but it also employs a model of the background built using the local minimum intensities from the image collection [43]. While this more sophisticated approach attempts to model the background signal, the *minimum* operator is sensitive to outliers. Furthermore, *CPmean* and *CPboth* estimate the foreground at a given location as the mean of all images at that location, while the data belonging to the foreground only (meant as the fluorescence intensity of the cells only) should be considered. As a result, CellProfiler's estimate of the vignetting function is corrupted by large contributions from the background.

Analyzing these considerations about the foreground estimation, to correctly obtain a representative vignetting function we proposed two new multi-image based methods to correct the vignetting effect conceived to work in fluorescence microscopy.

In the first method (hereafter, *LCBM* - Linear Correction Based Method) the vignetting function is estimated using the median foreground signal arising

from a large set of non-overlapping images, in order not to undergo photo-bleaching effects. The number of required images depends on the foreground confluency (percentage of the field of view occupied by cells) although, in general, the large sets of images, typically acquired in HCS, represent a perfect input for the proposed method. Accordingly, no additional acquisition is required. The standard flat-field correction formula (Eq 2.2) is used to correct the images, considering the term  $B_V(x,y)$  as corresponding to  $B(x,y)$  and  $NC$  as the mean value of  $V-B$ . The estimated vignetting function is assumed as being representative of the whole intensity range, leaving probable non-linearities of the system out of consideration. In particular, we proposed a two-step non-parametric approach to estimate  $V(x,y)$  and  $B(x,y)$  by explicitly separating foreground and background of the input images. In brief, in the first step we extracted the background by assigning each  $(x,y)$  position the mode of the distribution of the intensity values for each image at that position. The second step of our approach leverages information from the background to construct a more accurate estimate of the foreground and, consequently, of the vignetting function. At each  $(x,y)$  location, images with a pixel intensity lower than  $B(x,y)+gap$  (whose value definition will be clear afterwards) are discarded, and the remaining pixels are assumed to belong to the foreground. After applying an outlier removal step,  $V(x,y)$  is estimated by computing the mean illumination level of the remaining foreground pixels.

In the second flat-field correction method we propose (hereafter, *nLCBM* - non-LCBM), the assumption that a single vignetting function is representative of the entire intensity range is overcome by considering that fluorescence microscopy can emphasize non-linear behaviours of vignetting due to for instance interaction radiation-matters and camera response function. In particular, we propose a non-parametric multi-image based correction method and an acquisition scheme which can be implemented in any widefield fluorescent microscope, even being manual and not equipped with a  $x-y$  motorized stage. The main concept of our approach is to measure how the intensity of a particular object varies when it is re-positioned at different displacement within the image. This is accomplished by moving the microscope holder during the acquisition step and collecting a set of overlapping images surrounding the first image acquired (thus considered as the “central image”). In this way, the objects of the scene are represented in different  $(x,y)$  positions of the images acquired. It means that any pixel belonging to the central image also appears in a series of other images. This collection of appearance variation provides

us with a sparse representation of the vignetting. We exploited such sparse representations to robustly estimate the vignetting function at each image location and intensity level by grouping data from similar intensity levels. The flat-field correction is then accomplished simply by dividing each intensity level of the input images with the coupled vignetting function (normalized by its mean value). Theoretically, the method could yield improvements over the first method proposed, thanks to the non-linear correction. Despite that, the additional acquisition of the set of overlapping images have to be performed, this representing an additional task for the microscope's user.

To assess the effectiveness of the proposed methods we performed several experiments. In particular, we compared the results achieved by *LCBM* and *nLCBM* with those obtained flat-field correcting the images according to three widely used approaches:

- *CPmean*
- *CPboth*
- standard flat-field correction using the vignetting function estimated from FCS and the background surface estimated using images from regions completely free of cells (hereafter, *FCSM* - Fluorescent Calibration Slide Method)

To perform the experiments, we used an extensive dataset of images of a human genome-wide RNA interference screen. The screen was performed on fixed HeLa cells with the Red Fluorescent Protein (RFP) used to highlight the Actin filaments into the cells. Using a microscope equipped with a  $x$ - $y$  motorized stage, we acquired different sets of images, with different characteristics (all the details are in Sect. 3.3). In particular, to quantify the vignetting correction efficiency we performed two different experiments.

In the first experiment, the median foreground surface estimated using a set of non-overlapping images have been compared before and after being flat-field corrected according to the different methods tested. In particular, the *flatness* of the median foreground surfaces has been considered as the most important parameter to be measured to decree which method yields the best correction meant as the flattest signal distribution.

In the second experiment, we used a set of overlapping image pairs and we computed the Root Mean Squared Error (*RMSE*) between the overlapping regions. In this way the entire image is analyzed and both the foreground and background regions are considered, even if the background is of low interest in fluorescence microscopy. In practice, with this experiment we studied how the vignetting affects the whole single images and how much it is attenuated by the different correction approaches. The lower *RMSE* value achieved is representative as the best flat-field correction. Accordingly, the different tested approaches have been ranked to decree which method yields, on average, the best correction of the whole single images.

The performance of the methods, assessed through the different experiments and the analysis of the achieved results proved the effectiveness of both the proposed methods to achieve a flat-field, even outperforming methods using reference samples.

## 3.2 Methods compared in the experiments

To compare the two approaches we propose with the methods typically used in literature we chose as the representative one the methods implemented in CellProfiler. CellProfiler is a free open source image analysis software widely used in the medical-biological field. Various built-in functions and modules are implemented and two of which, “Correct Illumination - Calculate” and “Correct Illumination - Apply”, are those devoted to compensate for the vignetting effect in microscopy images. The first module is used to estimate the vignetting function exploiting the image data set being analyzed, so to achieve one image as the representative of the non-uniformity distribution of the intensity values in the single images. The second module is used to perform the flat-field correction, based on division or subtraction between the input image and a given vignetting curve. In addition, the module permits to manage image normalization and rescaling options. Thanks to the many parameters and combinations available in these two modules, diverse approaches can be devised to calculate and to apply the vignetting function. For a fair comparison with the multi-image based method we are proposing, we chose two CellProfiler’s multi-image approaches built using the facilities offered by the two modules.

In *CPmean*, the “Correct Illumination - Calculate” module is used to estimate the vignetting function starting from a sequence of images belonging to the same plate and fluorescent channel. To do that, the algorithm implemented inside CellProfiler simply provides the intensity mean value of the stack for each  $(x,y)$  pixel position. As stated by the authors, this solution works only if the foreground objects are evenly distributed across the images and cover most of the camera’s field of view. The images are flat-field corrected by simply performing a pixel wise division between the original images and the estimated vignetting function, post filtered with a Gaussian kernel (by letting the software choose automatically the morphological structuring element -kernel- size) and normalized by its mean value. In particular, the flat-field correction formula used is reported in Eq. 3.1:

$$I_{FFC}(x,y) = \frac{I(x,y)}{V(x,y)} \cdot \widehat{V} \quad (3.1)$$

where the bar over a variable means its mean value. Accordingly,  $\widehat{V}$  is the mean value of the estimated vignetting function.

In *CPboth*, CellProfiler was used to reconstruct the background starting from the same image stack used to estimate the vignetting function. The algorithm to reconstruct the background, implemented in the “Correct Illumination - Calculate” module, is based on the estimation of the local minimum values, performed separately for each single image of the stack, followed by a search of the lowest local minimum value of the stack in each  $(x,y)$  pixel position [43]. In this case, the flat-field correction was performed again using the “Correct Illumination - Apply” module, according to the Eq. 3.2:

$$I_{FFC}(x,y) = \frac{I(x,y) - B(x,y)}{V(x,y) - B(x,y)} \cdot \widehat{V - B} + \widehat{B} \quad (3.2)$$

$\widehat{B}$  is used to bring the intensity of the images back to the original range. In practice, in *CPboth* each input image  $I(x,y)$  is normalized using the vignetting function  $V(x,y)$  estimated in *CPmean* after subtracting the estimated background surface  $B(x,y)$  from both  $I(x,y)$  and  $V(x,y)$ .

In the screenshot items of Fig. 3.3 is reported as the CellProfiler’s parameters have been set inside the module “Correct Illumination - Calculate”, to obtain the vignetting function (Fig. 3.3a) and the background surface (Fig. 3.3b) used in the configurations tested. In particular, we always used the default parameters, also for the final Gaussian filter performed on the raw surfaces

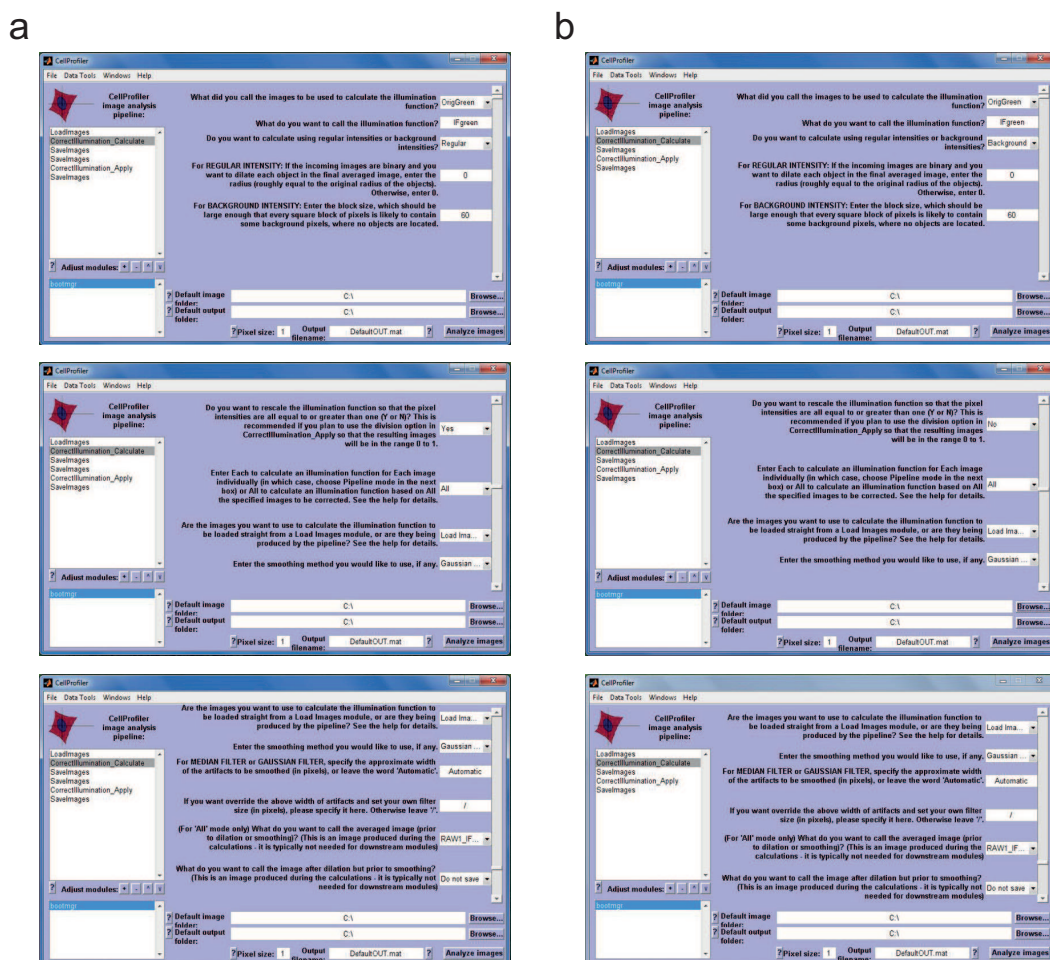


**Fig. 3.3:** Screenshots of the CellProfiler Correct Illumination modules. The reported screenshots summarize the parameters imposed to obtain the vignetting function (column **a**) and the background surface (column **b**) according to the methods *CPmean* and *CPboth*.

estimated.

It is worth noting that we used the CellProfiler modules also to perform pilot experiments for testing other configurations, such as the *CPboth* method but without subtracting the  $B(x,y)$  term in the denominator and/or the multiplicative constant of Eq. 3.2. However, the results obtained have been always worse than the ones achieved using the two configurations explained above.

*FCSM* is the last method used in our comparisons. In this method the standard

flat-field correction formula is typically used neglecting  $B_V$  term 3.3:

$$I_{FFC}(x,y) = \frac{I(x,y) - B(x,y)}{V(x,y)} \cdot \hat{V} + \hat{B} \quad (3.3)$$

Practically speaking, computing  $B_V(x,y)$  would require one additional acquisition by the microscope's user and, in practice, the term is almost always neglected. In addition, for the *FCSM* we performed exploratory experiments to test different configurations, such as the lack of the term  $B(x,y)$ , but the results obtained were always worse than those attained using the configuration explained above.

### 3.3 Materials

The experiments have been performed using fluorescence images of fixed HeLa cells, where the Actin filaments were stained with RFP. Cells have been seeded into standard plastic 384-well plates (in each plate, the wells are arranged in a  $16 \times 24$  matrix). The biological assay was a human genome-wide RNA interference screen (data courtesy of Light Microscopy and Screening Centre, ETH Zurich, Switzerland). Accordingly, cell in different wells can express a different behaviour. The microscope used to acquire the images was an inverted ImageXpress Micro Widefield (Molecular Devices, United States), with a motorized  $x$ - $y$  stage endowed with a 12-bit CoolSNAP HQ digital CCD camera (Photometrics, United States) and a Plan Fluor ELWD lens with  $20\times$  magnification. Images have been acquired with a pixel resolution of  $0.3225\mu\text{m}/\text{pixel}$ . The image resolution was  $1392 \times 1040$  pixels, 12-bit grey levels intensity, and they have been saved in TIFF format, with lossless compression. The cells confluency was generally pretty high: approximately by a visual inspection we can say that more than 50% of the images have a confluency higher than 70%.

Using the automated microscope, we acquired 6 sets of images with different characteristics:

- *Set A*: 9 non-overlapping images  $\times$  208 different wells, for a total amount of 1881 images.
- *Set B*: a stack of 1583 still images inside a single well (never imaged before).

- *Set C*: a set of 1583 overlapping images randomly acquired with a minimum 5% shift in  $x$ ,  $y$  respect to the first image acquired.
- *Set D*: a set of 252 images of different fields of view referring to a RFP commercial FCS (FluorRef, United States).
- *Set E*: a set of 37 images of fields of view free of cells containing culture medium (background) only.
- *Set F*: 100 image pairs, using 100 wells never used before (one pair from each well), imposing a 25% overlapping between each pair (shift of 50% for both image sides).

The shutter time was by default set to 100 ms and the lamp intensity has not been changed nor adjusted during the acquisition. However, the protein concentration inside the FCS was particularly high and the emitted signal resulted particularly intense. Accordingly, in order to achieve images that were not completely saturated, this required to change the exposure time to 5 ms and the intensity of the lamp just to acquire the images of *Set E*.

The different sets of images have been acquired for different purposes. In particular, in the experiments performed we used:

- A subset of 500 random images of *Set A* (hereafter, *Set A1*) for estimating the vignetting function and the background surface according to *CPmean*, *CPboth* and *LCBM* (all the details given in Sect. 3.4).
- The first 500 images of *Set B* and *C* to estimate the vignetting functions according to *nLCBM* (all the details in Sect. 3.5)
- *Set D* and *E* to perform the standard flat-field correction using the vignetting function estimated from FCS and the background surface estimated using images from field of views free of cells
- *Set F* and another subset of 500 images randomly chosen (and never used before) from *Set A* (hereafter, *Set A2*) to assess the quality of the different methods in to the different experiments

In particular, to estimate the vignetting function from the FCS and the dense

background surface estimated using images free of cells, we simply estimated the median surface (analyzing for each  $(x,y)$  pixel position the  $z$ -intensity histogram of the stack built with the images acquired) arising from *Set D* and *E*, respectively.

The experiments have been performed using to an off-the-shelf PC (Intel Core i5, CPU 2.27 GHz, 4 GB RAM). All the images used in the experiments and the codes of the developed algorithms can be provided on request [11].

## 3.4 Method based on linear correction

In the first proposed method, *LCBM*, the vignetting effect is faced following a linear correction approach and using the standard flat-field correction formula (Eq 2.2). In particular, the vignetting function is estimated using the median foreground signal arising from a large set of non-overlapping images, in order not to undergo photobleaching effects. To obtain a representative dense foreground surface, the cells confluency and the number of used images play a key role. Deciding the number of images required is a tricky task. If the set of images to be flat-field corrected is small, an additional large set of more images have to be acquired to be able to estimate in advance the vignetting function according to this method. However, the large sets of images typically acquired in HCS are enough to be used in input to the proposed method, and no extra acquisition is required.

In the method we propose the vignetting function and the background surface is estimated by explicitly separating the foreground and background of the input images. In particular, both vignetting and background are directly derived stemming from the images themselves and without exploiting any prior information.

### 3.4.1 Background modelling

Ideally, an image can be always subdivided into two complementary regions, foreground and background, where the foreground usually represents the objects of interest. Accordingly, separating foreground from background is the

first step of any segmentation procedure. In fluorescent images, this is usually achieved by detecting the background, since it has more uniform properties that make its detection easier, and the foreground is derived as the complement. In order to allow our approach to address the widest class of fluorescent images, we kept the method for the background modelling as the most general purpose as possible. Accordingly, we built a non-parametric model of the background, starting from the stack of images typically at one's disposal in HCS. Through analyzing the  $z$ -histogram for each  $(x,y)$  pixel position it is possible to estimate the 2D background that embodies both the effects of the camera noise and of the shade fluorescence of the culture medium. In fluorescence imaging, the variance of the background is far lower than the variance of the foreground. Therefore, the high number of images being analyzed in HCS is more than enough to build a significant statistics regarding the distribution of the background values for each  $(x,y)$  pixel position. Furthermore, in fluorescence microscopy even the intensity of the background pixels is always far lower than the foreground one, this often yielding noisy bimodal histograms. Accordingly, for each  $(x,y)$  pixel position we assumed the intensity corresponding to the *first global peak* of the  $z$ -histogram as the representative background value. As far as the implementation is concerned, for each  $z$ -histogram we computed the first derivative and we analyzed the sign function to search peaks and valleys for detecting the first maximum peak. A  $z$ -histogram of a randomly chosen  $(x,y)$  pixel position and the 3D profile of the background surface are shown in Fig. 3.4. The final background is then obtained by simply filtering the raw surface estimated performing a common median  $5 \times 5$  filter. Our approach to model the background is robust and general. The only case where it fails is when the cell confluency in each image is very high. For instance, in exploratory experiments we saw that mean cell confluency higher than 95% could be problematic. However, so a high confluence is rare and in that case we suggest to acquire one more image made of background only, manually selecting a field of view free of cells.

### 3.4.2 Vignetting estimation

Stemming from the  $z$ -histogram of each pixel we aim to define, for each  $(x,y)$  pixel position, a threshold to separate foreground from background. In general, the distribution of the background values is either quite symmetric around its

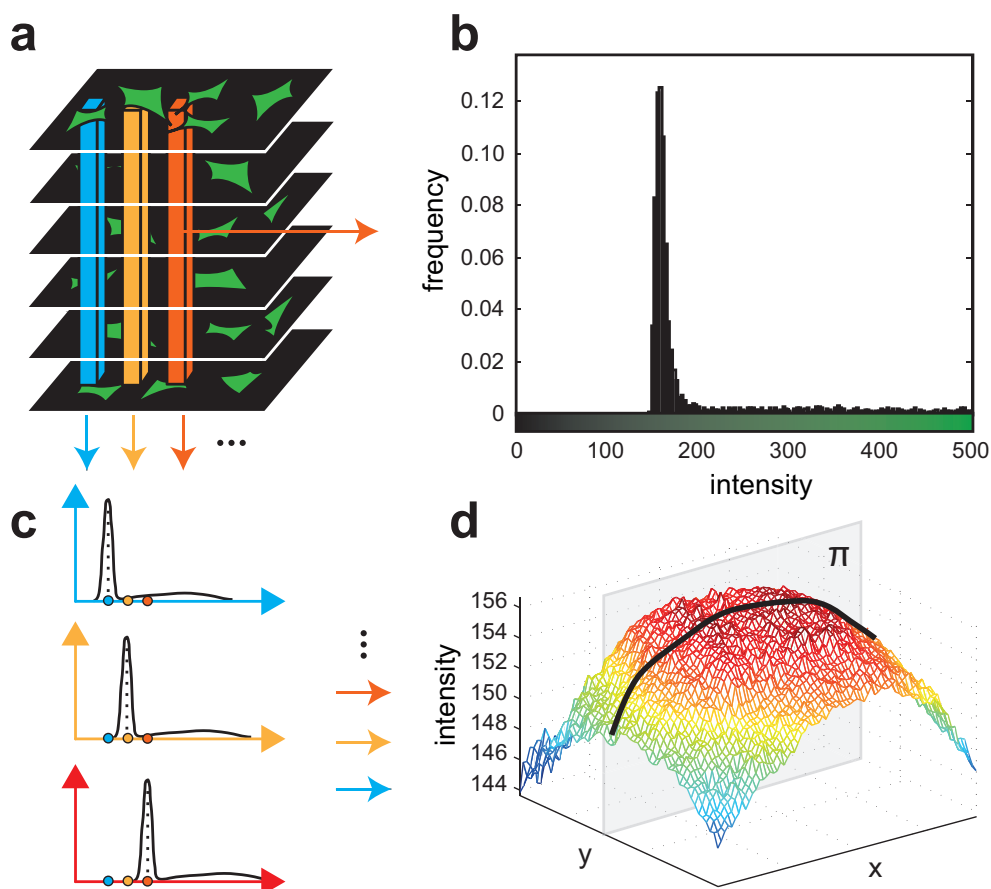


**Fig. 3.4:** Model of background. Starting from the stack of images (a), the background is modelled analyzing the  $z$ -histogram for each  $(x,y)$  pixel position (b). The range of values of the background is lower and narrower than the range of the foreground, so the background is modelled searching for the first global peak of histograms for each  $(x,y)$  pixel position. Different  $(x,y)$  pixel positions are characterized by different  $z$ -histogram (c). In particular, the histograms are characterized by a very similar shape but they are shifted. By collecting the intensity values of the peaks in a 2D mask (d) is possible to reconstruct a dense robust background very quickly.

maximum peak  $m$  or at most slightly right-skewed, since the foreground values are most likely higher than  $m$ . Let  $p$  be the minimum grey level value estimated for each  $(x,y)$  pixel position.  $gap$  is the distance in grey levels between  $m$  and  $p$  (Eq. 3.4):

$$gap = m - p \quad (3.4)$$

The threshold  $T$  is computed as  $T = m + gap$ , this being adaptive for each  $(x, y)$  pixel position. To filter out local noise estimations of  $gap$ , we used for each  $(x, y)$  position a fixed value, determined as the mean value plus 3 standard deviation (std) of the  $gap$  values estimated. In order to achieve a reliable estimate of the foreground curvature, for each  $(x, y)$  pixel position the median value has been chosen (Fig. 3.5). Finally, the foreground surface was denoised

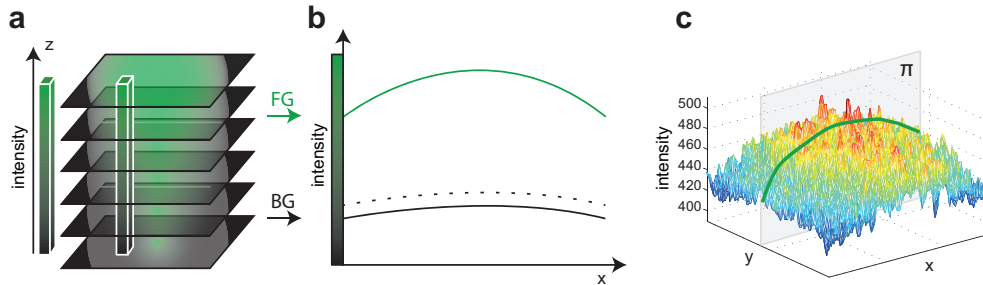


**Fig. 3.5:** Model of foreground. Once the background is reconstructed, it is possible to determine the foreground values for each  $(x, y)$  pixel position. These values are extracted sorting the stack (a) and using the background as threshold. For each  $(x, y)$  pixel position, the median of the remaining  $z$ -histogram values is a good approximation of the vignetting function. In (b) is reported a schematic representation of a line profile of the foreground estimation given by its intersection with the plane  $\pi$  for a  $x$ -line at a fixed  $y$  coordinate. The black line represents the  $x$ -values of background for that  $y$  coordinate. The black-dotted line the threshold used to separate foreground from background. The green line represents the median of the  $z$ -histogram values labelled as foreground. In (c) is reported the 2D mask of the foreground values, used as vignetting function.

using first a median filter to remove possible isolate peaks followed by a mean filter to remove high frequency components. For both filters the side of the square kernel mask has been fixed to 10% of the image's largest side, this being compatible with the size of a cell visualized at a magnification factor  $10\times$ .

### 3.4.3 Linear flat-field correction

Referring to the standard flat-field correction formula (Eq 2.2), we used as  $V(x, y)$  and  $B(x, y)$  the foreground and background surfaces estimated as explained above. In addition, since the input image and the foreground curve undergo the same systematic error, we subtracted  $B(x, y)$  by both numerator and denominator. Accordingly,  $B_V(x, y)$  is considered as corresponding to

$B(x,y)$ . The standard formula thus becomes the same reported in Eq. 3.2, where  $NC$  is the mean value of  $V-B$ . In this way, the estimated vignetting function is assumed representative of the entire intensity range without considering possible non-linearities of the system, such as the camera response function and circuitry of the camera sensor.

### 3.5 Method based on non-linear correction

The second proposed flat-field correction method (*nLCBM*) models spatial and radiometric non-linear vignetting properties, yielding a near perfect vignetting correction in any given intensity level. The assumption that one single vignetting function can be representative of the entire intensity range is abandoned in order to consider a non-linear flat-field correction approach. An ensemble of representative vignetting functions is estimated using overlapping images acquired directly from the sample, using a fluorescent microscope, whether it is equipped with a  $x$ - $y$  motorized stage or not. Our approach relies on measuring the intensity of the same objects acquired at different image displacements (Fig. 3.6), by simply moving the microscope stage to achieve a set of overlapping images surrounding the first image acquired (considered as the “central image”, Fig. 3.7). As a result of the acquisition procedure, any given pixel belonging to the central image appears at different displacements in a series of other images. The collection of variations of appearance of objects expected as being unchanged provides us with a sparse representation of the vignetting function. We exploited such sparse representation to robustly estimate the vignetting function *at each image location and intensity level* by grouping pixels with a similar intensity level. However, in fluorescence microscopy acquiring repeated images of the same objects make them to be affected by the so called photobleaching, that is a non-linear intensity decay of the emission light due to the destruction of fluorophores. Accordingly, before computing the vignetting functions, we needed to model the decay so to recover the intensity values before photobleaching. To this purpose, we acquired a sequence of still images then arranged into a stack. In particular, we acquired the same number of images of the set used for the vignetting estimation. The decay of the intensity value of each pixel is used to obtain reference pixel-based time (time=image number) intensity curves and couples of values made of actual and target (i.e., starting) intensities. The latter is then used to

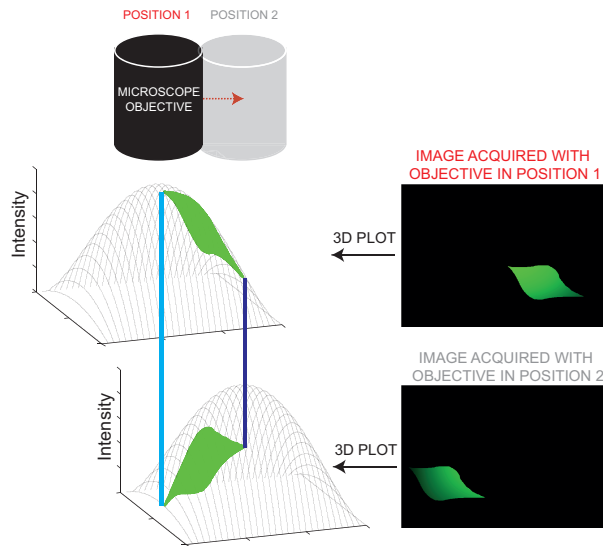


**Fig. 3.6:** Object's intensity depending on the position in the image. Our approach learns the vignetting effect by observing the intensity's change of an object acquired at different image displacements. In this Figure, a fluorescent cell with a homogeneous signal undergoes a change in appearance, due to vignetting, as the position of the lens changes.

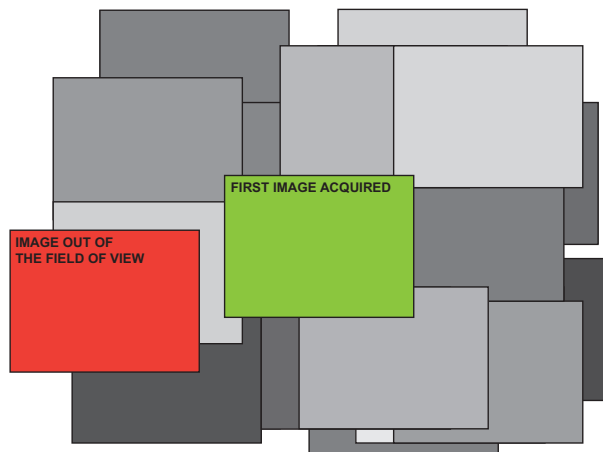


**Fig. 3.7:** Non-linear flat-field correction method: acquisition strategy. A set of images are manually acquired *trying* to capture all the images overlap the first acquired. The images are acquired in a random order.

normalize the actual intensity values of the set of overlapping images acquired to estimate the vignetting functions. As a consequence, our method results in

---

a set of vignetting surfaces built for different intensity levels. The non-linear flat-field correction of the input images is then performed pixel-wise, by simply dividing each intensity level of the input images with the coupled vignetting function (normalized by its mean value). Theoretically, the method can improve the first method proposed (*LCBM*), mainly thanks to the non-linear correction performed, though an additional acquisition of a set of overlapping images must be done and this requires to perform one more operation by the microscope's user.

In Fig.3.8 a schematic flow chart of the proposed approach's pipeline is pre-



**Fig. 3.8:** Schematic flow chart of the non-linear flat-field correction method. First, a set of partially overlapped images is acquired directly from the sample, manually moving the microscope. Then, another set made of the same number of images is acquired with still microscope. This second set is used to estimate the photobleaching decay curves required to correct the set of partially overlapped images. Finally, the ensemble of vignetting functions is estimated to be subsequently employed to perform the flat-field correction of the images then acquired.

sented. Going more in detail, we can subdivide the flat-field correction approach in the following three stages:

- Photobleaching modelling
- Vignetting functions estimation
- Non-linear flat-field correction

### 3.5.1 Photobleaching modelling

To precisely estimate the vignetting functions, measuring the intensity of the same objects in a set of different overlapped images, the images must be photobleaching corrected in advance. To this purpose, we used a stack of still images (Fig. 3.9a). The decay curves have been estimated simply looking at the intensity changes for each pixel position. For better statistical significance, the

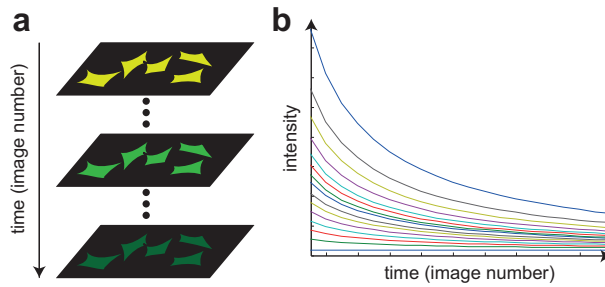


**Fig. 3.9:** Modelling of the photobleaching decay. (a): to evaluate the intensity decay due to photobleaching a sequence of still images is acquired, without moving the microscope. The intensity values decrease as the number of images acquired increase. (b): the intensity decay curves due to the photobleaching effect are built using the time sequence of the intensity changes for every  $(x,y)$  pixel position. The curves are then used as intensity normalization function to recover the pixel values.

curves obtained were binned and interpolated to obtain robust decay curves for every intensity value present in the first images of the sequence (Fig. 3.9b). Finally, we corrected by photobleaching each other acquired image mapping back to the intensity of the first acquired image all the intensity values. To this purpose, the estimated photobleaching decay curves are used as a normalization factor.

### 3.5.2 Vignetting functions estimation

The ensemble of representative vignetting functions is estimated measuring the intensity of the same objects acquired at different image displacements. In particular, a representative vignetting function for each different intensity level in the first image is achieved through registering the overlapping images acquired. For the global registration of the images we used a simple approach: we compared the first image acquired (the central image), considered as reference, with the remaining images, using the Phase Correlation algorithm (details can be found in Appendix 6) to estimate the registration. In particular, image pairs with less than 10% of overlap or with a mean difference in the overlap higher than 5% of the whole intensity range have been discarded to avoid possible registration errors. We repeated the process choosing a few more different images as the new reference. In order to obtain less noisy registrations,

we computed the median between the different registrations gathered. Once the registrations have been computed, for each pixel of the central image it is possible to obtain a vignetting surface. In particular, starting from the sparse representation of the vignetting surface, we estimated the dense representation using Thin Plate Spline (TPS) fitting. Nevertheless, to reduce the computational complexity in the experiments performed we binned the intensity range in levels equally spaced (we binned into 100 levels, recalling that the images are 12-bit depth). Again, to bound the computational burden, for each level we chose 10 pixels (with the lowest gradient, from the central image) to be used to estimate as many surfaces. The pixels chosen have the lowest gradient, since pixels from high-gradient regions are particularly sensitive to small registration errors (Fig. 3.10). Finally, in order to make the ultimate vignetting

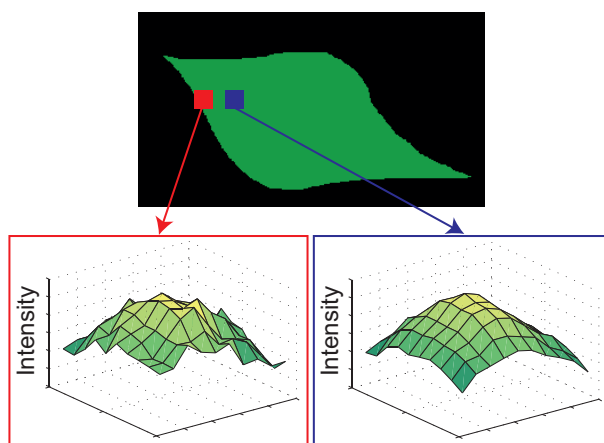


**Fig. 3.10:** Disadvantage of high intensity gradient pixels. Due to small registration errors, surfaces estimated using pixels from high gradient regions (bottom left) can result noisy if compared with the surface estimated using pixels from homogeneous intensity regions (bottom right).

function estimated for each level more robust, it has been achieved by simply computing the average of the single surfaces estimated.

### 3.5.3 Non-linear flat-field correction

The standard model for the vignetting correction assumes a linear image formation model. Correction is accomplished by removing the additive  $B(x,y)$

term, then normalizing the image by the vignetting function (Eq. 2.2). In case of the proposed non-linear approach, a set of vignetting functions related to different intensity levels are estimated. Accordingly, the non-linear flat-field correction is accomplished for each intensity level and the formula can be written as reported in Eq. 3.5:

$$I_{FFC}(x,y) = \frac{I(x,y)}{V_{I(x,y)}(x,y)} \cdot \widehat{V_{I(x,y)}} \quad (3.5)$$

where  $(x,y)$  are the image plane coordinates. Since not all the grey levels have their own vignetting function (due to the finite range of the central image and quantization needed to reduce computational burden) each surface  $V_{I(x,y)}$  is estimated through bilinear interpolation of the two adjacent curves previously estimated, whose intensity value in the  $(x,y)$  position is the closest one to that in the corresponding position of  $I$ . A specific pixel of  $V_{I(x,y)}$  in position  $p$  and  $q$  is then indicated as  $V_{I(x,y)}(p,q)$ . Using the given formula, each pixel of the original image is vignetting corrected by a specific vignetting function.

## 3.6 Experimental results

In order to compare the effectiveness of *LCBM* and *nLCBM* with that achieved by the other approaches mentioned in Sect. 3.2, we carried out two different experiments. In the first experiment, we measured the *flatness* of the median foreground surface, extracted from a set of non-overlapping images, before and after being corrected according to the different methods tested. This gives us a quality measure of the general effectiveness of the different flat-field corrections: the ideal outcome of any correction method is a perfectly flat signal distribution of the foreground (in fluorescence the background signal is typically neglected). Instead, in the second experiments we used overlapping image pairs to quantitative monitoring the effectiveness of the different flat-field corrections on the entire image, considering both foreground and background regions. The overlapping regions represent a meaningful test-bed to assess the effectiveness of the vignetting correction: theoretically, no photometric misalignments should be visible if the stitched images are perfectly flat. To this purpose we used the *RMSE* on the overlapping regions, that gives an averaged measure of the images' differences. This permits to assess how much the different correction approaches attenuate the vignetting effect on the whole image.

As already stated in Sect. 3.3, for both the experiments we used the vignetting function estimated from *Set D* and the background surface estimated from *Set E* as the references for the standard flat-field correction using FCS and the background estimated using images free of cells (both used in *FCSM*). To estimate the vignetting function and the background surface according to *LCBM*, *CPmean* and *CPboth*, we used the 500 images of *Set A1*. Instead, to estimate the set of vignetting functions according to *nLCBM*, we used the first 500 images taken from both *Set B* and *C*.

### 3.6.1 Flatness of the foreground signal

In the first experiment, in order to measure the *flatness* of the median foreground surface we used the 500 images of *Set A2*. In particular, in order to obtain the foreground mask we segmented the images using as a global threshold the maximum value of the background surface estimated directly from the images using the CellProfiler module already explained in Sect. 3.2. Despite the simplicity of the segmentation method, we can say that the masks obtained are good enough for our purpose (Fig. 3.11). Then, we arranged the 500 images into a stack and computed the *z*-median foreground surface, before and after flat-field correction performed according to the different methods. Finally, the *flatness* of the median foreground surfaces has been achieved through computing the std of the distribution of the local means of the surface, computed on a square moving window whose side has been fixed at 10% of the largest side of the images, this being compatible with the size of a cell visualized at a magnification factor 10 $\times$ . The lowest *flatness* value indicates the method achieving the general better flat-field correction of the foreground signal distribution.

The *flatness* values obtained by correcting the 500 images of *Set A2* according to the different methods are reported in Tab. 3.1. Furthermore, the simple std

	UNCORRECTED	<i>FCSM</i>	<i>CPmean</i>	<i>CPboth</i>	<i>LCBM</i>	<i>nLCBM</i>
<i>flatness</i>	3.33	3.52	2.21	2.37	1.75	1.81
$\sigma$	4.22	4.41	3.59	3.74	3.05	3.15
Rank	5 <sup>th</sup>	6 <sup>th</sup>	3 <sup>rd</sup>	4 <sup>th</sup>	1 <sup>st</sup>	2 <sup>nd</sup>

**Tab. 3.1:** Flatness and std of the foreground distribution before and after the different flat-field corrections.

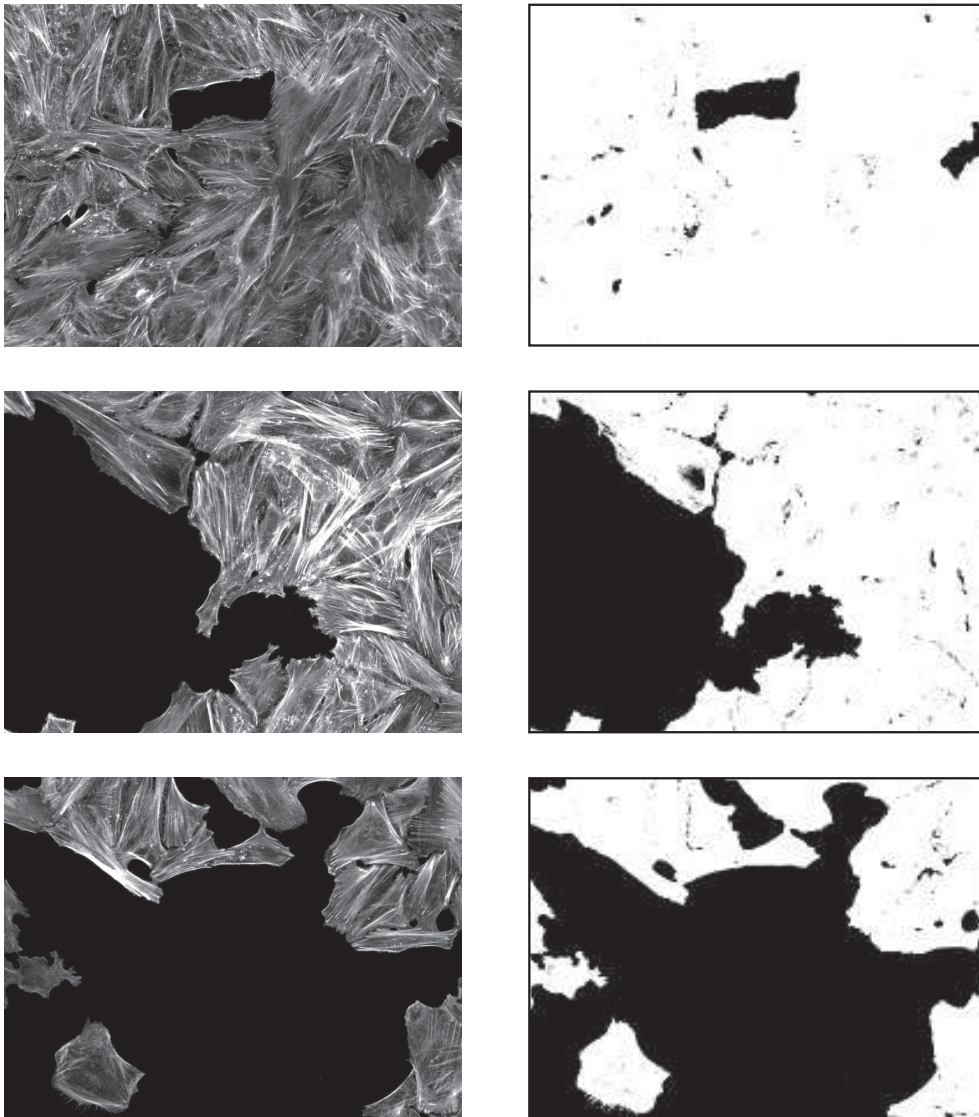


**Fig. 3.11:** Foreground masks. To segment the foreground of the single images referring to Actina filaments we simply used as global threshold the maximum value of background surface estimated using CellProfiler.

( $\sigma$ ) values of the median foreground surfaces are reported in the second line. The two lower *flatness* values are those related to *LCBM* and *nLCBM*, this proving the effectiveness of both the methods to flat-field correct the distribution of the foreground signal. The third line of Tab. 3.1 reports the rank of the method according to the *flatness* values achieved, that is the same achieved by  $\sigma$ . The worst result is not due to the original images, but to *FCSM*. This can be

explained directly looking at the 3D visualization of the foreground surfaces. Fig. 3.12 reports 3D visualizations of the median foreground surfaces obtained

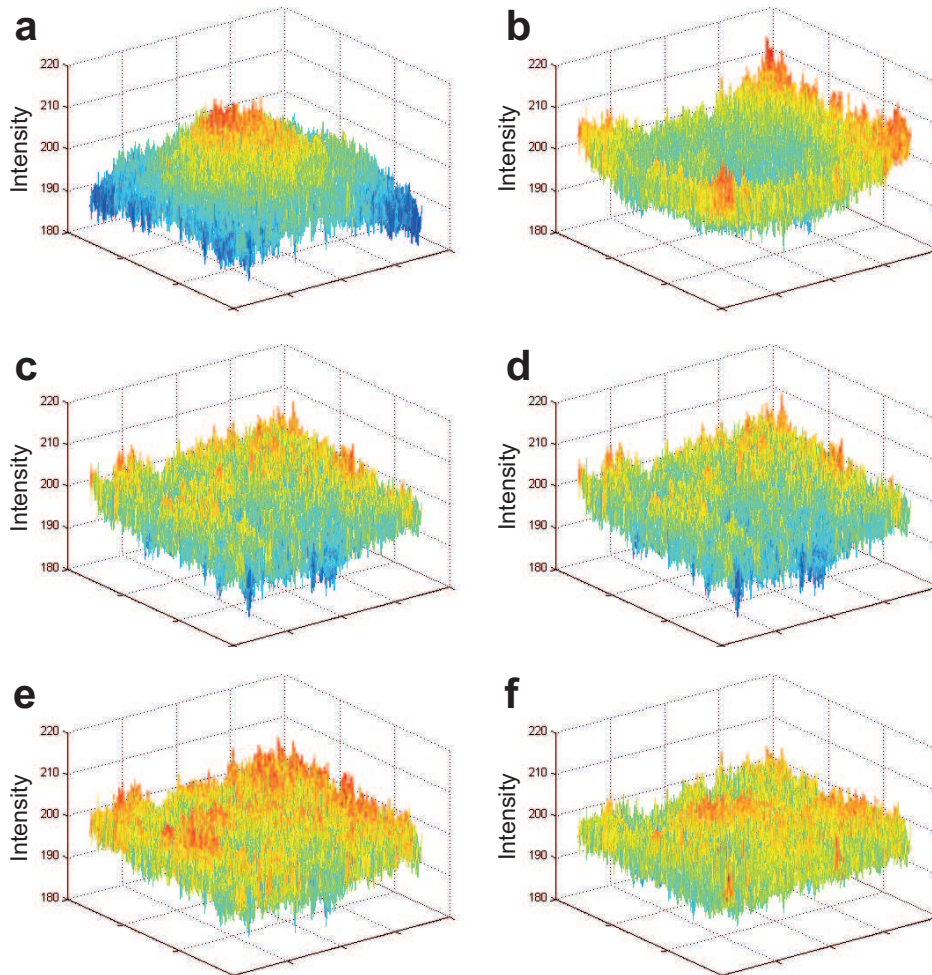


**Fig. 3.12:** Median foreground signal distributions. The reported surfaces are the 3D representation of the median foreground signal distribution estimated using the images uncorrected (a) and corrected according to *FCSM* (b), *CPmean* (c), *CPboth* (d), *LCBM* (e) and *nLCBM* (f).

flat-field correcting the original images according to the different methods. Even at sight, it is possible to confer that the flattest surfaces are the two related to *LCBM* and *nLCBM*. Furthermore, it is particularly interesting to note that *FCSM* strongly over-corrected the median foreground surface and this is probably the reason why their *flatness* and  $\sigma$  are the worst ones.

### 3.6.2 Flatness of the whole images

In the second set of experiments we used the 100 overlapping image pairs of *Set F* to compute the *RMSE* (according to Eq. 3.6) only in the overlapping region of each image pair, before and after correcting the images according to the different flat-field correction methods tested (Fig. 3.13).

$$RMSE_{(OP,BP)} = \sqrt{\frac{\sum_x \sum_y [OP(x,y) - BP(x,y)]^2}{P}} \quad (3.6)$$

$BP(x,y)$  and  $OP(x,y)$  are 2D matrices related to the Back-Projected (*BP*, overlapping part) and Overlapped Part (*OP*), respectively, and  $P$  is their number of pixels. The *RMSE* has been chosen since the differences we want to

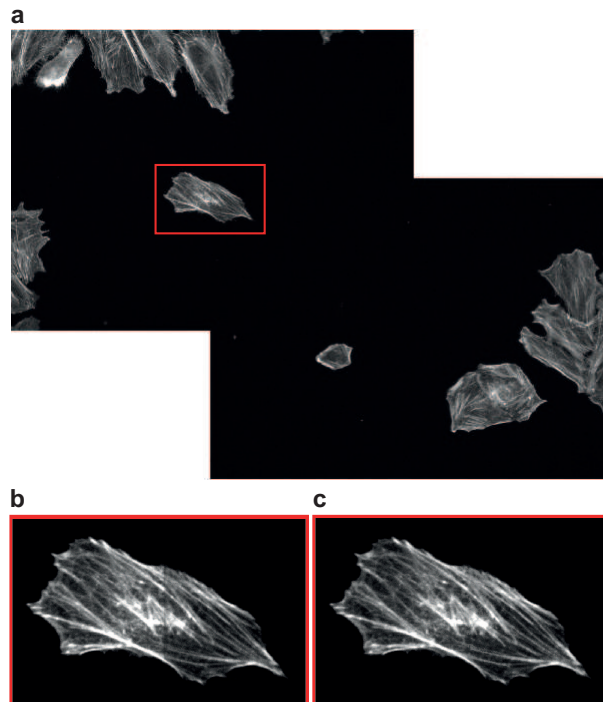


**Fig. 3.13:** Overlapping image pair. (a): a pair of overlapping uncorrected images used for testing. (b): a close-up of the uncorrected test pair reveals the effect of vignetting where the images are stitched. (c): vignetting is noticeably reduced in the same region after flat-field correction (in this case performed according to *nLCBM*).

measure are well distributed all over the images and no spikes or significant

local changes are present. The histogram of the sign differences has typically a Gaussian distribution (Fig. 3.14). The *RMSE* permits to assess how much the

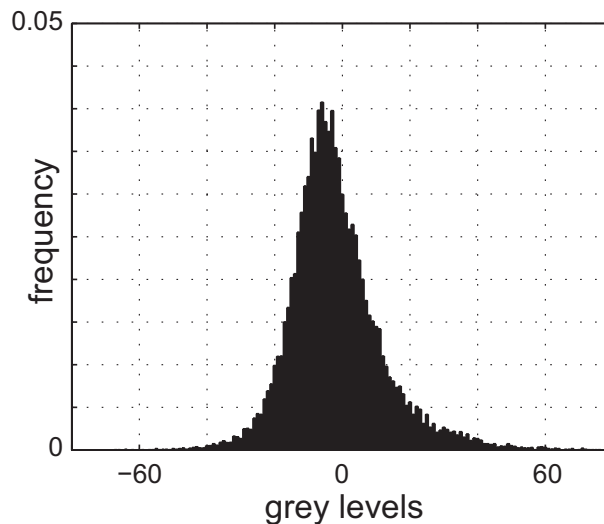


**Fig. 3.14:** Frequency histogram of the sign differences in the image overlapping. In  $x$  the intensity values in grey levels related to the sign differences obtained subtracting a pair of overlapping regions. In  $y$ , the frequency values.

different correction approaches attenuate the vignetting effect on the whole image, meant as both foreground and background regions (although typically the background is not analyzed in fluorescent microscopy). In particular, first we corrected by photobleaching the second image of each image pair, according to the method explained in Sect. 3.5.1. Then, we computed three different indices:

- the average *RMSE*: average value of the *RMSE* achieved in the 100 image pairs
- the average improvement: computed by normalizing each single *RMSE* value by the *RMSE* achieved by the original uncorrected images and then subtracting to 1 the obtained value.
- the ranking score: a score based on how many times a given method ranked first (i.e., obtained the best *RMSE* value), second, etc.

In Tab. 3.2 the ranking scores, the average  $RMSE$  values (meanstd), the average improvements and the methods rank (computed according to the average  $RMSE$ , the average improvement and the number of the 1<sup>st</sup> positions achieved by the different methods) are reported. Although the rank obtained (reported

	UNCORRECTED	$FCSM$	$CP_{mean}$	$CP_{both}$	$LCBM$	$nLCBM$
Score 1 <sup>st</sup> position	0	2	1	4	<b>74</b>	19
Score 2 <sup>nd</sup> position	0	7	13	15	23	<b>42</b>
Score 3 <sup>rd</sup> position	0	18	22	<b>35</b>	2	23
Score 4 <sup>th</sup> position	0	26	30	<b>32</b>	1	11
Score 5 <sup>th</sup> position	4	<b>47</b>	30	14	0	5
Score 6 <sup>th</sup> position	<b>96</b>	0	4	0	0	0
$RMSE$ (mean±std)	15.41±3.82	13.14±3.64	13.15±3.45	13.05±3.58	12.85±3.60	12.98±3.60
Average improvement	–	15.14%	14.12%	15.68%	17.07%	16.09%
Rank	6 <sup>th</sup>	4 <sup>th</sup>	5 <sup>th</sup>	3 <sup>rd</sup>	1 <sup>st</sup>	2 <sup>nd</sup>

**Tab. 3.2:** Ranking scores, average  $RMSE$ , average improvement and methods’ rank computed using 100 overlapping image pairs.

in the last line of Tab. 3.2) is different from that reported in Tab. 3.1, the two best methods still are  $LCBM$  and  $nLCBM$ . As expected,  $LCBM$  still achieved the best results (in 75%), since the main behaviour of vignetting is linear, but 25% is spread out of the other methods. Accordingly, we performed deep analysis of the remaining methods, also performing additional experiments to go through the motivation of some behaviours. Some considerations are reported below for each method tested, and these could help to better understand the results of Tab. 3.2.

### Method ranked 5<sup>th</sup>: $CP_{mean}$

As highlighted in the row “Score 6<sup>th</sup> position” of Tab. 3.2,  $CP_{mean}$  is the only method achieving scores even worse than the uncorrected images. The reason could be that  $CP_{mean}$  is the only method that does not provide a background subtraction and correct each intensity level of the images by a single vignetting function (see Eq. 3.1). Accordingly, to use  $CP_{mean}$  to correct images containing a large percentage of background is not a good choice. To confirm that, we sorted the image pairs according to the percentage of background in their overlapping region. In fact, in the 5 image pairs having the lowest foreground percentage,  $CP_{mean}$  for 4 times achieved the worst  $RMSE$ . The  $RMSE$  values achieved by the different method in the 5 lower-foreground-percentage image

pairs are reported in Tab. 3.3:

Foreground percentage	UNCORRECTED	<i>FCSM</i>	<i>CPmean</i>	<i>CPboth</i>	<i>LCBM</i>	<i>nLCBM</i>
3%	3.02	2.52	<u>4.62</u>	2.58	2.36	2.81
13%	5.22	5.03	<u>6.15</u>	5.04	4.92	5.04
23%	7.60	7.03	<u>7.87</u>	7.00	6.99	7.09
35%	<u>8.85</u>	7.98	8.36	7.76	7.68	7.69
42%	9.29	8.77	<u>9.33</u>	8.67	8.60	8.65

**Tab. 3.3:** *RMSE* values in the 5 lower-foreground-percentage image pairs. For each row the worst *RMSE* value is underlined.

#### Method ranked 4<sup>th</sup>: *FCS*

Probably, the motivation standing behind the 4<sup>th</sup> rank position achieved by *FCSM* is the nature of the object used to estimate the vignetting function: a slide with an huge amount of fluorescent dye, whose intensity is much higher than the sample’s one. Also, in the presence of negligible non-linearities of the system, to estimate the vignetting function using a higher intensity signal could be not a good choice if the vignetting function has to be used afterwards to correct intensity signals far lower. To prove that the intensity range of the source used to estimate the vignetting function plays a key rule, we studied the two cases where *FCSM* ranked first (row “Score 1<sup>st</sup> position” of Tab. 3.2). Looking at the overlapping area of the two image pairs (Fig. 3.15), we immediately noted that they were characterized by a large amount of background and very bright spots of intensity. The vignetting function estimated from the *FCS* could be right for flattening the bright spots of the intensity. In addition, the background subtraction (see Eq. 3.3) should help correcting images with large amount of background. Images characterized by bright spots and large amount of background are typically high contrast images. Accordingly, to prove the effectiveness of *FCSM* for flat-field correcting high contrast images, we computed the std (often used as a contrast measure) of the overlapping regions of the 100 image pairs and we sorted the *RMSE* values according to the std values obtained. The two times the *FCSM* was the best fall in the first 12 high contrast image pairs, this pointing out the good tendency of *FCSM* to correct images with bright spots and large amount of background. However, a deeper characterization of the method should be carried out through a multi-feature analysis based, for instance, contrast, intensity distribution, range intervals.

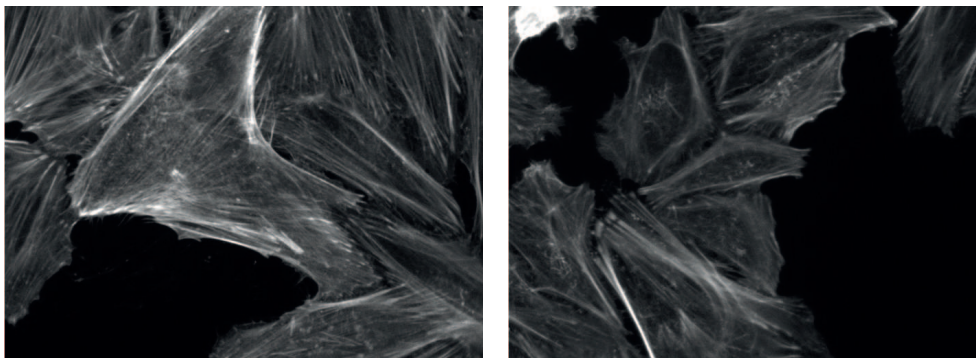


**Fig. 3.15:** Overlapping areas of the image pairs where *FCSM* performed as the best method. They are characterized by a significant amount of background and very bright spots of intensity.

### Method ranked 3<sup>rd</sup>: *CPboth*

*CPboth* is very similar to *CPmean*, but the background subtraction should fix the problems discussed dealing with *CPmean*. In particular, we analyzed how the different methods flat-field correct the background. To this purpose, we reused the 100 image pairs of *Set F*, but this time we computed the *RMSE* using only in the background pixels in the overlapping regions. In Tab. 3.4, the ranking scores, the average *RMSE* values (meanstd), the average improvements and the methods rank (computed according to the average *RMSE* and the average improvement achieved by the different methods) are reported. As

	UNCORRECTED	<i>FCSM</i>	<i>CPmean</i>	<i>CPboth</i>	<i>LCBM</i>	<i>nLCBM</i>
Score 1 <sup>st</sup> position	0	13	21	<b>53</b>	12	1
Score 2 <sup>nd</sup> position	1	<b>31</b>	6	27	<b>31</b>	4
Score 3 <sup>rd</sup> position	3	<b>33</b>	8	11	30	15
Score 4 <sup>th</sup> position	6	15	9	7	18	<b>46</b>
Score 5 <sup>th</sup> position	17	7	<b>36</b>	2	9	29
Score 6 <sup>th</sup> position	<b>73</b>	1	20	0	0	6
<i>RMSE</i> (mean±std)	8.03±2.93	6.75±2.43	7.10±2.05	6.60±2.39	6.77±2.45	6.96±2.43
Average improvement	–	15.24%	6.51%	16.86%	15.13%	11.96%
Rank	6 <sup>th</sup>	2 <sup>nd</sup>	5 <sup>th</sup>	1 <sup>st</sup>	3 <sup>rd</sup>	4 <sup>th</sup>

**Tab. 3.4:** Ranking scores, average *RMSE*, average improvement and rank computed considering the background pixel of 100 overlapping image pairs.

expected in background, *CPboth* was the method achieving the best average *RMSE*, average improvement and the highest number of lower *RMSE* (the best

score achieved 53 times). It means that the model of background estimated in *CPboth* is accurate and the background subtraction performed is a crucial task for the flat-field correction of the background. However, we must recall that this affects also in the evaluation of the *RMSE* in the whole images.

### Method ranked 2<sup>nd</sup>: *nLCBM*

We know from Tab. 3.4 that *nLCBM* does not work too well for flat-field correcting the background (it was the best one time only). This is probably due to the absence of non-linearities in the intensity range of the background, where typically the fluorescent signal is mainly related to the autofluorescence of the culture medium or small fluorescent particles (corpuscles or debris) free of moving in the liquid. Furthermore, looking at the set of vignetting functions estimated, one can see that the functions do not cover the entire range of the images. In particular, the mean value of the highest vignetting function is far lower than the maximum values of the images to be corrected. According to Eq. 2.2, also the values higher than the mean values of the highest vignetting function estimated are corrected using that function and this could yield errors. To prove that *nLCBM* does not work properly with images with high intensity values, we first sorted the 100 image pairs according to the mean intensity value of their overlapping region. Then, we checked how many times *nLCBM* achieved the lower *RMSE*, dividing the images into four groups (of equally spaced intensity levels) according to their mean value (the first group has the highest mean). As reported in Fig. 3.16, *nLCBM* achieved only 2 scores in the interval containing the images with the highest mean intensity value. It proves that *nLCBM* is not able to flat-field correct properly images characterized by high intensity values. Furthermore, to obtain 0 score in the last interval (containing the images with the lowest mean intensity value) proves again that *nLCBM* does not work well with images containing large amount of background. To conclude, we can state that to increase the representativeness of the set of vignetting functions estimated, a set of images covering an intensity range larger than the range of the images to be corrected must be acquired.

### Method ranked 1<sup>st</sup>: *LCBM*

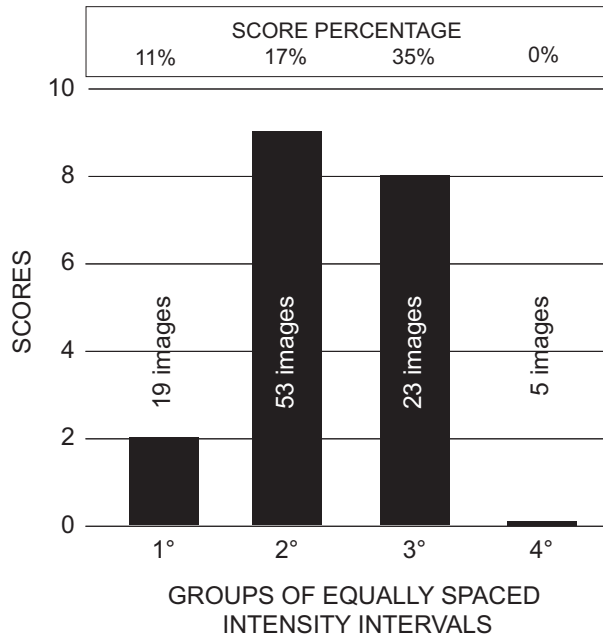


**Fig. 3.16:** Histogram score of  $nLCBM$ . We sorted the image pairs according to their mean intensity value in the overlapping region, then we checked how many times (scores)  $nLCBM$  achieved the lower  $RMSE$ , dividing the images into 4 groups of equally spaced intensity levels (the first group has the highest mean). Over the bars is reported the number of images included in the intensity interval and the score percentage.

The method is general purpose and always performed well. Nevertheless, the results reported in Tab. 3.4 proved that  $CPboth$  provides a better background model and using it in  $LCBM$  could yield slight improvements.

## 3.7 Conclusion and future work

### 3.7.1 Conclusion

In this chapter we described the two methods we developed to flat-field correct images acquired with widefield fluorescence microscopes. The first method we proposed ( $LCBM$ ) estimates the vignetting function using a large set of (non-overlapping) images, like those typically acquired in high content screenings.

The flat-field correction is performed according to the standard linear approach where the background subtraction is performed first and the images are then corrected (“done flat”) by normalizing by the vignetting function. Instead, in the second method (*nLCBM*) the linear approach is abandoned in favor of a non-linear approach, where each intensity level of the images is corrected by its own vignetting function. A set of vignetting functions is estimated using a sequence of overlapping images, acquired moving the microscope holder around a central image. The presentation of the same objects in different image’s coordinates gives a sparse representation of the vignetting functions. In particular, the images are registered and a vignetting function is estimated for each intensity level present in the central image. The estimated vignetting functions are then representative of the non-linearities of the system. The flat-field correction is then performed pixel-wise, simply normalizing each pixel of the images by the related vignetting function.

We compared the two proposed methods with different approaches widely used in literature by carrying out two different experiments. The purpose of the first experiment was finding out which method achieved the best result in the flat-field correction of the median foreground surface estimated using a set of non overlapping images. The reason behind this choice is that in fluorescence microscopy usually the background is neglected and the only interesting signal is the foreground, meant as the signal emitted by the cells. Accordingly, the method achieving the flattest foreground surface could be considered the best method to correct the vignetting effect in fluorescence. *LCBM* achieved the best result, immediately followed by *nLCBM*. Furthermore, the result achieved using fluorescent calibration slides (the most largely used approach in literature) was very interesting and somehow unexpected: the foreground surface result overcorrected and less flat than the one referring to the original uncorrected images.

To analyze also the effectiveness of the different approaches in the flat-field correction of the whole images, considering both foreground and background regions, we performed a second experiment where we computed the Root Mean Squared Error (*RMSE*) in the overlapping regions of 100 image pairs, before and after the different flat-field corrections. The overlapping regions represent a meaningful test-bed to assess the effectiveness of the vignetting correction. We considered as the best method the one obtaining the lower difference between the overlapping regions (no photometric misalignments should

be present if the stitched images are perfectly corrected). Both *LCBM* and *nLCBM* overcome the other method tested and still *LCBM* was the method achieving the best results, since the main behavior of vignetting is linear. With other additional experiments, we proved that *LCBM* performed better than *nLCBM* mainly in two cases: in images characterized by a large amount of background and in images containing high-intensity values. In the first case *nLCBM* forces to seek non-linearities where probably they are really negligible and this acts as noise enhancement. In the second case, *nLCBM* was not able to reliably correct the high values because in the experiments performed the range of values of the images used to estimate the vignetting functions resulted narrower than the range of the images to be corrected. Accordingly, the highest vignetting function estimated was used as the normalization factor of all the pixels with higher intensity, this yielding errors.

The content of this chapter was partly published in [114].

### 3.7.2 Future work

Both of the methods we proposed can be improved. In particular, the experiment performed computing the *RMSE* in the background regions only showed that *CPboth* provides a better background model than that in *LCBM*. Accordingly, the background modelling of *LCBM* could be improved, even directly using the same model implemented in *CPboth*. Furthermore, we should improve the method to find out how many images are required to obtain accurate vignetting and background surfaces according to *LCBM*. Such analysis could be crucial to provide the microscope users with hints regarding the usability of *LCBM*.

As for *nLCBM*, the algorithm implemented could be optimized to speed up the registration process of the overlapping images acquired, improving the global registration strategy to perform at subpixel accuracy, for instance using the Shi-Tomasi corner points and the Lucas-Kanade features Tracker [100]. In addition, better fitting techniques to obtain the dense vignetting surfaces ought to be devised to achieve more realistic vignetting functions. The experiments with background correction proved that the non-linear correction approach is not a good solution. This is probably due to the main linear nature of the vignetting in the background. Accordingly, to split the flat-field correction into

two different approaches, providing a linear approach for correcting the background values and the non-linear approach only for the foreground, could be the right strategy bringing some improvements. Finally, the trade-off between accuracy of the estimated vignetting functions and the number of overlapping images and the relation between the intensity range of the images to be corrected and the range of the images used to estimate the vignetting functions have to be deepened to provide usability information regarding *nLCBM*.

## 3.8 Acknowledgments

I thank Dr. Gábor Csúcs and his staff of the Light Microscopy and Screening Centre (LMSC) of the ETH Zurich, Switzerland, for providing the data relative to the human genome-wide RNA interference screens used in this work. In particular I thank Dr. Peter Horvath and Dr. Kevin Smith for their suggestions and the hours we spent together to conceive the vignetting correction in fluorescence. Their help was crucial for this work. I also thank the biologists Dr. Justine Kusch and Dr. Andreas Kaufmann that guided us with their knowledge. In particular, their help was fundamental to acquire all the images used in this work.

# Chapter 4

## Mosaicing

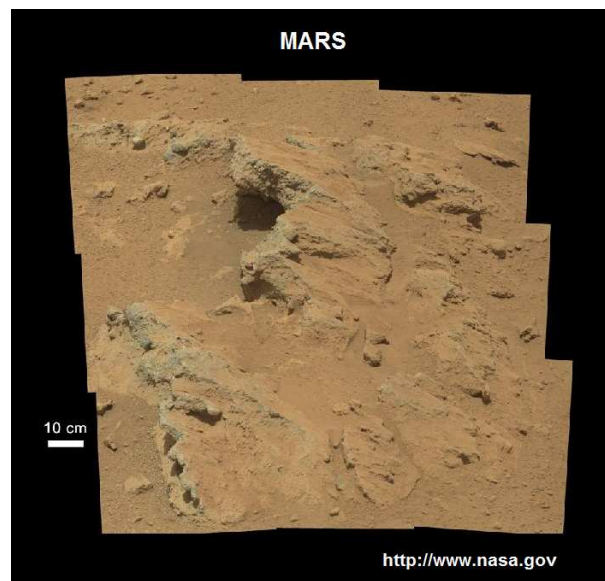


**Fig. 4.1:** Mosaic of satellite images from the soil of Mars.

- L. Carozza, A. Bevilacqua, F. Piccinini, Mosaicing of optical microscope imagery based on visual information. *33<sup>rd</sup> International Conference of the IEEE Engineering in Medicine and Biology Society (EMBS)*, Boston, USA, August 30-September 3, 2011, pp. 6162-6165
- L. Carozza, A. Bevilacqua, F. Piccinini, An incremental method for mosaicing of optical microscope imagery. *8<sup>th</sup> annual IEEE Symposium on Computational Intelligence in Bioinformatics and Computational Biology (CIBCB)*, Paris, France, April 11-15, 2011, pp. 55-60

## 4.1 Introduction

One of the main features of every camera is the Field Of View (*FOV*), meant as the part of the scene shown in a single acquired image. Its finiteness represents a strong limitation for several reasons [115] in different fields like surveillance systems [116], aerospace and satellite monitoring [117] and microscopic specimen analysis [20]. Mathematically, the *FOV* of a digital camera is defined by three parameters: the number of *pixels* of the sensor, the *area* of the pixels and the *magnification* factor used (Eq. 4.1).

$$FOV = \frac{pixels \times area}{magnification^2} \quad (4.1)$$

In particular, area and number of pixels are fixed constraints for each camera, so the *FOV* results inversely proportional to the magnification factor. Accordingly, there is a trade-off between the size of the area represented in an image acquired in a single shot and the magnification factor used. Consequently, acquiring a single image representative of a wide scene with a high pixel's resolution is not feasible.

The *FOV* becomes a strong limitation in several cases. For instance, a narrow *FOV* makes to acquire images of a cell culture at high magnification impossible. Moreover enough cells are needed to have a good statistic [118]. Usually, to overcome this limitation a set of overlapping images is acquired and used to build a mosaic, that is a large image where the original component images are stitched together in a larger one having the same resolution. In this way, it is possible to obtain a single detailed image (the final mosaic) representative of a wide scene [62]. In order to recover the relationships among the different views of the scene proper algorithms are used to find out invariant features then used as references. The main goal is to align (i.e., register) different images of the scene in a common and scene-consistent reference point of view, by estimating the transformations connecting corresponding patterns of the scene matching in the different views. In particular, Image Registration of multiple views constitutes a very complex and challenging research field for the scientific and academic research community [119]. In microscopy, the task becomes even more complex when there is an additional need: to obtain the mosaics in real-time along with the sample observation. This because the operators often need to achieve information on the whole sample directly during the inspection

(often non repeatable), in order to decide how to proceed further.

The number of publications concerning image mosaicing methods is huge. For instance, in 2008 the Annotated Computer Vision Bibliography listed 362 papers only in the *Mosaic Generation* chapter [120]. Nevertheless, mosaicing is still considered an open issue for many applications [121]. [122, 123, 124, 125] present an extensive overview of different registration methods. Furthermore, many open-source and commercial software tools can be employed to obtain image mosaics [126, 127, 128, 120]. To assign the different mosaicing methods to a proper class is not the focus of this work. Despite that, in Sect. 4.2 we try to give a short overview on the main classes.

In this work, we are interested to mosaicing methods for 2D images acquired with widefield microscopes, where the motion between scene and camera is near traslative only, with rotations prevented by the manufacture of the microscopes' holder. Furthermore, the scene objects (typically cells and tissue) can be considered, with a good approximation, as being still and non-deformable throughout the examination time of the specimen. Many methods available in this application field exploit prior information about the registration like the (micrometer) shift between the acquired images, available using automatized acquisition systems like microscopes coupled with motorized  $x$ - $y$  stage. Nevertheless, since the accuracy of the motorized  $x$ - $y$  stage is typically in the order of  $1\mu\text{m}$ , therefore to obtain pixel or sub-pixel alignment's accuracy (dependent of the resolution coefficient, but typically lower of  $1\mu\text{m}$  for high magnifications) proper registration techniques are always required [129, 130]. In addition, the methods are often application-optimized.

Despite many methods have been proposed in the literature, there is no free open source mosaicing method suitable to build mosaics in real-time while images are acquired with non-motorized widefield microscopes. Accordingly, starting from the existing approaches, we implemented our approach in a software capable to work on-line and easy to use for testing different algorithm's combinations and tonal corrections. In particular, in this work we describe such an approach used to build on-line mosaics of microscopic images, that is by reading images from disk but using methods extensible to real-time applications. The method is conceived to work with histological samples and cell cultures (that cover the most relevant part of the routine examinations performed in the biological laboratories) acquired with light microscopes. Nevertheless,

simply adding a correction stage for photo-bleaching, it can be easily extended to general widefield microscopes. The method exploits visual information only and it relies on an efficient image registration method, robust to the presence of outliers and global photometric artefacts, such as those due to the vignetting effect. As a consequence, it does not need automated equipment or prior information, and preserves final photometric and geometric consistency in spite of the manual motion of the microscope holder. The only assumption regards the objects present in the images: they are considered still and non-deformable. Considering the mean time of specimen's observations, the assumption can be realistic even for living cells. The limited computational requirements of our method makes it suitable for a future implementation for real-time applications. As a matter of fact, our approach could be implemented and optimized to build the mosaic interactively during the sample observation, providing the users with an immediate visual feedback on the explored area and "freezing" the sample condition of the precise time of the analysis (sometimes needed but not reproducible). In Sect. 4.3 the detailed presentation of the method is reported, according to the different stages of the general paradigm of the local image registration approaches previously presented. It is worth noting that the main purpose of this work is not necessarily the improvement of the state of the art. Rather, it represents a functional stage for testing the different vignetting correction approaches explained in Chaps. 2 and 3. Nevertheless, we dedicated a specific chapter for this issue, thinking that providing all the details of the mosaicing method would be necessary for the reader to better understand the experimental results. In particular, we implemented an effective solution for creating on-line mosaics by using non-automated microscopes where each parameter regarding warping model, tonal correction and registration strategies can be handled by the user also to provide a numerical assessment of different configurations used in the vignetting correction.

Besides, we validated the proposed mosaicing method by performing several experiments under different working conditions. We used sets of images of histological samples as well as living cell cultures to assess the quality of the mosaics obtained using different warping models and tonal adjustments. The analysis of joint tonal and geometrical registration errors proved that the method can be effectively employed to obtain mosaics on-line.

## 4.2 State of the art

*Image Mosaicing* represents a well studied topic in the Computer Vision research community, and accordingly a high number of works have been published in the last three decades [131].

The mosaicing methods can be firstly classified according to the environmental working domain (outdoor [132], indoor [133]), the applicative field (e.g., Medical/biological [124] such as microscopy [134]), or the dimensionality of objects (3D [135, 120] or 2D [20, 136]). Furthermore, the algorithms employed in these contexts have different hardware requirements and degrees of automation [19, 137, 138]. In general, images to be registered are usually extracted from a video [139, 140, 141] or acquired as sequence of views of the same scene [19, 20, 126]. The overlapping between the different views, object's deformation [142] and illumination changes [143] affect the robustness requirements of the matching stage. Information about the relative motion (traslative, rotative, stationary, etc.) between scene and camera guides the selection of the proper warping model and properties of the scene objects, like motion and presence of deformable objects [144], affect the registration strategy.

In general, the paradigm of image registration almost always works according to following different stages [122, 123]:

- **Feature Detection.** To be able to find the relationship between different views of the same scene, salient image properties have to be detected and matched with repeatability under different conditions. In other words, the chosen feature (or features) must be preserved in presence of geometric transformations, photometric changes, noise, etc. Mainly, two approaches are followed to find salient image properties in different views: a *featureless dense* (also called *area-based*) or a *local sparse* approach. In the first case, image properties of a given region, potentially extended to the entire image, are used. Generally this approach is based on the intensity of all the pixels of the image, without searching for specific features. Instead, the second approach relies on the detection of local features, that are localized patterns with some image's property different from their surrounding neighbourhoods. The properties usually employed to extract (and localize) these patterns fall in the spatial (colour, texture, image gradients and their orientation, etc.), frequency

(e.g., Fourier Transform) or space-frequency domain (e.g., Wavelet coefficients, etc.). Since these methods do not work directly on image intensity but rather on derived invariant properties, they are generally more robust to noise and changes in lighting conditions. The resulting structures can be regions, contour lines or even local patches (e.g. corner points), with different levels of semantic relevance. A wide literature exists that addresses local structures like corners, edges and ... [145].

- **Feature Matching.** In order to derive the transformation matrix relating to the different views of the scene, the patterns detected in the single views have to be related for finding the correspondences. The most important property of a matching method is certainly the robustness, since a sufficient number of correct correspondences must be achieved, avoiding false matchings that could mislead the next image registration stage. Following the main Feature Detection approaches aforementioned, two groups of methods can be outlined for the Feature Matching. The first methods, typical coupled with the *featureless* approach, perform exhaustive search in the whole image domain, using likelihood metrics typically employed for template matching directly on image pixel values. The main drawback of these *correlation methods* is the computational effort required for the exhaustive search of the image patterns to be matched. The second group of methods aim at matching more complex descriptors, generally derived from the sparse detected patterns. These matching methods can be primarily classified into two categories: *geometry-based* and *feature-space*. The geometry-based matching methods employ similarity measurements using geometric properties of the detected features. High-level descriptors, like contours, can be matched using even their local properties (e.g., the curvature). The feature-space matching methods rely on matching of the  $k$ -dimensional feature descriptors as points of  $k$ -dimensional vector space. These vectors generally represent the appearance of localized regions and they are matched according to some defined metric distance. High-dimensional features, being more separable, retain a more discrimination power, but make the matching stage more computationally expensive.
- **Warping Model Estimation.** Once image correspondences are computed, they can be used to infer the warping transformations linking the different views. Generally, hypotheses about the sensor model, the

motion model and the scene structure (rigid, deformable, planar, etc.) are necessary in order to avoid degenerate configurations that can cause ambiguity. The mapping transforms can be *global* (valid in the whole image domain) or *local* (referred to local regions). Here, our applicative domain allows us to focus our attention to rigid transformation for non-deformable objects. The research in this field has been characterized by a great effort towards fully automatic approaches, working for uncalibrated cameras in presence of general scene structures and automatically detecting degenerate configurations for accurately estimating the “correct” scene model using model selection criteria. This goes in the direction of jointly estimating the relative pose parameters between the camera (or cameras) and the scene and/or reconstructing the geometric structure of the scene, preserving scene consistency and accuracy. This is generally achieved by minimizing non-linear cost functions on the global dataset, typically the whole image sequence or a large subset of acquired images. Accordingly, this often requires the application of iterative minimization algorithms on the whole sequence to be known in advance. This typically prevents these methods from running in real-time.

- **Image Warping and Stitching.** The registration of the images in a common reference frame is finally obtained by warping all the single images according to the estimated transformations. Generally, a tonal adjustment is performed in advance in order to preserve in the single views the photometric consistency of the scene taking into account different lighting conditions [146]. Chaps. 2 and 3 of this thesis, dedicated to the vignetting correction, better explain the different approaches mainly used for flat-field correcting the intensity of the single acquired images. Other methods work on histogram matching [147] or blending techniques [90, 21] to attenuate tonal inhomogeneities among the different images to be registered. Once tonal alignment has been performed (except for blending that is a post-processing technique), image warping can be done following different interpolation methods. Seams in the stitching zones are attenuated proportionally to the effectiveness of both the vignetting correction and the geometric registration. It is worth noting that for some Feature Matching methods the vignetting correction can strongly influence the accuracy of the registration. For instance, the area-based methods introduced into the Feature Detection stage of Sect. 4.3.2 are simply based on the intensity values of the image pixels, and in presence

of strong vignetting curvature the difference of the intensities between different regions could produce mismatches. In general, but especially for the area-based methods, to perform the tonal adjustment of the acquired images before the geometric Image Registration is strongly suggested.

According to the above stages, many different combinations have been used to develop different methods reported in the literature, often specific for some application contents.

One of the first solution to build mosaics also in microscopy dates back to 1983 and it presents the multiresolution spline technique originally proposed in [148]. In this multiscale approach, the images to be stitched are distorted and jointed together with smooth seams. The images are decomposed in subimages by filtering/resizing and the same-level subimages, of the original images to be stitched, are separately mosaicked using a weighted average method to avoid seams in the border of the overlapping regions. In practice, each subimage is multiplied by a weighting function which decreases monotonically across its border. The mosaicing method proposed depends on the percentage of image overlapping and on the range of frequencies of the images to be stitched. For this reason, it could be applicable with a high difficulty to the brightfield images of living cells, since they usually are very low contrast images and details lay in a very narrow range of frequencies. No technique is proposed to estimate the shift between the different images to be stitched. Furthermore, the photometric changes are simply attenuated and the vignetting problem is not specifically tackled. Accordingly, despite the high visual quality of the final mosaics, they result not to be suitable for quantitative analyses. More specifically, as far as mosaicing in light microscopy is concerned, most works' purpose has often been to provide visually pleasant mosaics through post processing the whole image sequence.

Since the first solutions to the present days both featureless dense correlation-based methods [149, 150] or sparse feature-based approaches [127, 21] have been widely employed in the registration stage, depending on the computational and accuracy application requirements. A first class of algorithms follow a dense featureless registration approach with likelihood error function based on pixel image intensities and they result computational intensive. The methods proposed in [151] and [152] are conceived to be used necessarily with high-precision motorized  $x$ - $y$  stages. Data obtained with motorized stage con-

trollers [151] and mosaic initialization through manual alignment [152] are used for a coarse geometric registration, while global tonal and geometric alignments are performed by minimizing a cost function over the pixel intensities of the whole image stack. Accordingly, these methods work in batch mode, at the end of the images acquisition stage. A second class of algorithms relies on sparse feature-based registration approaches, detecting and matching salient regions in consecutive images. The algorithm described in [153] utilizes Harris detectors [154] to identify salient points and normalized moment of inertia as their feature descriptor. This method is applied to single couples of images while general issues regarding the mosaic generation (consistency of photometric and geometric registration) are not addressed in by the authors. The method proposed in [21] uses wavelet-based edge correlation to detect feature points and normalized cross correlation for their matching. This method is not conceived for on-line mosaicing since it needs global registration to achieve an accurate mosaic.

Typically, the registration of the different views is done according to either global (e.g., energy minimization [139], global projection [155], graph-based [136]) or local [145] approaches and the performance goes from batch [156] to real-time [157] applications. The warping parameters are estimated, in most of cases, starting with sequential pair-wise registration followed by global registration performed on the whole image sequence or on a large subset [123]. Global registration is generally performed by minimizing non linear cost functions containing many unknowns, depending on the extent of overlapping areas, the number of features, the number of views and the complexity of the motion model. Works in [158, 140, 150] follow this approach, using iterative optimization in a bundle adjustment fashion. Accordingly, the computational burden of the minimization process and, above all, the need of a large set of frames require off-line processing.

As far as mosaicing in microscopy is concerned, most works' purpose has often been to provide visually pleasant mosaics through post processing the whole image sequence, typically using blending techniques [157, 138, 90, 21]. Only few mosaicing methods consider explicitly the vignetting effect [129, 156, 62] and propose interesting solutions [19, 20] for tonally registering the images obtaining visually pleasant mosaics suitable also for quantitative analyses [63, 111, 55, 159].

To conclude, we analyze several freely available mosaicing tools that can be used to obtain mosaics of microscopy images:

- *ImageJ* [95, 160] *Stitching Plugin* [126]. Starting from a set of 2D or 3D overlapping images, the mosaic reconstruction is made pairwise computing subpixel translation among the images. The user can also define an approximate layout of the final mosaic to speed up the registration process. The algorithm is not optimized and it is particularly computational expensive.
- *Autostitch* [127]. In [156] the software tool *Autostitch*, developed for outdoor panoramic image generation, is tested on microscopic image stacks acquired during manual and motorized motion of the microscopes holder. *Autostitch* is based on SIFT [85] detection and matching to increase robustness. It is really user-friendly and widely used. Despite that, it suffers of problems of image merging [133].
- *MosaicJ* [128]. A semiautomated method which requires the user to manually align the images for a subsequent fine registration stage. It is implemented in Java and the software is available as ImageJ plugin. This work being focused on accuracy performance. The images are pixel-wise registered using a dense featureless approach, thus resulting in a high computational burden that prevents this method to be used in real-time.
- *XuvTools* [120]. This is a reliable fully-automated stitching software for 3D datasets of fluorescence images. The toolset is written in templated C++. Before a fine registration, the whole set of images is automatic analyzed to define an approximate layout of the final mosaic and this requires a high computational effort. Then a Seams in the stitching zones are attenuated by a bleaching correction at the borders. The main limitation is the assumption regarding translations only between the images.

It is worth noting that all the above mentioned mosaicing tools work off-line and provide blending techniques to reduce intensity inhomogeneities between the images stitched, but none of them takes the vignetting effect explicitly into consideration.

## 4.3 Methods

In this section, we describe our approach for building on-line mosaics of microscopic images. As stated above, the method is developed for images of histological specimens and cell cultures acquired with light microscopes, but it can be easily extended to widefield microscopy. The method starts analyzing (on-line or off-line) pairs of acquired overlapping images. It exploits visual information only and it relies on an efficient image registration method based on matching of corner points, that are robust to the presence of outliers and photometric artefacts, such as the vignetting effect. As a consequence, it does not need automated equipment or prior information, and preserves photometric and geometric consistency during the manual motion of the microscope holder. The only assumption regards the properties of the objects present in the images: they are considered not in motion and non-deformable. In the next Sects., we describe the proposed mosaicing approach following the different stages of the general paradigm of image registration presented in Sect. 4.1.

### 4.3.1 Pre-processing

Before going inside the detail of the geometric registration, we focus our attention on the tonal alignment of the acquired images. As the first step, every acquired image is flat-field corrected to obtain a set of consistent views of the same scene, without non-uniformity of the signal distribution inside the single images. Generically, the Köhler illumination [24] is only theoretical and all the acquired images are characterized by an uneven distribution of the “illumination” signal (evident as intensity’s curvature), usually known as vignetting effect (Fig. 4.2). If the images are stitched together without performing an appropriate correction, seams in the stitching zones of the final mosaic would be evident (Fig. 4.3a). Many methods have been proposed in the literature to correct the vignetting effect (see Chap. 2). The most trivial and commonly used approach in light microscopy is to acquire in advance an image or a sequence of images of an empty field and using the surface obtained as the vignetting function to normalize the intensity of every subsequent acquired image [109]. The standard flat-field correction formula already introduced in Sect. 2.3 is

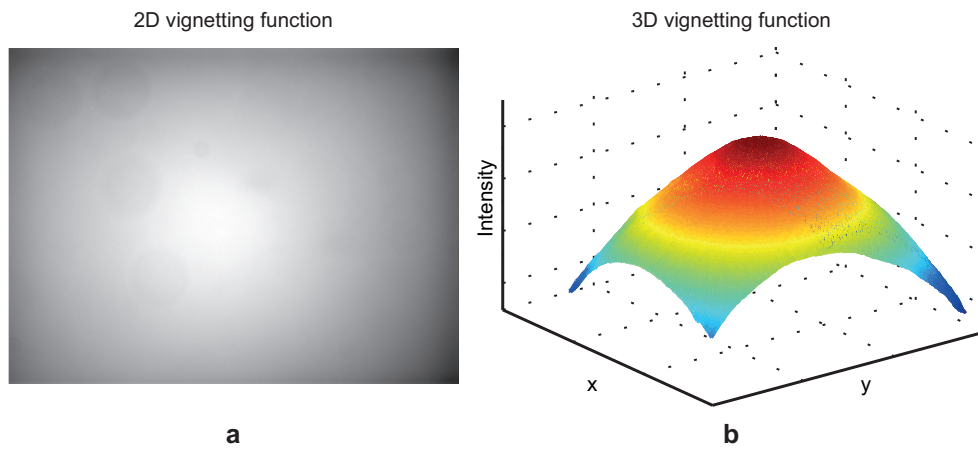


**Fig. 4.2:** Curvature of the image's intensity. The vignetting effect causes a curvature on the intensity of the acquired images. (a): schematic 2D and (b): 3D representation of the intensity curvature of the median surface of a stack of images acquired in brightfield from an empty field is proposed.

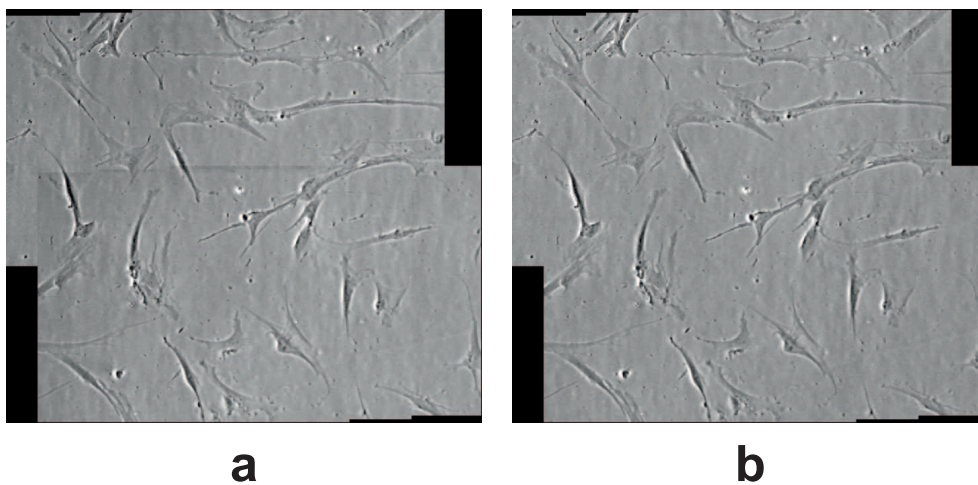


**Fig. 4.3:** Visual comparison between mosaics built with and without vignetting correction. (a): mosaic of 6 images of living mesenchymal SC, acquired using in phase contrast microscopy. If no vignetting correction is performed, seams in the stitching zones are pretty evident and they can mislead segmentation or automatic analysis. (b): the same mosaic corrected using the vignetting function estimated from empty field. Seams are almost negligible.

here reported for completeness (Eq. 4.2):

$$I_{FFC} = \frac{I}{V} \bar{V} \quad (4.2)$$

$I$  is the original acquired image,  $V$  is the vignetting function,  $\bar{V}$  is the mean value of  $V$ ,  $I_{FFC}$  is the final flat-field corrected image. After the correction, the seams in the stitching zones result strongly attenuated (Fig. 4.3b). In our approach, the acquired images are first converted in grey levels (in case they are multichannel) and then are flat-field corrected, just before the geometrical registration stage. It is worth notice that our method can be employed also to work with colour images, which are flat-field corrected by normalizing all the channels with the same vignetting function. However, further strategies have to be adopted to avoid problems such as the generation of pseudo colours [157, 33, 90, 161, 162, 163, 72].

### 4.3.2 Feature Detection

We developed our method to work on-line with the image acquisition, also for planning an extension for real-time applications in the future. Accordingly, to use local-sparse features that do not require high computational time to be extracted and matched [164]. In particular, we employed the Shi-Tomasi features (corner points characterized by a high intensity gradient) [100], robust and easy to track also in presence of geometric transformations, photometric changes, noise, etc (Fig. 4.4). In particular, Shi and Tomasi proposed a stable corner detector analyzing the condition number of the pseudo-Hessian matrix (also named auto-correlation matrix) performed on image patch  $G(\cdot)$  of sizes  $W$ , centered on points  $(x, y)$  of the reference image, being  $I^x$ ,  $I^y$  the local components of image gradient (Eq. 4.3):

$$G(x, y) = \begin{bmatrix} \sum_{i \in W} (I^x(x_i, y_i))^2 & \sum_{i \in W} (I^x(x_i, y_i)I^y(x_i, y_i)) \\ \sum_{i \in W} (I^x(x_i, y_i)I^y(x_i, y_i)) & \sum_{i \in W} (I^y(x_i, y_i))^2 \end{bmatrix} \quad (4.3)$$

The image patch can be characterized according to the eigenvalues  $\lambda_1$  and  $\lambda_2$  of  $G(\cdot)$  as:

- a flat region, if both  $\lambda_1$  and  $\lambda_2$  are small in value;
- an edge, if one eigenvalue is high in value, showing image variability in that specific direction;

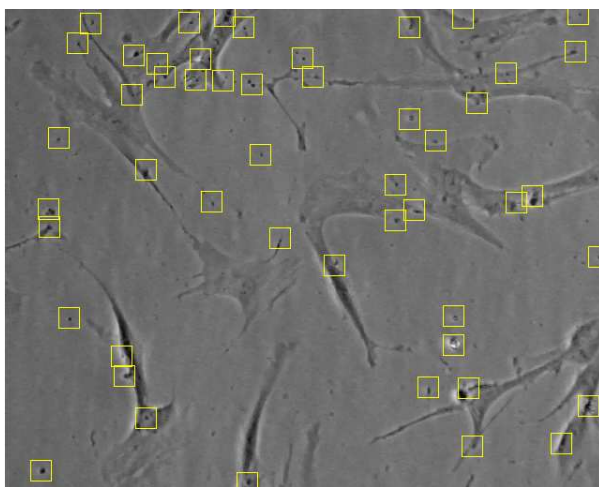


**Fig. 4.4:** Shi-Tomasi features. Shi and Tomasi proposed a stable detector for corner points easy to track and robust also in presence of some geometric transformations, photometric changes, noise, etc. The corner points are based on the highest eigenvalues of the image.

- a corner, if both  $\lambda_1$  and  $\lambda_2$  are high in value.

The  $G$  matrix is well conditioned if the eigenvalues do not differ too much. At the same time, the eigenvalues must be greater than a certain threshold  $\lambda_{min}$  in order to be reliable and not capture noise (Eq. 4.4):

$$\min(\lambda_1, \lambda_2) > \lambda_{min} \quad (4.4)$$

Practically speaking, the minimum eigenvalue is computed for each of the reference image pixels, yielding an eigenvalue map. Non-maxima suppression is performed on this map on a local pixel's neighbourhood, and the remaining samples are thresholded by a strength value  $\lambda_{min}$ . Finally, the corners are chosen spatially spread, rejecting on the map those locations spatially close to stronger corners.

In our approach two subsequent acquired images are always supposed to overlap. This is generally true if the images are extracted from videos or if the mosaic is built in real-time with the image acquisition. In particular, between each pair of subsequent images there must be a minimum of 10% of overlapping. In our approach, to perform the registration between each current image

and the previous one, first the Shi-Tomasi corner points are detected separately in both the images, then the correspondences among the corner points extracted in the two views are estimated.

### 4.3.3 Feature Matching

According to previous stage, to estimate the correspondences of the features detected in the subsequent views we employed the Lucas-Kanade Tracker (LKT) for two main reasons. First, it is the best one to define the correspondences using the Shi-Tomasi corner points. Second, it works with subpixel accuracy with excellent time performance (Fig. 4.5). The LKT is based on the early work of

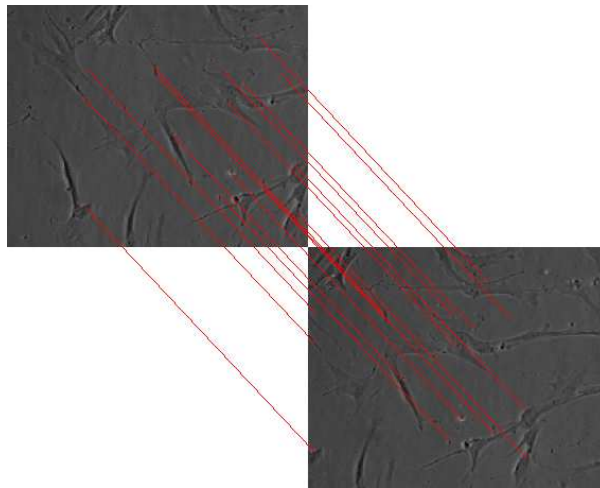


**Fig. 4.5:** Correspondence between corner points using LKT. Used to estimate the correspondences between features detected in the different views. It is the best one to define the correspondences using the Shi-Tomasi corner points and it works with subpixel accuracy with good time performance.

Lucas and Kanade [101], then fully developed by Tomasi and Kanade [165] and clearly explained by Shi and Tomasi in [100]. Practically speaking, this widely used tracker aims at estimating local optical flow displacements using a linear approximation of spatial and temporal variations of the image intensity. In the last two decades, LKT has been used in very different applicative domains, such as robotics, face recognition, vehicle tracking [166]. Its main advantages are the efficacy, even without the claim of generality, and its computational

simplicity, which makes the method suitable even for hardware implementations on old generation devices. In brief, given a local image patch centred on the pixel  $(x, y)$ , let us suppose that the optical flow constraint equation is fulfilled between two acquisition instants  $(t, t + \delta t)$  (Eq. 4.5):

$$I(x, y, t) = I(x + \delta x, y + \delta y, t + \delta t) \quad (4.5)$$

Then, for small motion offsets the local unknown displacement vector  $\bar{v} = (v_x, v_y)$  (assumed locally constant for that image patch) among the image pair  $(I, J)$  can be found by minimizing the likelihood Sum Squared Difference (SSD) score (Eq. 4.6):

$$\epsilon(v) = \sum_W (I(x, y) - J(x + v_x, y + v_y))^2 \quad (4.6)$$

in a neighbourhood  $W$  of the feature location. Accordingly, the optimum  $\bar{v}_{opt}$  is found for the vector  $\bar{v}$  satisfying Eq. 4.7:

$$\left. \frac{\partial \epsilon(\bar{v})}{\partial \bar{v}} \right|_{\bar{v}} = [0 \ 0] \quad (4.7)$$

Expanding Eq. 4.7 according to its Taylor series approximation for small displacements, after some passages Eq. 4.8 is found for  $\bar{v}_{opt}$ :

$$\bar{v}_{opt} = G^{-1} \cdot \bar{b} \quad (4.8)$$

being  $G$  the auto-correlation matrix in Eq. 4.3 and  $\bar{b}$  a term containing spatial and temporal (that is between the images under registration) derivatives (see [167]). The Shi-Tomasi feature detector ensures that the problem expressed by Eq. 4.8 is well conditioned. The LKT method estimates the vector  $\bar{v}$  and uses it iteratively for a subsequent small signal linearization, until the algorithm converges or a maximum number of iterations is reached. This algorithm can reach subpixel accuracy but cannot handle robustly too large image displacements. Pyramidal implementation of this algorithm [167] aims at coping with this issue, working on more pyramidal levels on which estimating “small” displacement vectors, then back propagated to higher pyramid levels up to the original image. However, this approach can lead even to false matchings when “similar” interest points are spread along the image. For this reason, we used the global area-based method named Phase Correlation (all the details in Appendix 6) as a bootstrap step for providing a guess value for the tracker initialization [168].

### 4.3.4 Warping Model Estimation

The warping transformation between two images can be estimated starting from point correspondences between the two views. In general, the warping transformation depends on the geometrical configuration linking camera motion and scene, and no assumption about the model can be made if no priors about camera motion and scene structure are given. In this section some basis knowledge about the *two-view* geometry [119] are briefly recalled, since generally pair-wise (sequential) registration approaches are required for on-line applications. Fundamental concepts of homography estimation and epipolar geometry are addressed for completeness.

Epipolar Geometry constitutes the general approach to projective geometry between two views. The fundamental epipolar equation is reported in Eq. 4.9:

$$I1_i \cdot F \cdot I0_i = 0 \quad (4.9)$$

which represents a necessary condition once two sets  $I0_i$  and  $I1_i$  of  $i = 1, \dots, C$  corresponding image points, are established between the two views ( $I0, I1$ ). The Fundamental matrix  $F$  is independent from scene structure and retains the camera's relative pose. Accordingly, it can be estimated from image correspondences. Estimation of the  $F$  is subject to ambiguity when degenerate configurations are encountered. Structural degeneracy is met when the structure of the scene is planar, while pose degeneracy is encountered when the two camera centres almost coincide, as for small baselines or pure camera rotations. In these two cases the epipolar geometry can be simplified to planar projective geometry. According to the theory of planar registration, for pure camera rotations (independently from the scene structure) and planar regions (independently from the camera pose) - an approximation that holds also for scenes distant from the camera - image correspondences are linked through the projective homography matrix  $H_{I0}^{I1}$  according to the homogeneous Eq. 4.10:

$$I1_i = H_{I0}^{I1} \cdot I0_i = \begin{bmatrix} h_{11} & h_{12} & h_{13} \\ h_{21} & h_{22} & h_{23} \\ h_{31} & h_{32} & h_{33} \end{bmatrix} \cdot I_i \quad (4.10)$$

where the parameter  $h_{33}$  is typically forced to the value 1 to avoid of representing equivalent transformations given by matrices multiple of others. Ac-

Accordingly, homography has only 8 degrees of freedom. Furthermore, homographies are endowed with a group structure so that their composition is still a homography. With these hypotheses, given at least 4 non collinear point correspondences, the entries vector  $\bar{h}$  of the homography parameters can be estimated according to the Direct Linear Transform (DLT) method. DLT aims at estimating the homography parameters rearranging Eq. 4.10 so that a linear system in 8 unknowns can be written (Eq. 4.11):

$$A \cdot \bar{h} = 0 \quad (4.11)$$

where the entries of the matrix  $A$  are function of the image correspondence coordinates (see [119] for details). The vector  $\bar{h}$  is estimated solving typically in a least square sense the (usually overdetermined) constrained problem (Eq. 4.12):

$$\min \|A \cdot \bar{h}\| = 0, \|\bar{h}\| = 1 \quad (4.12)$$

The considerations regarding the model estimation are valid assuming that correspondences are affected only by measurement errors, that is related to image features really corresponding to the same point in the scene matched with a limited accuracy. However, the matching algorithms can also return false matchings that alter this distribution and can dramatically affect the model estimation stage. Outliers can be due to the registration algorithm, as it happens when (false) matchings are established between points related to different parts of the scene, or to the presence of migrating impurities corpuscles and slight modifications of not stable structures. Furthermore, the holder guide could not be planar and the depth of focus would not be spatially uniform, so that corresponding points in different views can present out-of-focus blurring effects. Accordingly, robust model estimation requires the image correspondences to be filtered, so that outliers are removed and the model computed on a robust support only [169]. To this purpose, the RANSAC algorithm [170] has been widely employed in the Computer Vision literature (details in Appendix 6).

The acquisition conditions, the scene model and the camera model should be taken into account for the selection of the warping model. The system can be modelled as composed of a fixed (projective) camera which observes the manual rigid movement of the microscope holder. The thickness of the specimen (some microns) being negligible with respect to the lens working distance (some centimeters), the scene can be considered planar. Under these

conditions, the parallax effect can be neglected and corresponding features  $(I0_i, I1_i)$  on two consecutive views  $(I0, I1)$  are related by a projective planar homography  $P_{I0}^{I1}$  according to the homogeneous Eq. 4.10, here recalled for completeness (Eq. 4.13):

$$I1_i = P_{I0}^{I1} \cdot I0_i = \begin{bmatrix} p_{11} & p_{12} & p_{13} \\ p_{21} & p_{22} & p_{23} \\ p_{31} & p_{32} & 1 \end{bmatrix} \cdot I0_i \quad (4.13)$$

with  $\|\bar{p}\|=1$ . Thus, proceeding by a set of at least 4 non collinear feature matchings in the system of Eq. 4.13, the estimation of this 8-parameter transform would be required in general. In our case study, two additional approximations can be considered as satisfied. First, the depth-extension of the scene (the biological sample) is small if compared with the average distance from the sample and the camera principal point. Second, the imaged points of the scene can be considered close to the optical axis due to the “small” field of view of the camera. Under these hypotheses, the perspective camera model can be relaxed to the *affine* model  $A_{I0}^{I1}$  expressed by Eq. 4.14:

$$I1_i = A_{I0}^{I1} \cdot I0_i = \begin{bmatrix} a_{11} & a_{12} & a_{13} \\ a_{21} & a_{22} & a_{23} \\ 0 & 0 & 1 \end{bmatrix} \cdot I0_i \quad (4.14)$$

and the parameters to be estimated decrease to 6. Moreover, by proceeding with this complexity reduction approach, we can suppose to neglect the mechanical play of the holder (that can be affected by drift effects due to its continuous use) and the relative deviation of the camera optical axis from the normal to the holder. This yield to conceive a *translative* model  $T_{I0}^{I1}$ , shrinking the number of parameters to be estimated to 2, that are the  $x$  and  $y$  translation components (Eq. 4.15):

$$I1_i = T_{I0}^{I1} \cdot I0_i = \begin{bmatrix} 1 & 0 & \Delta x \\ 0 & 1 & \Delta y \\ 0 & 0 & 1 \end{bmatrix} \cdot I0_i \quad (4.15)$$

In Table 4.1 the main features of these global transformation models (Fig. 4.6) are summarized. The estimation of these models is carried out by solving their (typically overdetermined) system, according to Eq. 4.11. It is worth remarking that the estimation procedure of the warping transform is quite

Model	k	$C_{min}$	H
Projective	8	4	$P = \begin{bmatrix} p_{11} & p_{12} & p_{13} \\ p_{21} & p_{22} & p_{23} \\ p_{31} & p_{32} & 1 \end{bmatrix}, \ \bar{p}\ =1$
Affine	6	3	$A = \begin{bmatrix} a_{11} & a_{12} & a_{13} \\ a_{21} & a_{22} & a_{23} \\ 0 & 0 & 1 \end{bmatrix}$
Translative	2	1	$T = \begin{bmatrix} 1 & 0 & \Delta x \\ 0 & 1 & \Delta y \\ 0 & 0 & 1 \end{bmatrix}$

**Tab. 4.1:** Properties of the warping models employed in this context.  $k$  is the number of parameters (degrees of freedom) of the model,  $C_{min}$  is the minimum number of correspondences needed to estimate the model.



**Fig. 4.6:** Global transformation models. From left to right: original image, rigid, affine and projective transformation's representation.

sensitive to the presence of outliers (false matchings) and to the percentage of the overlapping area between two consecutive frames.

### 4.3.5 Image Warping and Stitching

Once the pair-wise matrix  $H_{I_1}^{I_0}$  relative to the global predesigned transformation model has been estimated, it is used to perform the final warping of the image  $I_1$  in the domain of the image  $I_0$ . Using a concatenation of matrices, every image can be warped in the domain of a reference image. In particular, we have chosen as mosaic reference frame the first image acquired ( $I_0$ ). Accordingly, the mosaic warping matrix for the  $n^{th}$  frame,  $H_{I_n}^{I_0}$ , defined by the relation (Eq. 4.16):

$$I_0 = H_{I_n}^{I_0} \cdot I_n \quad (4.16)$$

can be obtained by incrementally chaining, through the matrix right-productory operator (Eq. 4.17):

$$H_{I_n}^{I_0} = \prod_{i=1}^n H_{I_n}^{I^{(i-1)}} = H_{I_1}^{I_0} \cdot \dots \cdot H_{I_n}^{I^{(n-1)}} \quad (4.17)$$

This “*Frame-to-Frame*” (F2F, [99]) incremental approach is prone to *dead reckoning effects*, due to the accumulation of the estimation errors, that can turn to increase geometric deformations and misalignments. This effect is more evident for long looping path sequences, where frames of revisited areas of the scene can present a visible misalignment with the frames already mapped into the mosaic. As discussed above, generally a *global* registration of the collected frame is required to compensate for these effects. However, this would require to know all the image sequence in advance and would result in a computational intensive optimization stage. Alternatively, a “*Frame-to-Mosaic*” (F2M) approach [171, 132, 172] can be used, this permitting to reach a good trade off between the accuracy of the resulting mosaic and computational performances. According to this approach, the current  $n^{th}$  frame is registered not only with the previous  $(n - 1)^{th}$  frame, but also with the mosaic built up to that point. Let the F2M matrix between  $I_n$  and  $I_0$  be  $M_{I_n}^{I_0}$ . The corrective contribution is estimated by registering  $B_n$ , the warp version of  $I_n$  defined according to Eq. 4.18:

$$B_n = M_{I_{(n-1)}}^{I_0} \cdot H_{I_n}^{I^{(n-1)}} \cdot I_n \quad (4.18)$$

with the corresponding area  $C_n$  of the mosaic built by stitching the image  $I_{(n-1)}$  as the last one, according to the F2F registration. Being  $H_{B_n}^{C_n}$  the F2F matrix taking into account this corrective term,  $M_{I_n}^{I_0}$  becomes (Eq. 4.19):

$$M_{I_n}^{I_0} = \prod_{i=1}^n H_{I_i}^{I^{(i-1)}} \cdot H_{B_i}^{C_i} = H_{I_1}^{I_0} \cdot H_{B_1}^{C_1} \cdot \dots \cdot H_{I_n}^{I^{(n-1)}} \cdot H_{B_n}^{C_n} \quad (4.19)$$

Accordingly, in the F2M approach  $I_n$  is warped in the domain of  $I_0$  according to Eq. 4.20:

$$I_0 = M_{I_n}^{I_0} \cdot I_n \quad (4.20)$$

This further registration has the advantage of compensating mis-registrations at a reduced computational cost, since it requires only one more LKT stage, fed by the estimated model resulting from the F2F registration. Accordingly, the

application of the Phase Correlation stage, more computationally expensive, is not needed at this point.

Once the final mosaic warping matrix has been computed, the  $n^{\text{th}}$  image is then warped into the mosaic reference frame, using bilinear interpolation, and merged into the mosaic using a *stitching* approach, that is replacing the underlying pixel values. Typically, *blending* approaches are used to remove seams in the stitching zones [90, 21]. Nevertheless, if particles in adjacent frames are in motion, using blending they are shown as blurring objects in the final image. In the literature, this problem is known as *ghosting* effect [157, 138, 173]. In order to avoid it, we chose to employ the stitching approach mentioned above instead blending. Moreover, in microscopy image mosaics the seams are mostly due to vignetting and shading effects. Our flat-field correction stage compensates for these artefacts, this permitting to create a visually pleasant mosaic while keeping the high geometric accuracy achieved by our registration method.

## 4.4 Materials

In order to assess the quality of the proposed mosaicing approach, image sequences of biological samples have been acquired using standard non-motorized widefield microscopes widely employed in research labs. In particular, we have utilized an inverted Nikon Eclipse TE2000-U microscope equipped with a Nikon DXM1200 digital camera able to perform live acquisition at  $640 \times 512$  pixel resolution, 8-bit gray levels intensity. The system has been connected to an off-the-shelf PC (Intel Core i5, CPU 2.27GHz, 4GB RAM). Fig. 4.7 summarizes the framework used in our experiments. During our experiments, a magnification factor of  $100\times$  has been applied (lens used  $10\times$ , magnification of the camera  $10\times$ ), this resulting in a spatial resolution of  $1.0152\mu\text{m}/\text{pix}$ . All the images have been acquired in phase contrast mode.

Typically, the most trivial but common approach for correcting the inhomogeneous light signal in a single image is acquiring in advance an empty field image and using its intensity curvature as normalization factor. Accordingly, before positioning the specimen on the holder, empty field images have been acquired for several seconds (yielding a stack of 60 elements) in order to es-



Nikon Eclipse  
TE-2000U

DXM1200 Digital  
Eclipse Hardware

PC

**Fig. 4.7:** The system used in our experiments. The inverted microscope Nikon Eclipse TE2000-U has been equipped with a Nikon DXM1200 digital camera. The system has been connected to an off-the-shelf PC.

timate the vignetting function, meant as the median surface of the stack of images. Then, during the acquisition of the sample's images, the holder has been moved manually to mimic a real specimen inspection.

To assess the performance of our algorithm in different working conditions we acquired two different sets of overlapping images. The first set consists of images of living mesenchymal Stem Cells (SC) characterized by very low contrast and low confluency (Fig. 4.8). The second set refers to a histological sample of an altered Bone Tissue (BT), characterized by the presence of background regions among connected structures (Fig. 4.9). The cells were contained in commercial plastic six-well plates and the bone tissue was placed on glass slides with mounting medium. The confluence of the MSC images used in the experiments is about 30%. From both sets, we chose a subset of images to build a looping path with an overlap between the first and the last image aligned into the mosaics. The percentage of overlap between every pair of subsequent selected images always ranged between 15-85%. In particular, to build the mosaics we used subsets of 30 SC and 40 BT images (named SC30 and BT40, hereinafter) (Figs. 4.10 4.11).

The mosaics have been built off-line for testing the performance of different setups of the algorithm's parameters. In particular, we compared the mosaics obtained:

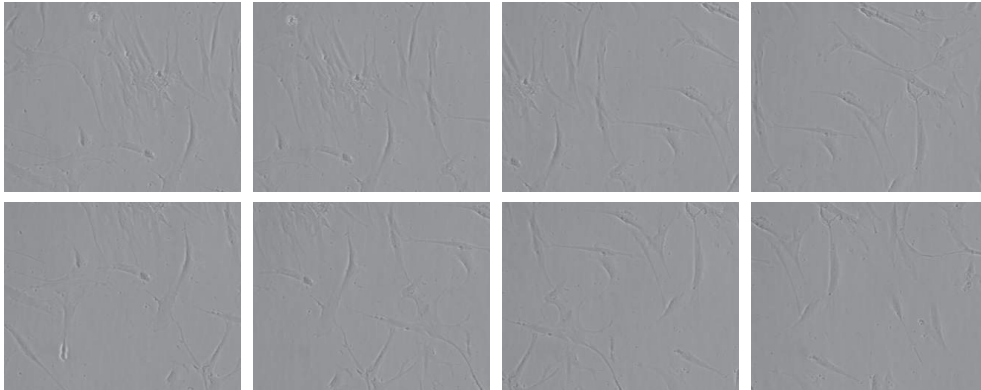


**Fig. 4.8:** Eight images ( $640 \times 512$ , 8-bit gray levels) of living mesenchymal stem cells used in the experiments. They are characterized by very low contrast.

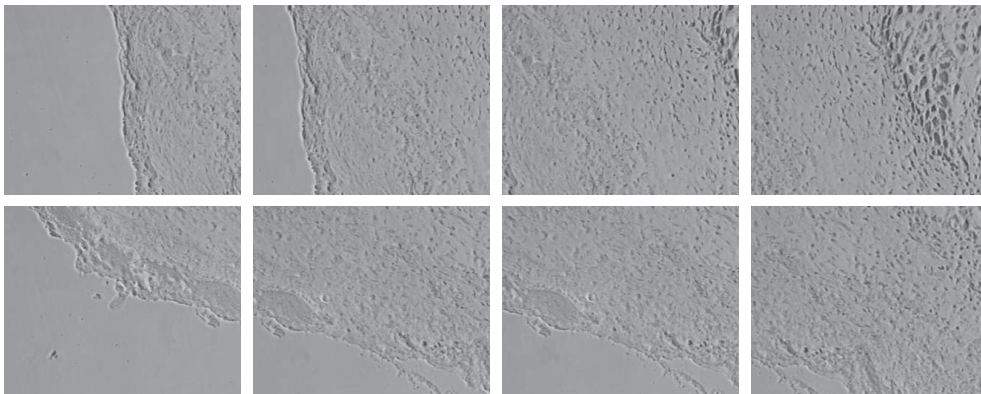


**Fig. 4.9:** Eight images ( $640 \times 512$ , 8-bit gray levels) of fixed bone tissue. The background regions are constitute by empty glass free of tissue.

- with and without the tonal alignment (performing or not the flat-field correction of the input images using the vignetting function estimated from the empty field)
- using the F2F or the F2M geometric registration approach
- according to the translative or affine or projective transformation model

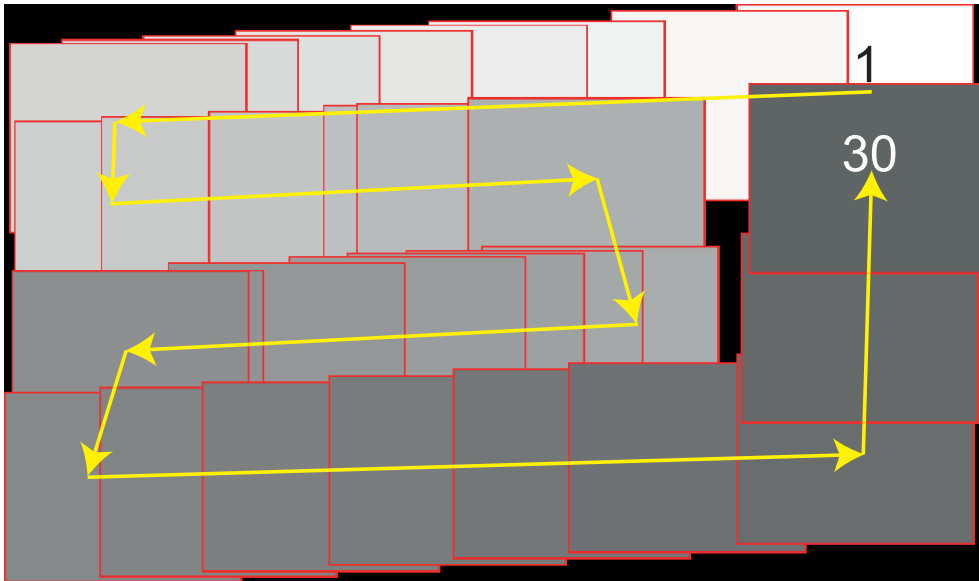


**Fig. 4.10:** Mosaic building path of the selected 30 images regarding mesenchymal SC. The direction of the alignment is pointed out with yellow arrows. There is an overlap between the first (represented as the brightest one) and the last (the darkest one) image aligned (looping path).

## 4.5 Metrics

Due to the lack of the mosaic ground truth [174], it is not so trivial to assess which is the best parameter combination to build mosaics using a general widefield microscope. Furthermore, the best parameters combination depends on the context, meant as foreground confluency, percentage of overlapping between two consecutive images, size of the final mosaic, number and path of the aligned images. According to the translative motion of the widefield microscope's holder, the translative warping model should be a good choice, but angular drift could make the affine or even the projective model a better choice. To numerically compare the different mosaics obtained according to different parameter combinations, we proposed two different types of evaluation. The first evaluation takes in consideration the joint tonal and geometric registration error, meant as a value combination of the effects of both tonal and geometrical registration error [175].

Here, we recall that we adopted a stitching strategy where each image is over-

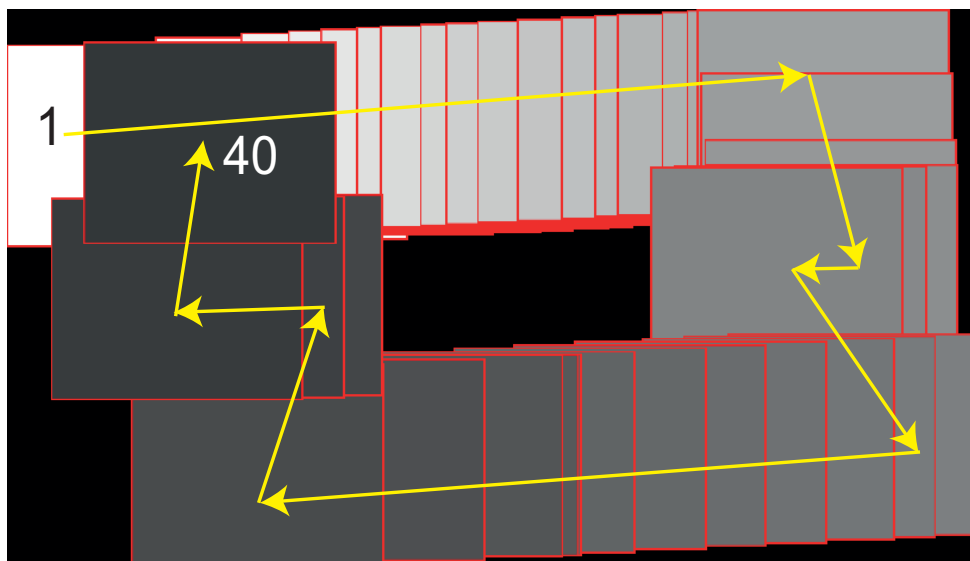


**Fig. 4.11:** Mosaic building path of the selected 40 images of an histological sample of BT. The direction of the alignment is pointed out with yellow arrows. There is an overlap between the first (represented as the brightest one) and the last (the darkest one) image aligned (looping path).

written by the overlapping subsequent ones. In particular, we computed the Root Mean Squared Error ( $RMSE$ , Eq. 4.21, [103]) between the Back Projection ( $BP$ ) of each original image ( $I$ ) registered into the mosaic, and its part overlapped by the mosaic itself (Overlapped Part -  $OP$ ).

$$RMSE_n = \sqrt{\frac{\sum_x \sum_y [OP_n(x, y) - BP_n(x, y)]^2}{P}} \quad (4.21)$$

$n = 1, \dots, N - 1$ , with  $N$  the number of images registered into the mosaic. In Eq. 4.21 we just consider the pixels  $(x, y)$  of the  $OP$  that are really overwritten. Practically speaking,  $P$  is the number of pixels of  $OP_n$  that were overwritten by  $I_i$  with  $i > n$ . Logically,  $RMSE_n$  evaluated between  $BP_n$  and  $OP_n$  pixels where  $I_n$  contributes would be always 0. In particular, the  $RMSE$  has been evaluated for  $N - 1$  pairs  $BP_n$  and  $OP_n$ . Of course, no images overwrite the mosaic's parts where the last image  $I_N$  is aligned. Computing the  $N - 1$   $RMSE$ s contributes to obtain a good statistic, because it is like comparing  $N - 1$  different mosaics, even if these are not fully uncorrelated due to the dead reckoning effect. Fig. 4.12 provides a visual schematic representation

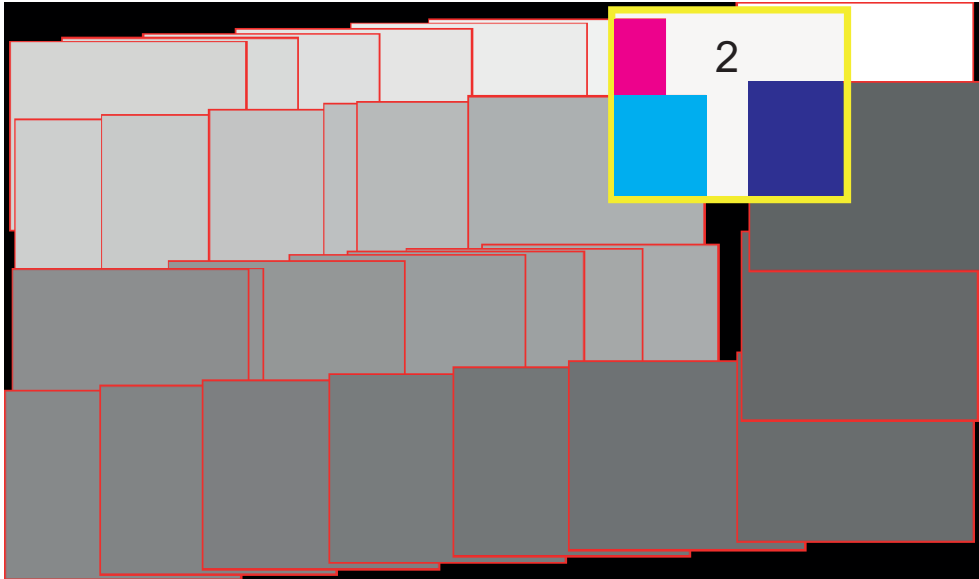


**Fig. 4.12:** Representation of the displacement of images composing the mosaic evaluated. The position of every image aligned is coloured using a different grey intensity. The borders of the aligned images are reported in red. To compute the  $RMSE_2$ , the image  $I_2$  (its border is highlighted in yellow) is back-projected into the mosaic and only the areas coloured in light magenta, cyan and blue are used to compute the error value.

of the image displacements to understand better how the  $RMSE_n$  has been evaluated for each image  $I_n$  registered into the mosaic.

The second type of evaluation aims to perform a quantitative comparison between the different mosaics, considering the geometrical registration error only. To this purpose, in all the mosaics, the first image was considered two times, at the beginning and at the end, also being the last image aligned through a simple F2F registration. To obtain a measure of the geometric registration error, we computed the Normalized Euclidean Norm ( $NEN$ ) of every global warping registration matrix obtained (Global Matrix -  $GM$ ), after subtracting the Identity Matrix ( $IM$ ) as normalization factor (Eq. 4.22).

$$NEN = \sqrt{\sum_{e=1}^E (GM(e) - IM(e))^2} \quad (4.22)$$

$E$  is the number of elements of the matrices  $GM$  and  $IM$ . For the transla-

tive, affine and projective models  $E = 9$ . Theoretically, in presence of no registration errors  $NEN = 0$ . Accordingly, the model yielding the final best geometrical registration is that obtaining the lower  $NEN_N^2$ .

## 4.6 Experimental results

The experiments aim at assessing the quality of the proposed mosaicing approach according to the different algorithm's configurations. In particular, we carried out experiments to verify the improvements in the mosaics built according to the tonal and the F2M registration. To this purpose, the *RMSE* values have been computed using different mosaics built with the same sets of images but changing the algorithm's configuration: whether the flat-field correction is performed or not and the geometric registration is F2F or the F2M. Finally, to decree which warping model is the better choice, we compared the mosaics built with the same sets of images, but alternatively using the translative, the affine or the projective warping model. In particular, we compared the different warping models, closing the path by registering as last image the first image of the mosaics and we used  $NEN$  as a quantitative metric. In the next subsections we first show the results obtained using the set of images named SC30, then those pertaining the set BT40.

### 4.6.1 Flat-field correction

The 30 images of the set SC30 have been registered accordingly to all the possible arrangements of tonal alignment, geometric registration and warping model. Mean ( $\mu$ ) and standard deviation (std,  $\sigma$ ) of the *RMSE* values computed using the first 29 images are reported in Tab. 4.2. For each combination of warping model and geometric registration, the mosaic obtained performing the flat-field correction achieved on average always lower (hence, better) *RMSE* than the corresponding mosaic obtained without performing the flat-field correction (rows 1 and 2 of Tab. 4.2 versus rows 3 and 4, respectively). In other words, the  $\mu$  values are typically lower when the flat-field correction is performed. This because the more the images are flat, the more the intensity difference in the images overlapping is lower in average. As far as the  $\sigma$

<i>RMSE</i> values ( $\mu \pm \sigma$ )			
Algorithm's configuration	Model		
	Translative	Affine	Projective
1: F2M with flat-field correction	2.67±0.98	2.05±0.20	2.02±0.16
2: F2F with flat-field correction	3.49±1.34	2.13±0.25	2.12±0.28
3: F2M without flat-field correction	4.43±0.85	4.31±1.23	4.30±1.19
4: F2F without flat-field correction	4.96±1.31	4.18±0.76	4.29±0.95

**Tab. 4.2:** *RMSE* values using SC30. Mean and standard deviation of the *RMSE* values computed using the images of the set SC30.

is concerned, for affine and projective models one can see that flat-field correcting lowers its value by a factor of three times, yielding a better stability to better *RMSE* values. An exception can be seen for the translative model where, in spite of a clear improvement of *RMSE*,  $\sigma$  slightly worsens, pointing out a better stability in the worst results. As expected, this proves that the flat-field correction always improves the mosaic. Figs. 4.13 and 4.14 report the

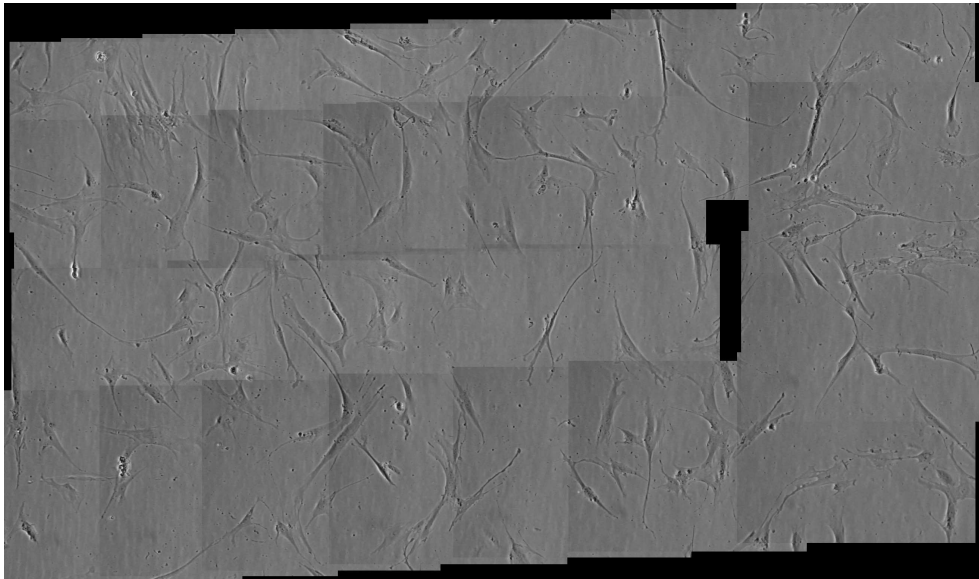


**Fig. 4.13:** Mosaic SC30 without flat-field correction. The mosaic has been obtained by aligning the images of the set SC30 according to the translative model, F2F registration, no flat-field correction.

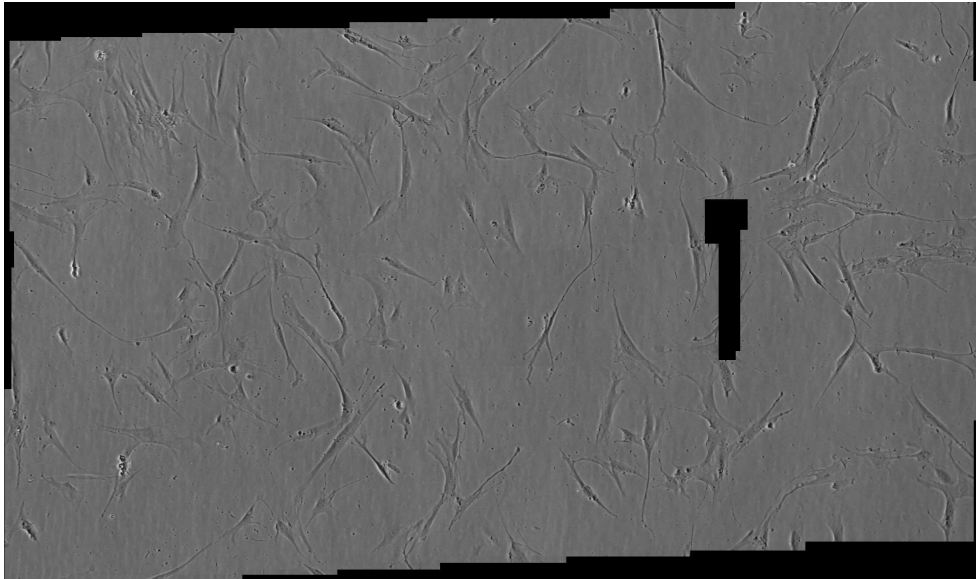


**Fig. 4.14:** Mosaic SC30 with flat-field correction. The mosaic has been obtained by aligning the images of the set SC30 according to the translative warping model, F2F registration, flat-field correction.

mosaics achieved with translative warping and F2F registration. The mosaic in Fig. 4.14 is obtained by flat-field correcting the input images. Seams in the stitching zones are strongly attenuated and the improvement is visually evident.

### 4.6.2 F2M registration

Tab. 4.2 shows that for each combination of warping model and geometric registration, the mosaics obtained with the flat-field correction achieve on average always a lower *RMSE*. Starting from the analysis of the flat-field corrected mosaics, we want to prove the effectiveness of the F2M registration versus the F2F. In particular, we analyze the *RMSE* values reported in the rows 1 and 2 of Tab. 4.2. For every combination of warping models the *RMSE* values achieved by the mosaics built according to the F2M registration are always lower (for both  $\mu$  and  $\sigma$ ). The improvement achieved by the F2M registration can be appreciated also by a visual inspection of the mosaics. Figs. 4.15 and 4.16 report the mosaics obtained using the projective model according to configu-



**Fig. 4.15:** Mosaic SC30 according to the F2F registration. The mosaic has been obtained aligning the images of the set SC30 according to the projective warping model, flat-field correction and F2F registration. Inside the red box a detail highlighted in Fig. 4.17(a).

ration in rows 1 and 2, respectively. The two details highlighted in Fig. 4.17 show the improvement caused by the better alignment brought by F2M registration. Moreover, it is not obvious to obtain the best result performing F2M registration without the flat-field correction of the image. In fact, the non-homogeneity of the image intensity can have a bad influence on the geometric registration and F2M could also be worse than F2F. This happened, for example, for the mosaics obtained without the flat-field correction and according to the affine and projective models (column 2 and 3 of Tab. 4.2: value in row 3 versus row 4), where the average achieves better (lower  $\mu$ ) and more stable (lower  $\sigma$ ) *RMSE* values in the mosaics built without flat-field correcting.

### 4.6.3 Warping models

In the last section we proved the effectiveness of the flat-field correction and the F2M registration (especially when coupled) in the creation of the mosaic. Now, we focus our attention on the choice of the warping model. First, we an-



**Fig. 4.16:** Mosaic SC30 according to the F2M registration. The mosaic has been obtained aligning the images of the set SC30 according to the projective warping model, flat-field correction and F2M registration. Inside the red box a detail highlighted in Fig. 4.17(b).

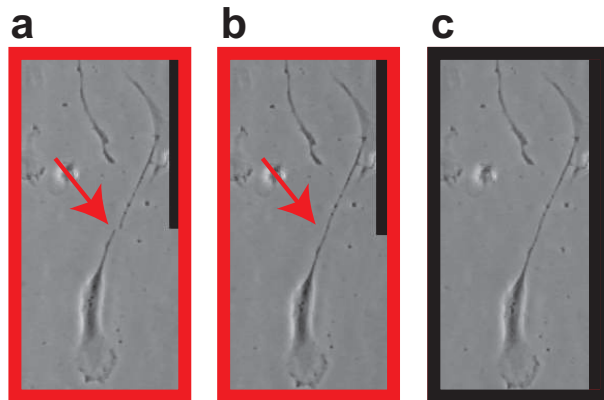


**Fig. 4.17:** Comparison between two details of mosaic SC30. (a): this figure highlights a detail of Fig. 4.15. The border of the cell is not continuous due to a misalignment caused by F2F registration. (b): detail of Fig. 4.16. It refers to the same regions of (a), but the border of the cell is now continuous, due to perfect alignment typically obtained when the F2M registration is employed. (c): detail from the first image aligned into the mosaics. It is shown as ground truth. No misalignment is visible comparing (b) and (c).

analyze the values related to the mosaics built according to the F2M registration and the flat-field correction, proving to be the best choice to build mosaics. The first row of Tab. 4.2 reports  $\mu$  and  $\sigma$  of the 29 *RMSE* values related to the mosaics built with translative, affine and projective warping model. The translative model brought the worst results (also confirmed by a larger std) on average. This proves that the mechanical motion of the holder and the relative deviation of the camera's optical axis from the normal to the holder is not so neglectable as expected. On the contrary, values for the affine and projective models are similar, meaning that the assumptions staying behind the affine model hold for a general widefield microscope. Looking to the first two rows of Tab. 4.2, it is worth noticing that on average with flat-field correction the translative model is always the worst one while the projective model is the best one, although it is not true for mosaics built without the flat-field correction. This is not completely unexpected, because without performing the flat-field correction the geometric registration could be less accurate due to the non-homogeneity of the image intensities and F2M registration could also perform worst than F2F (row 3 of Tab. 4.2 versus the value reported in row 4) and the projective model can not result as being the best choice. For the mosaics obtained without the flat-field correction and according to the F2F registration (row 4 of Tab. 4.2) the best and most stable result (considering both *RMSE*  $\mu$  and  $\sigma$ ) was achieved by the affine model. Nevertheless, analyzing the results referring to the mosaics obtained according to the F2M registration (value reported in row 3 of Tab. 4.2), we can see that the lowest  $\mu$  value is achieved when using the projective model and the lowest  $\sigma$  is obtained with the translative model, this meaning a greater stability of the latter one. In addition, the mean values achieved by the affine and projective models are always lower than those related to the translative model. Accordingly, contrarily to what expected and often repeated in the literature, we have proved that to create mosaics of images with a widefield microscope the affine or the projective models are more suitable than the translative one.

To confirm this finding and to better compare the mosaics obtained according to the different warping models, for every mosaic we performed an additional registration step: we registered the first image also as the last one (always using a simple additive F2F registration) and we computed *NEN* (Eq. 4.22) on the global registration matrix obtained. The *RMSE* is considered a joint tonal and geometric metric because it depends on both the tonal and geometric registration errors. On the contrary, *NEN* is a quantitative measure

regarding the geometric registration only. Theoretically, a perfect looping path registration should generate an identity matrix.  $NEN$  measures the distance between the obtained registration matrix and the identity. Tab. 4.3 reports

$NEN$ values			
Algorithm's configuration	Model		
	Translative	Affine	Projective
F2M with flat-field correction	2.18	1.68	1.07

**Tab. 4.3:**  $NEN$  value using SC30.  $NEN$  values computed using the images of the set SC30.

the  $NEN$  values achieved by registering the images according to the different tested warping models. As one can see, the highest  $NEN$  is achieved by the translative model, while the projective model is definitely the best.

#### 4.6.4 Results using the histological specimen

For a more generic analysis, we performed the same experiments also using the images of the set BT40. Being these images characterized by a higher contrast and more details as against images of living cells, feature detection and matching tasks result easier to be performed. As done for the set SC30, the 40 images of the set BT40 have been aligned according to the algorithm's configuration reported in Sect. 4.6.1.  $\mu$  and  $\sigma$  of the 39  $RMSE$  values are computed using the first 39 images registered into the mosaics are reported in Tab. 4.4. As expected, all the considerations made for the set SC30 still hold. The flat-field correction always brings an improvement. Figs. 4.18 and 4.19 report the mosaics obtained according to F2F registration and translative warping model. The mosaic in Fig. 4.19 is obtained performing the flat-field correction. F2M performs better than the F2F for all the transformation models (Fig. 4.20). In addition, it is worth remarking that the translative model always performed the worst. It is interesting to note that for this set the  $RMSE$  values relative to the mosaics built according to the affine and the projective model are often characterized by same  $\mu$  and  $\sigma$ . This is probably due to a very accurate feature detection and matching, due to a high contrasted texture. This minimizes errors of the parameters' estimation of the two models, both being a

<i>RMSE</i> values ( $\mu \pm \sigma$ )			
Algorithm's configuration	Model		
	Translative	Affine	Projective
a: F2M with flat-field correction	6.64±2.46	2.31±0.19	2.31±0.19
b: F2F with flat-field correction	7.52±3.70	2.91±1.77	2.96±1.92
c: F2M without flat-field correction	8.00±2.74	4.45±1.04	4.43±1.04
d: F2F without flat-field correction	8.62±3.74	4.58±1.22	4.58±1.22

**Tab. 4.4:** *RMSE* values using BT40. Mean and standard deviation of the *RMSE* values computed using the images of the set BT40.

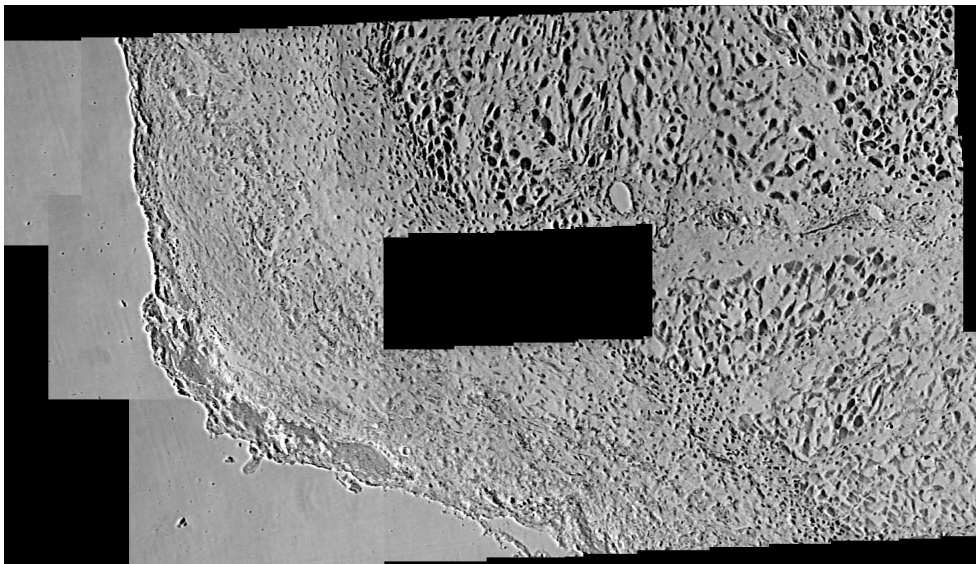


**Fig. 4.18:** Mosaic BT40 without flat-field correction. The mosaic has been obtained aligning the images of the set BT40 according to the translative warping model, F2F registration, no flat-field correction.

good approximation of the reality for the widefield microscopes.

To analyze more in detail the different warping models, we leaved the analysis of a joint tonal and geometric error such as the *RMSE* in favor of the analysis of *NEN* that measures the geometrical registration error only. As done for the set SC30, for every mosaic we performed an additional registration step registering the first image as the last one and computing the *NEN* on the

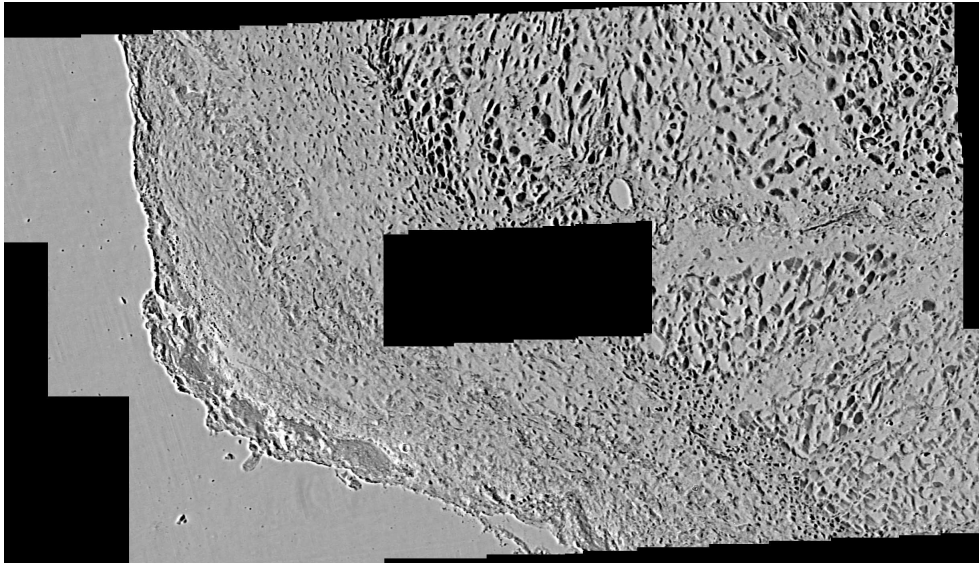


**Fig. 4.19:** Mosaic BT40 with flat-field correction. The mosaic has been obtained aligning the images of the set BT40 according to the translative warping model, F2F registration, flat-field correction.

global registration matrix obtained. Tab. 4.5 reports the *NEN* values achieved

<i>NEN</i> values			
Algorithm's configuration	Model		
	Translative	Affine	Projective
F2M with flat-field correction	0.48	0.31	0.31

**Tab. 4.5:** *NEN* value using BT40. *NEN* values computed using the images of the set BT40.

by registering the images (flat-field corrected and using the F2M registration) according to the different warping models. As for the set SC30, the highest *NEN* (worst result) is again achieved by the translative model, making the projective (or affine) model more suitable for creating mosaics with a widefield microscope.

### 4.6.5 Histological sample versus cell culture

In this section we carry out a comparative analysis of the results achieved using the BT images versus the SC ones. Generically, histological sample images are characterized by a higher contrast and more details than cell culture images. Figs. 4.21 and 4.22 report the grey level histograms of the mosaic in Figs. 4.13 and 4.18, respectively, normalized by the total number of pixels of the mosaics. The values at boundaries of the range of the main intensities (defined according to  $\mu \pm 3\sigma$ ) are reported in red. The histograms of the other mosaics built according to the different algorithm's configurations are comparable.

The main intensity range ( $6\sigma$ ) of the BT images is four times as much as the one of the SC images (BT: raw range  $\approx 200$  grey levels,  $6\sigma$  interval  $\approx 120$  grey levels; SC: raw range  $\approx 120$  grey levels,  $6\sigma$  interval  $\approx 30$  grey levels). The *RMSE* is based on intensity differences. The larger range of the BT images is the main cause of the higher *RMSE* values reported in Tab. 4.2 versus the ones in Tab. 4.4 (see Tab. 4.6 for a quick comparison). In fact, being standard

Algorithm's configuration	Model		
	Translative	Affine	Projective
<b>SC30</b>			
<i>RMSE</i> values ( $\mu \pm \sigma$ )			
1: F2M with flat-field correction	2.67 $\pm$ 0.98	2.05 $\pm$ 0.20	2.02 $\pm$ 0.16
2: F2F with flat-field correction	3.49 $\pm$ 1.34	2.13 $\pm$ 0.25	2.12 $\pm$ 0.28
3: F2M without flat-field correction	4.43 $\pm$ 0.85	4.31 $\pm$ 1.23	4.30 $\pm$ 1.19
4: F2F without flat-field correction	4.96 $\pm$ 1.31	4.18 $\pm$ 0.76	4.29 $\pm$ 0.95
<i>NEN</i> values			
F2M with flat-field correction	2.18	1.68	1.07
<b>BT40</b>			
<i>RMSE</i> values ( $\mu \pm \sigma$ )			
a: F2M with flat-field correction	6.64 $\pm$ 2.46	2.31 $\pm$ 0.19	2.31 $\pm$ 0.19
b: F2F with flat-field correction	7.52 $\pm$ 3.70	2.91 $\pm$ 1.77	2.96 $\pm$ 1.92
c: F2M without flat-field correction	8.00 $\pm$ 2.74	4.45 $\pm$ 1.04	4.43 $\pm$ 1.04
d: F2F without flat-field correction	8.62 $\pm$ 3.74	4.58 $\pm$ 1.22	4.58 $\pm$ 1.22
<i>NEN</i> values			
F2M with flat-field correction	0.48	0.31	0.31

**Tab. 4.6:** Summary of the *RMSE* and *NEN* values of the sets SC30 and BT40.

deviation also a contrast metric, comparing the  $\sigma$  values of the two histograms is clear that the BT images are characterized by a higher contrast (BT:  $\sigma \approx 20$ ; SC:  $\sigma \approx 5$ ). The feature detection and matching stage guides the registration. Images with a high contrast are simpler to register thanks to a number of more robust features that make the matching task more accurate. The lower *NEN* values yielded by the mosaics using BT confirm the better registration accuracy than the SC mosaics.

### 4.6.6 Computational performance

In the experiments the images have been aligned into the mosaics off-line. Nevertheless, the method chosen as well as its computational performance makes the algorithm suitable for on-line processing and, in the future, for real-time applications, allowing building the mosaic directly during the specimen's inspection. The tests have been performed using an off-the-shelf PC (Intel Core i5, CPU 2.27GHz, 4GB RAM) processing  $640 \times 512$  8-bit gray levels images stored on the hard disk. In particular, the computational cost of the Phase Correlation stage is approximatively 250 ms, and 250 ms more are due to the matching and warping stages. The most intense computational burden is due to mosaic updating and visualization, that increases as the size of the mosaic. We measured the elapsed time needed to build a 40 image mosaic according to the most CPU intensive registration configuration (full-resolution, F2M, projective model) and the average computational time was 10 sec per frame. No part of the algorithm has been optimized and the strategies adopted for efficient rendering and visualization of the mosaics are beyond the scope of the thesis. Since at the moment the algorithm is implemented on a research prototype, we are confident that a further optimization stage can be applied to improve on the computational performances also towards *real-time*, compliantly with the common user behavior.

## 4.7 Conclusion and future work

### 4.7.1 Conclusion

In this work we developed a software tool to build mosaics of images acquired with general non-motorized widefield microscopes. The focus of the work was not necessarily the improvement of the state of the art. Rather, the purpose was defining, setting up and implementing a methodology for testing and comparing different vignetting correction approaches. In addition, we took the opportunity to assess different registration approaches and warping models. In fact, we implemented and deeply validated interesting solutions for the on-line mosaic creation, releasing a software that can easily be exploited by users to test different algorithm's configuration. In particular, we used images of histological specimens and cell cultures, that cover the most relevant part of the routine examinations performed in the biological laboratories, and we tested the algorithm using two different geometric registration strategies (frame-to-frame and frame-to-mosaic) and three different global warping models (translative, affine and projective).

We performed several experiments to validate the proposed mosaicing method under different parameters' setups. The analysis of the proposed joint tonal and geometrical registration errors results in three main conclusions. (i) First, as expected the tonal correction always improves the final mosaics. Also, mosaics of flat-field corrected images are visually more pleasant because the seams in the stitching zones are strongly attenuated. Furthermore, the flat-field correction helps the next stage of geometric registration, because the feature detection and matching steps are more accurate when the images to be registered are normalized so to be characterized by a homogeneous signal distribution. (ii) Second, by using mosaics of images flat-field corrected we compared two different geometric registration strategies: frame-to-mosaic and frame-to-frame. We confirmed that the frame-to-mosaic registration performs better and the most relevant improvements are realized when working with vignetting corrected images. (iii) Third, analyzing the joint tonal and geometrical error and the geometrical registration error alone we proved that the assumption regarding the perpendicularity of the microscope's holder to the optical axis in general does not hold. In fact, we found the projective warping model being the most suitable choice to build microscopy image mosaics.

Besides, we showed that the affine model, rather than the translative one, can be also a good solution, but this mainly depends on three issues: working distance between the camera principal point and the observed specimen typology, amplitude of angular inclination of the holder and relation between the inclination of the holder and its motion direction. In particular, as far as the latter issue concerned, the worst result is obtained if the images are acquired moving the holder along the direction of its maximum inclination. To conclude, if no prior information regarding the instrumentation system is available, we suggest to employ the projective warping model coupled with the frame-to-mosaic geometric registration of tonal corrected images as the best solution to build mosaics of images acquired with widefield, even non-automated, microscopes. Finally, the experiments performed and the obtained results proved that the method could be effectively employed to obtain mosaics on-line, after a proper optimization.

The realized software prototype and all the images used in the experiments can be provided on demand [11].

The content of this chapter was partly published in [23, 22].

### 4.7.2 Future work

Several improvements can be considered as future work. First, a strategy for flat-field correcting the single images has to be devised to effectively obtain color mosaics. At this moment, the colour images are flat-field corrected normalizing all the channels with the same vignetting function. A better solution could be to analyze separately each channel for estimating its specific vignetting function. Furthermore, to fix problems such as the generation of false colours, a dynamic remapping look-up-table can be used to provide a single RGB colour for each grey level of the converted original image. A second improvement regards the extension of the method from light microscopy to general widefield microscopy, fluorescent microscopy included. The proposed method also works to build mosaics of fluorescent images, but the photobleaching decay is not considered and in the final mosaic the objects imaged more times present an intensity decay. Furthermore, the photobleaching can have a bad influence on the feature detection and matching stage, producing non-accurate alignments. In order to develop a mosaicing approach that could be

robust also with fluorescent images, these must be normalized to have the same intensity distribution. A solution based on vignetting correction only is not enough, since also the photobleaching effects have to be compensated. This could be accomplished using a function estimated arising from a set of intensity grey level based decay curves. Finally, the approach proposed to compare the different warping models can be utilized to develop an application providing a feedback on the inclination status of the microscope's holder. The translative model could give some results as the projective model in case the holder is perfectly perpendicular to the microscope's optical axis. This knowledge and the proposed mosaicing approach could be employed together to develop a user-friendly application to calibrate the microscope.

## 4.8 Acknowledgments

I thank Dr. Ludovico Carozza (School of the Built Environment at Heriot-Watt University, Edinburgh, United Kingdom) for providing some algorithms and data already published in his PhD thesis [176], Dr. Enrico Lucarelli and his staff of the Osteoarticular Regeneration Laboratory (Rizzoli Orthopaedic Institute, Bologna, Italy) for important discussions and helping me to prepare the biological samples.

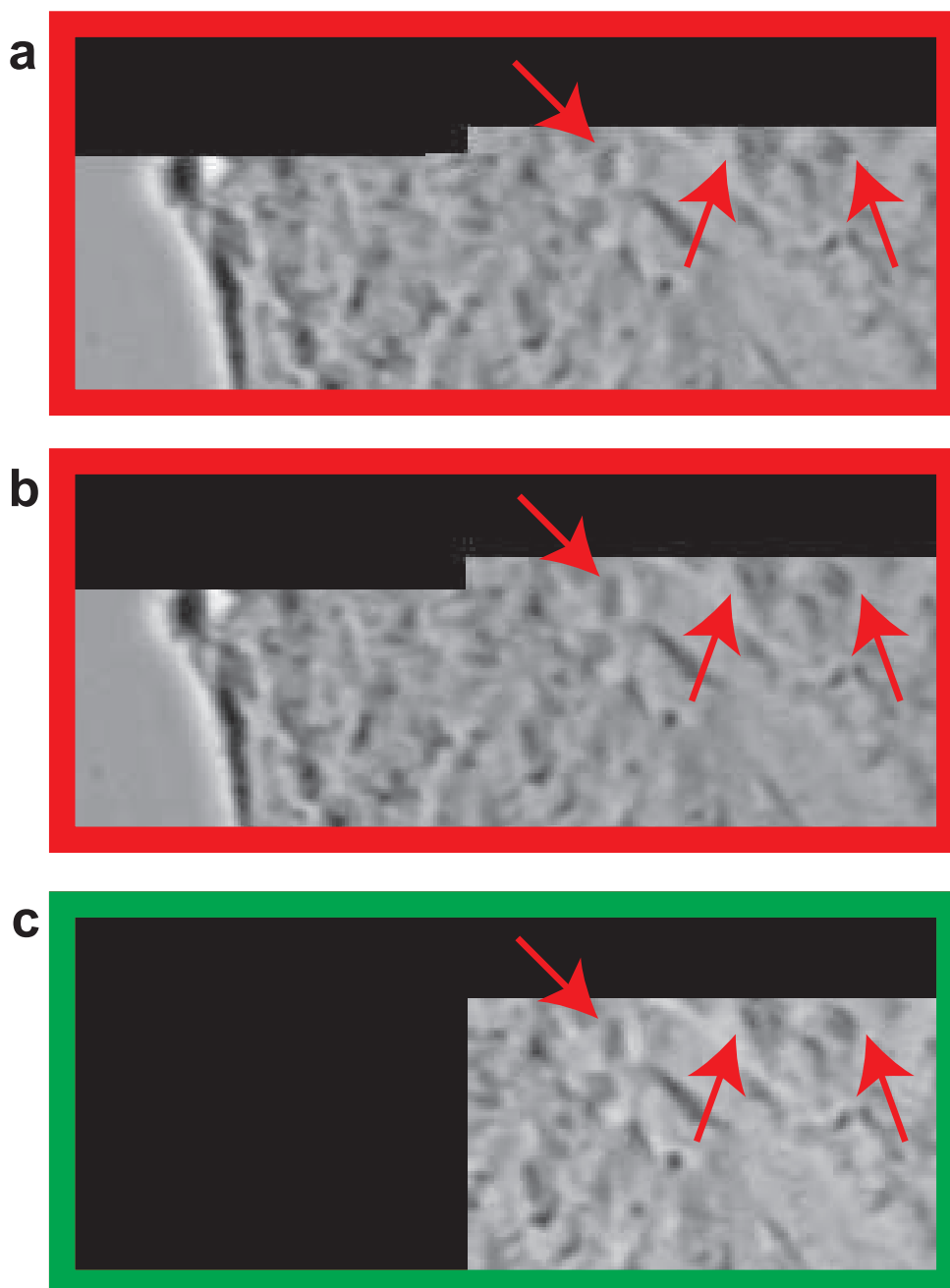


**Fig. 4.20:** Comparison between two details of mosaic BT40. (a): this figure highlights a detail from the mosaic obtained by aligning the images of the set according to the projective warping model, flat-field correction and F2F registration. The border of the tissue is not continuous due to a misalignment caused by F2F registration. (b): detail from the mosaic obtained aligning the images using the projective model, flat-field correction and F2M registration. It is the same region depicted in (a), but the border of the tissue is now continuous, due to perfect alignment obtained with the F2M registration. (c): detail from the second image aligned into the mosaics. It is shown as ground truth. No misalignment is visible comparing (b) and (c).

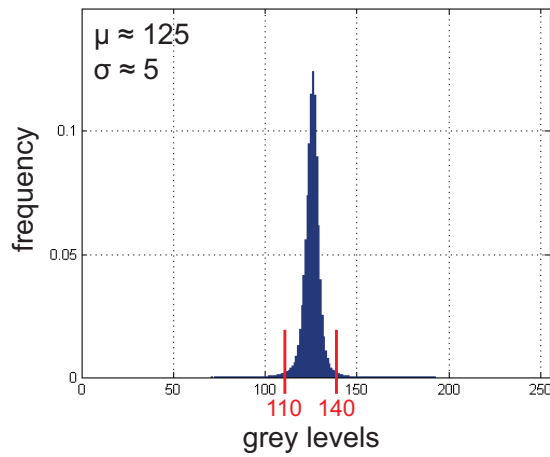


**Fig. 4.21:** Frequency of intensity levels of the SC mosaic reported in Fig. 4.13. In  $x$  the intensity values in grey levels (minimum and maximum value reported in red). In  $y$ , the frequency values.

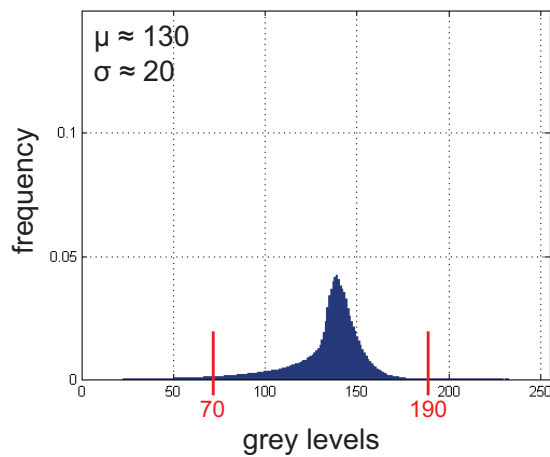


**Fig. 4.22:** Frequency of intensity levels of the BT mosaic reported in Fig. 4.18. In  $x$  the intensity values in grey levels (minimum and maximum value reported in red). In  $y$ , the frequency values.



# Chapter 5

## Depth of focus



**Fig. 5.1:** Depth of focus. Due to a narrow depth of focus the storm troopers are in different focus levels.

- F. Piccinini, A. Tesei, W. Zoli, A. Bevilacqua, Extended depth of focus in optical microscopy: assessment of existing methods and a new proposal. *Microscopy Research and Technique*, 15(11): 1582-1592, 2012
- F. Piccinini, A. Tesei, W. Zoli and A. Bevilacqua, Extending the Universal Quality Index to assess N-image fusion in light microscopy. *International Journal of Bioelectromagnetism*, 14(4): 217-222, 2012

## 5.1 Introduction

In widefield microscopy, the most relevant part of the biological routine examinations is performed by focusing the sample at the beginning and changing it during the inspection, in order to keep the parts of the sample at different depths sharp. In particular, glass slides and multi-well plates represent most of the common holders used to contain biological samples, typically tissues and cell cultures. While specimens are “planar” and lie in one single focal plane, multi-well plates have a  $z$ -dimension that cannot be neglected. Also, the latter can contain non-adherent cells that are distributed in a volume of culture medium, besides the well’s bottom being not perfectly flat. In this case, the cells can lie in more focal planes and, depending on the magnification factor, they can be also thicker than the depth of focus (or depth of field) of the system, meaning that it is not possible to acquire a whole cell completely in-focus in one single image [177]. This is a well known problem in biological imaging with common light microscopes, where algorithms for extending the depth of focus through digital processing have regularly been proposed since the 1970s [178, 179, 180]. Furthermore, if the final composite images are not obtained for visual purposes only, the fusion process can represent the early stage of other applications [181], such as 3D reconstruction [182, 183, 184] and virtual extension of the camera’s field of view (see Chap. 4). In all these cases, the performance of the fusion stage has important consequences for the accuracy of the entire process.

A microscope’s depth of focus is a function of the wavelength of the light source and the numerical aperture of the lens [185]. To understand how these parameters affect the depth of focus it is necessary to analyze its mathematical formulation. Physically, the depth of focus ( $d$ ) for thin lenses is defined according to Eq. 5.1:

$$d = \frac{\lambda}{ri \cdot \sin^2 \alpha} \quad (5.1)$$

where  $\lambda$  is the (monochromatic) wavelength of the light source,  $\alpha$  the semi-aperture of the angle subtended at the lens by an object and  $ri$  the refractive index of the medium interposed between optics and specimen. In particular,  $ri$  can depend on many different materials and substances that are crossed by the light rays. Typically, air or oil is between the tip of the lens and the holder of the sample. In addition, if it is a glass slide, a plastic coverslip is

placed over the samples. Instead, in case of multi-well plates, a lid seals the wells (usually made of plastic) that often, during inspections, contain air and culture medium. The denominator of Eq. 5.1 can be written also as a function of the numerical aperture  $NA$ , for thin lenses defined according to Eq. 5.2:

$$NA = ri \cdot \sin \alpha \quad (5.2)$$

The depth of focus is inversely related to the magnification factor  $M$  of the used lens [186] (Eq. 5.3):

$$NA = constant \cdot M \quad (5.3)$$

indicating that it is impossible to acquire complete 2D in-focus images of objects characterized by a wide  $z$ -dimension, e.g. multicellular spheroids [187] (Fig. 5.2), or even single cells using high-magnification lens.

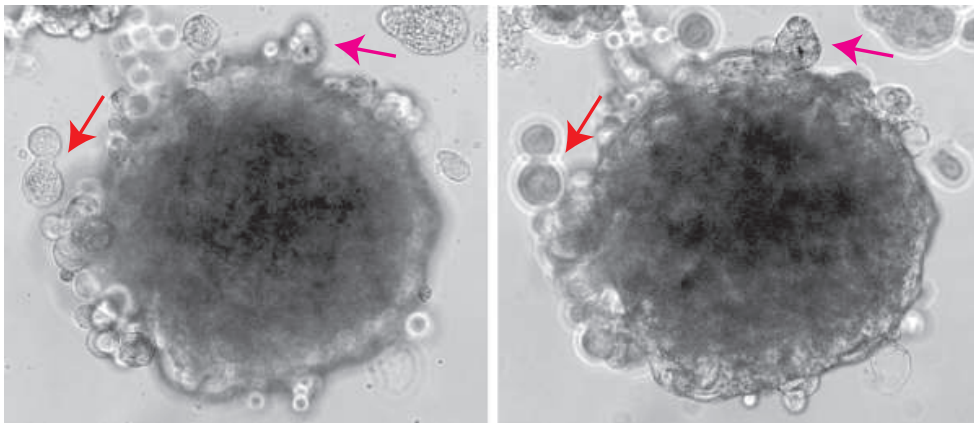


**Fig. 5.2:** Lung cell spheroid (bronchosphere). It is not possible to acquire a single completely in-focus image of objects characterized by a wide depth, such as the multicellular spheroid, using standard light microscopes. Moving the microscope's holder in the  $z$ -direction it is possible to acquire optical slices at different focus levels, thus achieving different in-focus regions of the object. The images show a couple of  $z$ -aligned slices pertaining to a bronchosphere, acquired in brightfield using a standard light microscope. In this case, the magnification factor was  $10\times$  and the spheroid's diameter is 422 pixels  $\approx 270 \mu\text{m}$ . In the left image, small particles near the major spheroid are in-focus, whereas they are blurry in the right one, where the circular crown at the border of the spheroid is in-focus.

Numerous methods have been proposed in literature to extend the microscopes' depth of focus through digital processing. Usually, such methods start

by building a stack of images acquired by simply shifting the microscope's holder along the optical axis ( $z$ -direction) to achieve optical sections (slices with adjacent in-focus regions) of the specimen [188]. If the dimensions of the object are much larger than the depth of focus, only a small portion of each slice will be in-focus and different regions of the object will be in-focus in different slices. Generally, the extended depth-of-focus methods aim at recovering the in-focus pixels from each single slice of the stack and at building the final single composite image (mainly informative and suitable for visual inspection or quantitative analyses performed on the whole cell) by combining information through image fusion processing [189]. Commonly, they rely on the assumption that the slices of the stack are perfectly  $z$ -aligned and that the objects of interest are still. A tentative classification of the different methods yields two different groups, each based on their working domain:

- Spatial domain. Historically, these approaches were the first to appear in literature. Generally speaking, a pivot rule [178, 179, 190] based on properties of single pixels [191, 192] or their neighborhoods [185, 188] is followed to determine for each  $(x,y)$  position the in-focus slices between the images acquired at different  $z$  positions of the holder.
- Frequency domain. The fundamental assumption is that among the different representations of the same scene, the most in-focus image contains more details and thus more high frequency components. Therefore, to reconstruct the final in-focus image, the local high-frequency components are analyzed between the slices of the stack. These approaches were first used at the beginning of the 1990s to deal with application domains not including microscopy [193, 194]. Since then, numerous other approaches based on wavelet [186] or curvelet transforms [177] have been proposed.

A review of literature image fusion methods of both classes was published by [184].

The large number of extended depth-of-focus methods proposed in literature and the lack of validated approaches to compare them makes the choice of the best method for one's need quite difficult [195]. Numerous quality metrics have been developed to numerically compare images and evaluate performance of fusion algorithms [196, 197, 198]. One widely used index is the Universal Quality Index ( $UQI$ ) proposed by the authors in [105]. Although  $UQI$  is not

explicitly based on any representation of the human visual system, the authors show that it is the index representing the image quality most closely resembling that of human visual perception. This metric requires a reference ground truth to be evaluated, which may not always be available in experimental settings [199]. To overcome this problem, a widely used extension of the *UQI* metric was proposed by the authors in [106]. This metric, known as Piella's Metric (PM), does not require any reference and enables methods based on the fusion of only two information sources to be compared. A further extension of PM was proposed by [200]. This metric, hereafter referred to as *UQIN*, is suitable to compare performances of methods where  $N$  images are used to obtain the final composite image. Although both PM and *UQIN* metrics are conceived to be extensions of *UQIs*, no exhaustive analyses have been carried out to study the correlation between their numerical output and that of the original *UQIs*.

In the present thesis a new extensive evaluation approach to numerically compare the performance of extended depth-of-focus methods is proposed. The experiments were carried out using stacks of both synthetic and real images. In particular, the approach followed to analyze the final composite image built using real ones provides an important strategy to help operators choosing the most suitable method for their own purposes. A new extended depth-of-focus method (hereafter called **Depth Of Focus Extender** - DOFE) for both gray-levels and colour images is also proposed, based on a spatial pixel-wise analysis of the source images used to obtain the composite image. Despite the simplicity of the proposed implementation, the experimental results obtained using synthetic stacks show that the method gives a better quality performance than state-of-the-art methods. With regard to real stacks, visual and numerical analyses indicate that results are at least comparable to those of the other methods considered.

## 5.2 State of the art

Many methods have been proposed in literature during the last decades to extend the microscopes' depth of focus. Despite that, only few are freely available and can be practically used in light microscopy. Aiming at assessing the quality of the proposed method, we compared the results achieved with

those of five other different extended depth-of-focus software tools. Four are widely used methods and implemented in ImageJ [96], one of the most common open source programs used for image processing. In particular, **Stack Focuser** (SF) and **Depth From Focus** (DFF) are available directly from the ImageJ Plug-In web section and the other two software tools from the website of the Biomedical Imaging Group (BIG) of the Ecole Polytechnique Federale de Lausanne (EPFL) [201]. They are called **Complex Wavelet-Based Method** (CWBM) and **Model-Based Method** (MBM). The last compared software tool is a very promising method based on **CURvelet** transform and it is implemented in MATLAB (hereafter referred to as CUR method).

SF [202] works in the spatial domain and it is based on three steps: first, each image of the stack is processed using a spatial median filter (fixed size  $3 \times 3$ ) and the Sobel edge detector to find out the in-focus regions. Second, assuming that the regions near an in-focus edge are also in-focus, a spatial maximum filtering is performed on each image to propagate the local maximum values. Finally, a maximum  $z$ -selection is made to build the indexed map containing, for each  $(x,y)$  position, the index of the image from which the pixel is taken to be copied into the composite one. The software also works on colour images by analyzing each channel separately. It permits and requires one input parameter only to be changed (i.e., the dimension of the squared kernel (morphological structuring element) for the spatial maximum filter, by default set to 11).

DFF [203] uses a quality metric called “sharpness index” [185] to detect in the spatial domain the in-focus regions on slices, before allowing maximum  $z$ -selection to be made (similarly to SF). The sharpness index is based on a sliding window analysis using a squared kernel. This index weights the effect of the corner pixels to be the same as the orthogonal ones and sums the magnitudes of the differences. Within the software, the kernel side of the sharpness index is by default set to 3.

CWBM [186] exploits the complex wavelet transform to locally analyze and define the in-focus regions of each single image of the stack subsequently used to build the final composite image. A number of input parameters are required, e.g. filter size and number of decomposition scales, although default values are suggested.

MBM [182] deals with the extension of the depth of focus as a deconvolution

optimization problem where the texture of the object and its topography are jointly estimated in an iterative process. The Point Spread Function (PSF) of the system is required as an input parameter, but the authors affirm that their approach is fairly insensitive to this parameter. They also claim that the approximation method proposed to estimate the PSF results in a composite image without any significant loss in accuracy. The resulting composite image is of a very high quality, paying a higher computational cost when compared with wavelet-based approaches.

CUR implements an image fusion method that works in the frequency domain [177]. Starting from the assumption that an in-focus region contains more high frequencies than blurry regions, the authors used the curvelet transform [204] to separate the high frequency image content and to reconstruct the final composite image stemming from the in-focus regions. The coefficients with the highest absolute value at each position, orientation and scale are selected to ensure that the most salient image features throughout the stack are preserved. This maximum absolute value selection rule is similar to those typically used in wavelet-based image fusion methods, but thanks to the high directional sensitivity of the curvelet transform the method achieves high average performance. CUR is implemented in MATLAB using functions obtainable upon request from the authors' website [205]. Our CUR implementation is achievable upon request [11].

It must be stressed that almost all the parameters of the methods tested were left at the default values suggested by authors. The best parameter setting was selected through dedicated test analyses only for the number of decomposition scales in CWBM, finally fixed at six scales.

## 5.3 Methods

As explained in Sect. 5.1, all the extended depth-of-focus methods suitable for microscopy applications start by exploiting a stack of optical sections of the specimen, acquired by moving the microscope's holder along the optical axis (the  $z$ -direction) and assuming that the imaged objects are still. Historically, the first methods proposed in literature were those working in the spatial domain and, according to [182] and [186], their quality performance should be

overcome by those of the frequency-based approaches. Nevertheless, their simplicity and ease-of-use make them very attractive. Taking into consideration the different solutions proposed in literature, we conceived and designed a new easy-to-use method to obtain high quality fused images. Typically, all the spatial approaches are based on two consecutive fundamental steps: *detection* and *fusion* of the in-focus regions of a stack of optical sections of the specimen to obtain a final composite in-focus image [179, 190].

We analyzed the different solutions proposed for both *detection* and *fusion* step and, as the rule for the *detection* of the in-focus regions, we assumed that for each region the best in-focus image, between more representations (optical sections) of the same scene (still objects), is defined as the image containing more details for that specific region [206]. Accordingly, to define the best in-focus image for each region we opted the simplest way to enhance details: a standard derivative process using the common  $x$ - $y$  central derivative, typically computed as root of the sum of the squared of the output masks, obtained convolving the image in both the directions by the 3-pixel linear structuring element with coefficients 0.5, 0,  $-0.5$ . To this purpose, a Sobel edge detection process, which performs the image filtering and edge enhancement stages in one step, is widely employed in literature [184]. However, for the sake of usability, we decided to separate the image filtering stage from the edge enhancement. In particular, for each single image of the stack firstly we computed the  $x$ - $y$  central derivative obtaining a new image containing in each pixel position the derivative value (hereafter called as to *derivative mask*). Then, we computed a simple mean filter of large size (size set by default to  $15 \times 15$  pixels) on the derivative mask obtained, to filter out the high local derivative values due to noise. This permits to propagate the influence of small areas characterized by high derivative, based on the assumption that regions of contiguous object are in-focus in contiguous images.

Regarding the *fusion* step, a maximum selection rule is typically followed to combine the detected in-focus regions in order to obtain the final in-focus image [184]. The natural choice would be to perform for each  $(x,y)$  pixel position the selection of the higher  $z$ -value of the stack composed by the derivative masks obtained before. However, it was decided to aim for something more effective. First, we built a *index-map* reporting for each  $(x,y)$  pixel position the number of the derivative mask containing the higher  $z$ -value. Second, we performed a *majority filter* on the map [186, 194]. The majority filter is similar

to a mode-filter. In particular in such a filter, if more than half of the pixels contained in the squared sliding window (with size set by default to  $5 \times 5$  pixels) have the same value, that value is attributed to the pixel in the center of the window. Essentially the majority filter, again motivated from the physical assumption that objects in neighboring regions are in-focus in neighboring images, was performed to promote the continuity of the value of adjacent pixels. Finally, the composite image was built by exploiting the index-map and by copying for each  $(x,y)$  pixel position the intensity value in the original image pointed out by the index-map.

Mathematically, the final in-focus Image ( $I$ ) is built according to Eq. 5.4:

$$I(x, y) = S_n(x, y); \quad n = \text{index-map}(x, y) \quad (5.4)$$

where  $S_n$ ,  $n = 1, \dots, N$  is one of the  $N$  images aligned into the analyzed stack.

For a RGB colour space extension, a simple suggestion would be to prepare a three-channel matrix for the final composite image and to copy the vector containing the original RGB values from the image pointed out by the index-map for each  $(x,y)$  pixel position. In this case, the index-map is created as explained above, but with the original colour images pre-converted into gray-level. Microscopic images are usually characterized by predominant colours, especially if staining dyes or fluorescence proteins are used, and the standard RGB to gray-level conversion can lead to a substantial information loss. Where predominant colours exist, an optimal solution is to replace the standard weighting coefficients, in the standard RGB to gray-level conversion formula, with those obtained through the principal component analysis of the three channels of the original image, using the Karhunen-Loève transform [186, 177]. Using this strategy, the predominant colours of the images are preserved and the final gray-level representation retains higher information content, yielding an image with more contrast and saliency.

DOFE is fully implemented in MATLAB and it is available on request [11].

## 5.4 Quality metrics

Several metrics are used in literature to evaluate the output of image fusion methods and an extensive overview is provided in [59] and [195]. Some of the most widely employed metrics in image processing are Mean Squared Error (*MSE*), Signal to Noise Ratio (*SNR*) and Universal Quality Index (*UQI*) (already introduced in Sect. 2.5.5). *MSE* and *SNR* are also used in data and signal analysis and in image processing. We define  $MSE_{(G,I)}$  and  $SNR_{(G,I)}$  the *MSE* and the *SNR* of the images  $G$  and  $I$ . The specific formulas are reported for completeness in Eqs. 5.5 and 5.6, respectively.

$$MSE_{(G,I)} = \frac{\sum_x \sum_y [G(x,y) - I(x,y)]^2}{P} \quad (5.5)$$

$$SNR_{(G,I)} = 10 \log_{10} \frac{\sum_x \sum_y G(x,y)^2}{P \cdot MSE_{(G,I)}} \quad (5.6)$$

$G$  is the reference ground truth,  $I$  is the image to be evaluated (here, the final composite image),  $(x,y)$  is the pixel coordinate and  $P$  is the number of pixels of  $G$  and  $I$ .

Conversely, *UQI* is a metric used for image evaluation only. It is designed by modeling any image distortion as a combination of three factors: loss of correlation, luminance distortion and contrast distortion, according to Eq. 5.7:

$$UQI_{(G,I)} = \left( \frac{v_{(G,I)}}{\sigma_G \cdot \sigma_I} \right) \cdot \left( \frac{2 \cdot \mu_G \cdot \mu_I}{\mu_G^2 + \mu_I^2} \right) \cdot \left( \frac{2 \cdot \sigma_G \cdot \sigma_I}{\sigma_G^2 + \sigma_I^2} \right) \quad (5.7)$$

$\mu_G$ ,  $\mu_I$ ,  $\sigma_G$ ,  $\sigma_I$  and  $v_{(G,I)}$  are mean, standard deviation and covariance, respectively, of the images  $G$  and  $I$ . The first component is the well known correlation coefficient which measures the degree of linear correlation. The second and the third components measure luminance distortion and contrast distortion of  $G$  and  $I$ , respectively [105]. A common characteristic of these three metrics is that they require a reference ground truth to evaluate image quality. Unfortunately, this is often unavailable in fusion problems aimed at reconstructing one real world, in-focus image [199]. To overcome such a problem, [106] proposed a *UQI* extension (PM) that is suitable for estimating the quality of composite images using only two input slices of the stack, without the need for a reference ground truth. PM was then extended by [200] to another metric, *UQIN*, suitable for exploiting not just two slices but all the

$N$  frames of the stack. The basic version of the  $UQIN$  metric is reported in Eq. 5.8:

$$UQIN_{(S_1, \dots, S_N, I)} = \frac{1}{|T|} \sum_{w \in T} \sum_{n=1}^N \gamma_{(S_n|w)} UQI_{(S_n, I|w)} \quad (5.8)$$

where  $S_n$  is a image out of the  $N$  slice used to build the final composite image  $I$  (for PM,  $N=2$ ),  $w$  is a small Region Of Interest (ROI) of the collection  $T$  in which the image is subdivided and  $\gamma_{S_n}(w)$  is defined according to Eq. 5.9:

$$\gamma_{(S_n|w)} = \frac{Y_{(S_n|w)}}{\sum_{n=1}^N Y_{(S_n|w)}} \quad (5.9)$$

where  $Y_{(S_n|w)}$  is the local saliency of the image  $S_n$ , typically defined as the image variance in the ROI  $w$ . Three different versions have been proposed for both PM and  $UQIN$ , by simply introducing different weighting functions applied to the equation terms. Eq. 5.10 reports the formula for  $UQIN2$ , the second version of  $UQIN$ :

$$UQIN2_{(S_1, \dots, S_N, I)} = \frac{1}{|T|} \sum_{w \in T} \sum_{n=1}^N C_w \gamma_{(S_n|w)} UQI_{(S_n, I|w)} \quad (5.10)$$

The weighting function is defined according to Eq. 5.11:

$$C_w = \frac{Y_{(S_1, \dots, S_N|w)}}{\sum_{n=1}^N Y_{(S_1, \dots, S_N|w)}} \quad (5.11)$$

where  $Y_{(s_1, \dots, s_N|w)}$  is the overall saliency inside window  $w$ , considering all the images  $s_1, \dots, s_N$ , and it is defined as the maximum of the of the  $Y_{(s_n|w)}$  with  $n = 1, \dots, N$ . Finally,  $UQIN3$  (the last version of the  $UQIN$ ) is reported in Eq. 5.12:

$$UQIN3_{(S_1, \dots, S_N, I)} = UQIN2_{(S_1, \dots, S_N, I)}^{(1-\beta)} \cdot UQIN2_{(S_1^e, \dots, S_N^e, I^e)}^\beta \quad (5.12)$$

where  $S_n^e$  and  $I^e$  are the edge version of the corresponding images and  $\beta$  is the edge contribution parameter.

It is worth noting that typically the methods' ranks computed according to  $UQIN$ ,  $UQIN2$  and  $UQIN3$  result different [106]. To overcome the lack of a standard metric to rank different methods, we propose a new metric simply by exploiting the basic definition of  $UQI$ . On the basis of [105], the standard  $UQI$  aims at mimicking the human visual perception to assess similarity between

images. Ideally, an in-focus image obtained from an extended depth-of-focus method should be corrected for the blurring effect within the defocused regions in each slice of the processed stack, where only a portion of each slice is in-focus. Accordingly, the more effective the extended depth-of-focus method, the higher the contribution in terms of blur compensation retained by the final composite image with respect to each slice. By quantifying these contributions in terms of image dissimilarities, a better-quality final composite image should be more dissimilar, on average, from the processed slices, thus yielding a higher image dissimilarity score. Following this assumption, we defined the new metric Average  $UQI$  (hereafter,  $AUQI$ ).  $AUQI$  is defined as the average of the  $N$  values obtained computing the  $UQI$  value between the obtained final composite in-focus image  $f$  and the  $N$  slices  $s_n$  of the original stack [207, 208]:

$$AUQI(s_1, \dots, s_N, f) = \frac{1}{N} \sum_{n=1}^N UQI(s_n, f) \quad (5.13)$$

$AUQI$  and the standard  $UQI$  are proposed as global indexes, without an implemented weighting function. Instead, all the versions of  $UQIN$  are defined as weighted local indices and this could play an important role in image rankings.

Our MATLAB implementation of  $MSE$ ,  $SNR$ , standard  $UQI$ , the different versions of  $UQIN$  and  $AUQI$  are available on request [11].

## 5.5 Materials

We used several synthetic and real image stacks, representing slices of fixed objects acquired by moving the microscope holder at different  $z$ -positions, to perform an extensive analysis of the quality performance achievable with DOFE. In particular, the synthetic stacks permitted us to exploit all the common quality metrics such as  $UQI$ ,  $MSE$  and  $SNR$ , which require a reference ground truth, not available when using real stacks [196]. The synthetic stacks (of eight images each) were constructed starting from five images, with very different contents, taken from the Brodatz texture database [209]. In particular, we used images D13, D22, D23, D61, D112 (Fig. 5.3). D13 and D61 can be considered similar to bone tissue, D22 to a lung biopsy, and D61 and D112 to cell cultures.

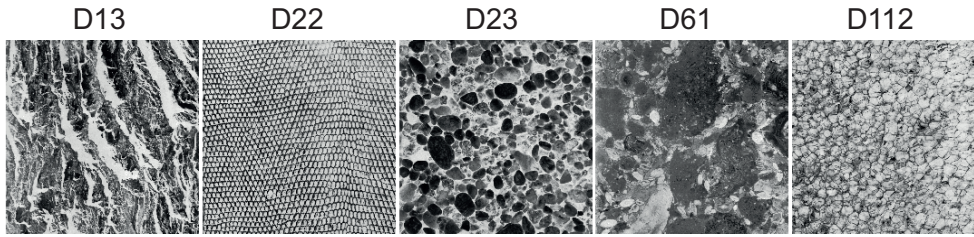


**Fig. 5.3:** Brodatz textures. Gray images from the Brodatz textures database [209] used to build the synthetic stacks of slices utilized in the experiments to compare the performance of the different extended depth-of-focus methods tested. From left to right: D13, D22, D23, D61, D112. D13 and D61 can be considered similar to bone tissues, D22 could recall a lung biopsy, and D61 and D112 cell cultures.

To build the synthetic stacks of partially-unfocused slices we exploited the specific function available through the MBM interface and previously used by the authors in [182, 186]. This function simulates the acquisition of images at different focal planes, by projecting the original 2D Brodatz texture  $T(x,y)$  used as a template onto a 3D Surface  $S(x,y)$ . In practice, the objects in the scene are considered as not being in motion and the image acquisition stage is simulated by moving the microscope's holder in the  $z$ -dimension (constant  $x$  and  $y$ ) only. The images are acquired at constant depth intervals. The single synthetic images are built according to the following steps.

1. The 3D shape of the projection surface is by default defined as a “dome”, with  $S(x,y)$  defined by the biquadratic function (Eq. 5.14):

$$S(x,y) = \left[ 1 - \left( \frac{2x}{W} - 1 \right)^2 \right] \left[ 1 - \left( \frac{2y}{H} - 1 \right)^2 \right] \quad (5.14)$$

$W$  and  $H$  are width and height of  $T(x,y)$  and  $x$ - $y$  the pixels' coordinate. For each  $x$ - $y$ ,  $S(x,y)$  represents the  $z$ -position of the surface of the dome according to the three axis of the Cartesian reference system (topography, bottom of Fig. 5.4a).

2. The intensity values of  $T(x,y)$  are orthographically projected onto  $S(x,y)$  (top of Fig. 5.4a). In practice,  $T(x,y)$  represents the intensity value in each 3D coordinate on the dome surface.

3. In order to simulate the optical system the volume of the dome is then convolved with a spatially-variant Gaussian Point Spread Function (PSF) with size increasing as the defocus distance increases (Eq. 5.15):

$$PSF(x, y, z) = \frac{1}{2\pi\tau^2} e^{-\frac{x^2+y^2}{2\tau^2}} \quad (5.15)$$

with  $\tau$  by default defined as reported in Eq. 5.16:

$$\tau = 0.2 + 1.3 |z| \quad (5.16)$$

4. Finally, the single synthetic images are obtained by sampling the dome volume at constant depth intervals with using linear interpolation along the  $z$ -dimension (Fig. 5.4b).

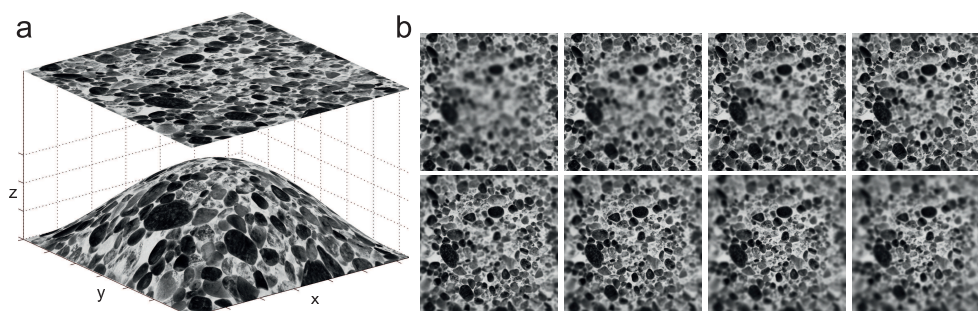


**Fig. 5.4:** Slices from synthetic stacks. The synthetic stack of slices was built using a function implemented in ImageJ and available through the MBM interface. In **(a top)** the original image is shown (Brodatz texture D23), projected on a 3D surface **(a bottom)**. In **(b)** the eight  $z$ -aligned synthetic slices obtained by sampling the 3D volume of Fig. 5.4a.

For real stacks, the objects are scanned by moving the microscope holder along the  $z$ -direction and images are (manually) acquired at prefixed constant distances. To build a wide real testbed we collected several stacks with very different content. In particular, we used the following four stacks (used by [182] and [186] and kindly furnished upon request): eye of the fly (32 14-bit images of  $1280 \times 1024$  pixels), Peyer's plaques from the intestine of the mouse (20 colour images of  $1996 \times 1450$  pixels), pancreatic buds stained with peroxidase (17 colour slices of  $400 \times 400$  pixels, extracted from a video) and a laser welding (13 colour images of  $1024 \times 768$  pixels). In addition, we acquired a stack of slices in brightfield referring to multicellular spheroids of human lung cells [187]. The

microscope was a Zeiss Axiovert 200 coupled with a Zeiss Achroplan  $10\times 0.25$  NA lens in air immersion and a Zeiss AxioCam MRc CCD camera. In order to obtain a ROI of  $611\times 531$  pixels containing the larger spheroid, the images were cropped. The  $z$ -stack consisted of 26 colour images with a  $z$ -step of  $5\mu\text{m}$ . It is worth noting that all the real stacks represented very different objects and also other parameters such as microscope, depth of focus and  $z$ -steps differ among stacks. Hereafter, these stacks will be referred to as FLY, INTESTINE, PANCREAS, LASER and LUNG (Fig. 5.5). Tab. 5.1 summarizes the



**Fig. 5.5:** Slices from real stacks. Images from the real stacks of slices used in the experiments. In each slice only few regions are in-focus. The reported images are taken from the middle of the stacks and are converted into gray-levels. From left to right: eye of the fly, intestine of the mouse, pancreatic bud, laser welding and lung cell spheroid.

characteristics of the real stacks of images used in the experiments.

set	number of images	image size	pre-processing	origin
FLY	32	$1280\times 1024$	none	BIG EPFL [182]
INTESTINE	20	$1996\times 1450$	none	BIG EPFL [182, 186]
PANCREAS	17	$400\times 400$	extracted from a video	BIG EPFL [186]
LASER	13	$1024\times 768$	none	BIG EPFL
LUNG	26	$611\times 531$	cropped from original larger images	original images personally acquired

**Tab. 5.1:** Characteristics of the real stacks of images used in the experiments.

## 5.6 Experimental results

To assess the effectiveness of the proposed approach we used both synthetic and real stacks of images. The synthetic stacks are provided with ground truth,

that is the original image used to obtain the defocused ones. Accordingly, to evaluate as the output of the different methods differ from the ground truth it is possible to use standard metrics like  $UQI$ ,  $SNR$  and  $MSE$ . Nevertheless, to evaluate the output of the different methods using also real sets of images we need a metric able to rank the methods without requiring a reference ground truth. To this purpose, first we validated a metric able to rank the output of the methods as the standard  $UQI$  does, here without requiring a reference ground truth, then we evaluated the output of the different methods using the new validated metric and the different sets of real images available.

### 5.6.1 Experiments with the synthetic stacks

In order to compare the performance of DOFE with that of state-of-the-art methods (reported in Sect. 5.2), the metrics  $UQI$ ,  $SNR$  and  $MSE$  were evaluated (Tab. 5.2) using the different final composite images and the related

METRIC, SET	DOFE	SF	DFE	CWBM	MBM	CUR
$UQI$ , D13	0.9945	0.9943	0.9676	0.9938	0.9915	0.9925
$UQI$ , D22	0.9895	0.9892	0.9548	0.9889	0.9837	0.9843
$UQI$ , D23	0.9974	0.9972	0.9691	0.9970	0.9961	0.9964
$UQI$ , D61	0.9965	0.9963	0.9663	0.9958	0.9949	0.9953
$UQI$ , D112	0.9922	0.9919	0.9433	0.9911	0.9885	0.9891
$SNR$ , D13	26.52	26.32	18.95	26.03	24.68	25.23
$SNR$ , D22	24.49	24.39	18.10	24.27	22.71	22.89
$SNR$ , D23	29.19	28.89	18.71	28.63	27.46	27.83
$SNR$ , D61	29.75	29.47	19.90	28.98	28.11	28.44
$SNR$ , D112	29.09	28.94	20.35	28.58	27.50	27.75
$MSE$ , D13	51	53	291	57	78	69
$MSE$ , D22	95	98	415	100	144	138
$MSE$ , D23	22	23	244	25	33	30
$MSE$ , D61	16	17	153	19	23	21
$MSE$ , D112	38	39	282	42	54	51
RANKING	1 <sup>st</sup>	2 <sup>nd</sup>	6 <sup>th</sup>	3 <sup>rd</sup>	5 <sup>th</sup>	4 <sup>th</sup>

**Tab. 5.2:** Methods ranking using synthetic stacks.  $UQI$ ,  $SNR$  and  $MSE$  values achieved by comparing the ground truths with the final composite images obtained with the six methods tested are reported. In particular, five different synthetic stacks were built using Brodatz textures D13, D22, D23, D61 and D112. The same ranking was obtained for each stack and metric, as shown in the bottom row of the table.

ground truths (i.e., the Brodatz textures used to build the stacks). The best

values for all the images, that is the highest  $UQI$  and  $SNR$  and the lowest  $MSE$ , were always achieved by DOFE. Looking at Tab. 5.2, last row, it is worth noting that for each stack the ranking (from the best to the worst method) was the same for all the metrics. Although achieving the same ranking for *all* three metrics was not expected, it often occurs [108, 22, 107] and in such cases the obtained ranking of methods can be considered both meaningful and reliable due to the number of consensus achieved. Analyzing the data in Tab. 5.2, it can be seen that the best numerical values, achieved by DOFE, were always followed by the ones achieved by SF, that is the method most similar to DOFE. In addition, all the methods generally yielded comparable results, except DFF whose numerical results were by far the worst, as the visual analysis confirms (Fig. 5.6). As matter of fact, what can be easily detected in extended depth-

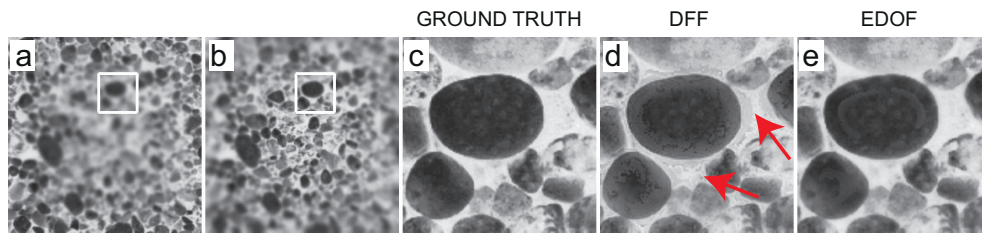


**Fig. 5.6:** Visual analysis of synthetic images. (a) and (b): unfocused slices of the stack artificially built using the Brodatz texture image D23. (c): zoomed detail of the ground truth image D23 related to the ROI pointed out by the white square in (a) and (b). (d) and (e): same details as (c), but from images obtained using DFF and DOFE, respectively.

of-focus applications are visually poor results, such as a final composite image containing manifest noise, Airy discs or artifacts produced, for example, by diffraction and aliasing [185] (Fig. 5.6).

### 5.6.2 Analysis of metrics for real stacks

There is no reference metric to compare the results of the different extended depth-of-focus methods in real cases, where logically the stacks are not provided of ground truth. In particular, the different versions of  $UQIN$  are commonly used in extended depth-of-focus applications, but their performance are not completely clear. Accordingly, it was decided to use the synthetic stacks

(provided with ground truth) to evaluate the three different versions proposed for  $UQIN$  in order to analyze the performance of the metrics and, in particular, to compare thoroughly  $UQIN$  and  $UQI$ . Tab. 5.3 reports the ranking of

METRIC, SET	DOFE	SF	DFE	CWBM	MBM	CUR
$UQIN$ , D13	4 <sup>th</sup>	5 <sup>th</sup>	6 <sup>th</sup>	3 <sup>rd</sup>	1 <sup>st</sup>	2 <sup>nd</sup>
$UQIN$ , D22	4 <sup>th</sup>	3 <sup>rd</sup>	6 <sup>th</sup>	5 <sup>th</sup>	1 <sup>st</sup>	2 <sup>nd</sup>
$UQIN$ , D23	4 <sup>th</sup>	5 <sup>th</sup>	6 <sup>th</sup>	3 <sup>rd</sup>	1 <sup>st</sup>	2 <sup>nd</sup>
$UQIN$ , D61	3 <sup>rd</sup>	4 <sup>th</sup>	6 <sup>th</sup>	5 <sup>th</sup>	1 <sup>st</sup>	2 <sup>nd</sup>
$UQIN$ , D112	3 <sup>rd</sup>	4 <sup>th</sup>	6 <sup>th</sup>	5 <sup>th</sup>	1 <sup>st</sup>	2 <sup>nd</sup>
$UQIN2$ , D13	5 <sup>th</sup>	3 <sup>rd</sup>	6 <sup>th</sup>	4 <sup>th</sup>	1 <sup>st</sup>	2 <sup>nd</sup>
$UQIN2$ , D22	4 <sup>th</sup>	3 <sup>rd</sup>	6 <sup>th</sup>	5 <sup>th</sup>	1 <sup>st</sup>	2 <sup>nd</sup>
$UQIN2$ , D23	5 <sup>th</sup>	4 <sup>th</sup>	6 <sup>th</sup>	3 <sup>rd</sup>	1 <sup>st</sup>	2 <sup>nd</sup>
$UQIN2$ , D61	4 <sup>th</sup>	3 <sup>rd</sup>	6 <sup>th</sup>	5 <sup>th</sup>	1 <sup>st</sup>	2 <sup>nd</sup>
$UQIN2$ , D112	4 <sup>th</sup>	3 <sup>rd</sup>	6 <sup>th</sup>	5 <sup>th</sup>	1 <sup>st</sup>	2 <sup>nd</sup>
$UQIN3$ , D13	4 <sup>th</sup>	3 <sup>rd</sup>	6 <sup>th</sup>	5 <sup>th</sup>	1 <sup>st</sup>	2 <sup>nd</sup>
$UQIN3$ , D22	4 <sup>th</sup>	3 <sup>rd</sup>	6 <sup>th</sup>	5 <sup>th</sup>	1 <sup>st</sup>	2 <sup>nd</sup>
$UQIN3$ , D23	4 <sup>th</sup>	3 <sup>rd</sup>	6 <sup>th</sup>	5 <sup>th</sup>	1 <sup>st</sup>	2 <sup>nd</sup>
$UQIN3$ , D61	3 <sup>rd</sup>	4 <sup>th</sup>	6 <sup>th</sup>	5 <sup>th</sup>	1 <sup>st</sup>	2 <sup>nd</sup>
$UQIN3$ , D112	3 <sup>rd</sup>	4 <sup>th</sup>	6 <sup>th</sup>	5 <sup>th</sup>	1 <sup>st</sup>	2 <sup>nd</sup>

**Tab. 5.3:** Rankings achieved using the metrics  $UQIN$ ,  $UQIN2$  and  $UQIN3$ .  $UQIN$ ,  $UQIN2$  and  $UQIN3$  ranking values were achieved by comparing the images of the five synthetic stacks built using Brodatz textures with the different final composite images created by the six different methods tested. As the parameters required to compute the third version of  $UQIN$ ,  $UQIN3$ , we used a sliding windows of  $9 \times 9$  pixels and  $\beta=1$ . It is worthy of note that the ranking achieved was always different from that previously obtained using the standard  $UQI$  (reported in the bottom row of Tab. 5.2).

methods according to the  $UQIN$  values obtained using a sliding windows of  $9 \times 9$  pixels and  $\beta=1$  for the third formula of  $UQIN$  (see Eq. 5.12). The same ranking achieved with the standard  $UQI$  (reported in the last row of Tab. 5.2) was never obtained, showing that  $UQIN$  and  $UQI$  evaluate images differently, in contrast to what was expected as  $UQIN$  is considered as an  $UQI$  extension. This was further confirmed by the last experiment carried out where we compared the performance of  $UQIN$  and  $UQI$  by replacing  $f$  (the output in-focus images) with the respective ground truth images in Eqs. 5.8 5.10 5.12. Surprisingly, the results obtained were not the highest as expected. It is worthy of note that the worst results were always obtained with DFF.

To overcome the lack of a suitable approach to rank methods when working with real stacks, we propose a new approach based on the metric previously defined as  $AUQI$ . As described in Sect. 5.6.1, in extended depth-of-focus ap-

plications it is fairly easy to visually judge whether a method yields a bad result. Starting from this assumption, we developed an effective approach to estimate the ranking of extended depth-of-focus methods, with the same evaluation performance as the standard  $UQI$  and without the need of a reference ground truth. First, on the basis of the visual quality of the final images  $f$ , we discarded the methods clearly yielding poor results. It is worth noting that to visually discard in advance the methods obtaining poor results is fundamental to avoid errors in the evaluation of the methods' rank. Second,  $AUQI$  was computed between  $f$  (one for each method not previously discarded) and the  $N$  slices  $s_n$  of the original stack. Finally, the methods' rank was obtained by attributing the lowest  $AUQI$  value to the best method, the second worst  $AUQI$  to the second best method, and so on (among those not previously discarded by visual analysis).

Tab. 5.4 shows the  $AUQI$  values and the final ranking obtained using the syn-

METRIC, SET	DOFE	SF	DFE	CWBM	MBM	CUR
$AUQI$ , D13	0.8822	0.8823	//	0.8831	0.8917	0.8897
$AUQI$ , D22	0.6538	0.6541	//	0.6543	0.6688	0.6674
$AUQI$ , D23	0.9220	0.9223	//	0.9230	0.9274	0.9270
$AUQI$ , D61	0.9306	0.9308	//	0.9315	0.9360	0.9354
$AUQI$ , D112	0.8250	0.8253	//	0.8258	0.8363	0.8353
RANKING	1 <sup>st</sup>	2 <sup>nd</sup>	//	3 <sup>rd</sup>	5 <sup>th</sup>	4 <sup>th</sup>

**Tab. 5.4:**  $AUQI$  from the synthetic stacks.  $AUQI$  values achieved by comparing the images of the five synthetic stacks built using Brodatz textures with the in-focus images obtained by the six methods tested. Values relating to the DFE method are not reported as they were visually poor and discarded beforehand. The bottom row reports the method ranking for all the stacks. As one can see, it corresponds to that achieved with the standard  $UQI$  (last row of Tab. 5.2).

thetic stacks, only discarding the DFE method which always yielded a visually poor result. In particular, the ranking obtained was the same for all the stacks and equivalent to the one achieved using the standard  $UQI$ . Furthermore, using the reference ground truths as in-focus images and calculating the  $AUQI$ , the obtained values were always lower than the ones reported in Tab. 5.4, as expected, this representing a further proof of the reliability of  $AUQI$ . It is worth noting that a crucial step of this ranking approach is the elimination of methods yielding for instance visually poor results. Without this step, some errors in ranking estimation may occur: a final composite image containing noise or artifacts could be very different from the original blurred slices of

the stacks. Consequently, computing the  $AUQI$  between such an image and the stack of the slices could lead to a very low value. Analyzing the data in Tab. 5.4, once again can be observed that the best values (i.e., lowest  $AUQI$ ) for all the stacks, achieved by DOFE, were very similar to those of SF (second ranking for all the stacks).

### 5.6.3 Experiments with real stacks

As stated previously, fully in-focus ground truth images are not available for the stacks of real slices. Consequently, the quality of the output image of extended depth-of-focus methods cannot be measured simply by exploiting the standard  $UQI$  (or  $SNR$  or  $MSE$ ). The evaluation approach conceived and discussed in Sect. 5.6.2 (based on the  $AUQI$  evaluation and preceded by a fundamental visual analysis) showed that for synthetic stacks it is possible to achieve the same final ranking obtained with  $UQI$ . This prompted us to use our approach to evaluate extended depth-of-focus methods in real world cases. It is worthy of note that, unlike the synthetic stacks, stacks of real slices (acquired with different hardware - microscopes and cameras - and a different  $z$ -step between the slices) may also yield different ranking of methods for each stack analyzed. Furthermore, the synthetic stacks are simply an approximation of the real world where, for example, the PSF is space-variant in the three dimensions and depends on several parameters such as the spectrum of the light source. Or else, the distance between coverslip and the surface of the object [210] and out-of-focus areas that are not correctly modeled by a Gaussian filter. In the light of such considerations, using the real stacks could result in some methods ranking different from that estimated using the synthetic stacks.

Fig. 5.7 shows the final composite images obtained using the six methods tested on the five stacks of real slices. Again, through visual analysis it can be seen that for each stack DFF always yielded poor results. Tab. 5.5 reports the  $AUQI$  values and Tab. 5.6 shows the ranking obtained by simply discarding the images pertaining to DFF. As expected, method ranking was dependent on image set, this yielding rankings different from those achieved with the synthetic stacks. The best results were always achieved by SF and once by DOFE.

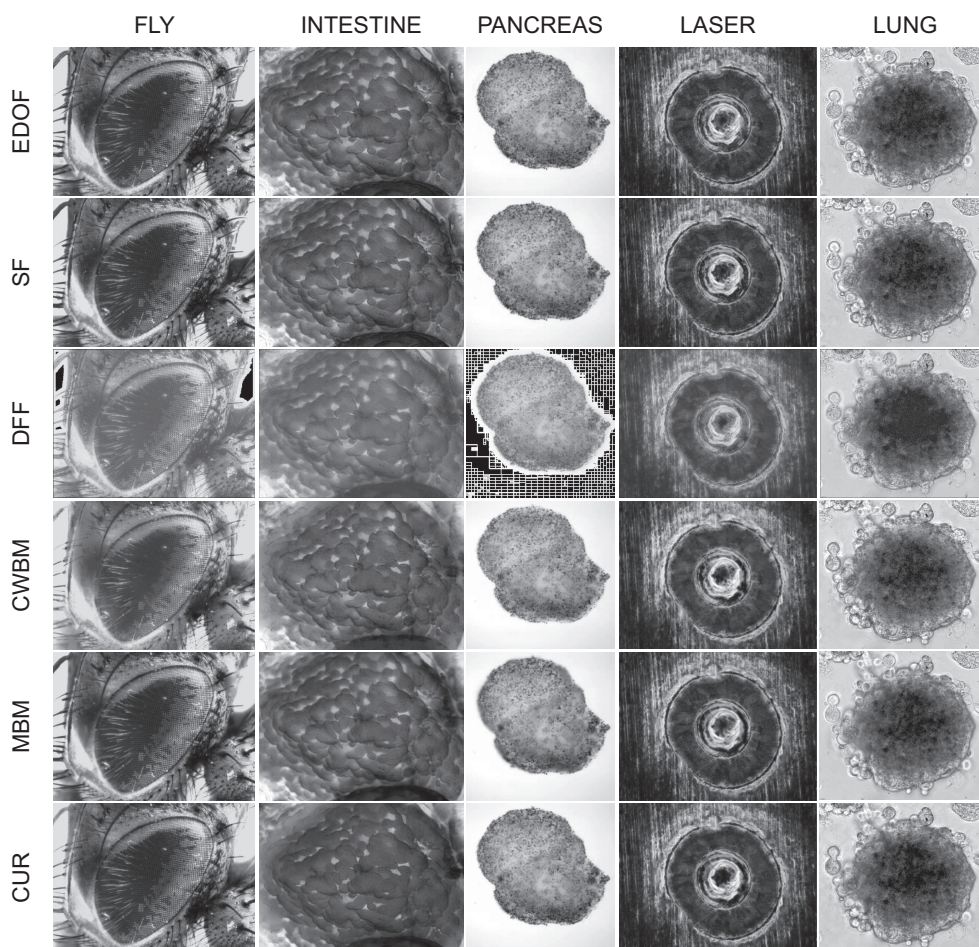


**Fig. 5.7:** Final in-focus images from real stacks. Final in-focus images obtained from the stacks of real slices using all six software tested. Left to right columns show images relating to: eye of the fly, intestine of the mouse, pancreatic bud, laser welding and lung cell spheroids. The final composite images obtained using DOFE are reported from the first to the last rows, for each stack: SF, DFF, CWBM, MBM and CUR. Simple visual analysis is sufficient to see that the worst results were always obtained using DFF (images in the third row).

## 5.7 Conclusion and future work

### 5.7.1 Conclusion

Extending the depth of focus is a well-known need in microscopy, where it is impossible to acquire a single completely in-focus image of objects char-

METRIC, SET	DOFE	SF	DFE	CWBM	MBM	CUR
<i>AUQI</i> , FLY	0.9021	<b>0.8996</b>	//	0.9062	0.9086	0.9096
<i>AUQI</i> , INTESTINE	0.8286	<b>0.8278</b>	//	0.8542	0.8466	0.8393
<i>AUQI</i> , PANCREAS	<b>0.9410</b>	0.9413	//	0.9557	0.9561	0.9495
<i>AUQI</i> , LASER	0.9278	<b>0.9271</b>	//	0.9306	0.9422	0.9413
<i>AUQI</i> , LUNG	0.8557	<b>0.8524</b>	//	0.8947	0.8692	0.8904

**Tab. 5.5:** *AUQI* from the real stacks. *AUQI* values achieved by comparing the images of the five real stacks with the composite images obtained with the six methods tested. The values relating to the DFE method are not reported as they were visually poor and discarded beforehand.

METRIC, SET	DOFE	SF	DFE	CWBM	MBM	CUR
<i>AUQI</i> , FLY	2 <sup>nd</sup>	1 <sup>st</sup>	//	3 <sup>rd</sup>	4 <sup>th</sup>	5 <sup>th</sup>
<i>AUQI</i> , INTESTINE	2 <sup>nd</sup>	1 <sup>st</sup>	//	5 <sup>th</sup>	4 <sup>th</sup>	3 <sup>rd</sup>
<i>AUQI</i> , PANCREAS	1 <sup>st</sup>	2 <sup>nd</sup>	//	4 <sup>th</sup>	5 <sup>th</sup>	3 <sup>rd</sup>
<i>AUQI</i> , LASER	2 <sup>nd</sup>	1 <sup>st</sup>	//	3 <sup>rd</sup>	5 <sup>th</sup>	4 <sup>th</sup>
<i>AUQI</i> , LUNG	2 <sup>nd</sup>	1 <sup>st</sup>	//	5 <sup>th</sup>	3 <sup>rd</sup>	4 <sup>th</sup>

**Tab. 5.6:** Method rankings using real stacks. This table reports the method rankings based on the *AUQI* values of Tab. 5.5. The values relating to the DFE were discarded beforehand as they were visually poor. It is worthy of note that the first two positions were always achieved by DOFE and by SF.

acterized by a wide depth, such as multi-cell spheroids. Although numerous methods have been proposed in literature to fulfill this need, the frequent lack of a reference ground truth and of a validated approach makes it difficult to define the method that can yield the best results in real applications. However, the wavelet-based methods are widely used and often considered better than those working in the spatial domain. Despite this, simplicity and ease-of-use of the spatial-based methods make them very attractive. Starting from this consideration, we designed a new spatial-based method where in-focus regions of the images are detected by performing a simple derivative step and the final composite image is built using a maximum rule and a number of filtering stages. We then selected five widely used state-of-the-art software and compared their performance with that achievable by DOFE. The experiments performed using synthetic stacks of slices, with ground truth, showed that DOFE performs better than the state-of-the-art ones. In order to extend the assessment to real cases, we first focused our attention on some metrics proposed in literature as *UQI* extensions, finding out that they are not capable of ranking the

method in the same way as the standard *UQI* does. Then, we validated a new approach to evaluate extended depth-of-focus methods which do not require a ground truth and exploit all the  $N$  images of the stack. The experiments showed that the rankings obtained on the basis of our new approach were the same achieved by the standard *UQI*. This confirms that our approach can be used to evaluate extended depth-of-focus methods in real world cases. We thus decided to use this new approach to see how DOFE works in real cases. The results achieved using real stacks proved that, despite its simplicity, the performance achieved by DOFE is at the very least comparable with those of the state-of-the-art methods. Also, it shows that spatial-based approaches may perform better than, or at least comparably to, wavelet-based methods, thus partially disproving what is reported in a significant part of literature.

The method implementation and all the metrics used in the tests are available on request [11].

The content of this chapter was partly published in [211, 212].

### 5.7.2 Future work

Several open issues still remain. First, as far as colour processing is concerned, there are no validated approaches in literature to assess which is the best extended depth-of-focus method. One working hypothesis could be to transform final colour images into grey levels, but this would lead to an information loss, whose consequences should be assessed. A second strategy could be converting the images in the *HSI* (Hue Saturation Intensity) colour space and using the *I* channel instead of the grey levels. Again, this represents an information loss, but the *I* channel could be a more reliable representative of the original colour images. Finally, the extended depth-of-focus algorithm implemented in this thesis should be improved in terms of speed performance and memory saving.

## 5.8 Acknowledgments

I would like to thank Dr. Daniel Sage (Biomedical Imaging Group, EPFL, Switzerland) for providing some of the stacks of slices used in this chapter.

## 5.9 Copyright permission

I declare that for using the material previously published in [211] I obtained the rights permission by co-authors and by the Publisher (the license details are reported in Tab. 5.7).

Licensee	Filippo Piccinini
License Date	Feb 20, 2013
License Number	3092930003758
Licensed Content Publisher	John Wiley and Sons
Licensed Content Publication	Microscopy Research and Technique
Licensed Content Title	Extended depth of focus in optical microscopy: assessment of existing methods and a new proposal
Licensed Content Date	Sep 13, 2012
Licensed Portion	Full article
Type Of Use	Dissertation/Thesis
Order Reference	MRTFOCUS20130220

**Tab. 5.7:** License details by Microscopy Research and Technique.

# Chapter 6

## Conclusion

In this thesis, we focused our attention on the microscope, the main instrument of measurement of the infinite small. In particular, we have considered common issues regarding the widefield microscope, the most common one in the biological laboratories. This instrument is the basic device for the daily work of thousands of biologists over the world. Nowadays, the different potential analyses carried out *via* microscope are truly countless. Furthermore, many current limitations could be solved simply by a better interaction between biologists and engineers. As a biomedical engineer working along side biologists I have had the opportunity to see the daily problems that my colleagues have to face using the microscope. This has been the reason that stirred up my work aiming at developing effective solutions to meet three main requirements regarding the usage of widefield microscopes:

- obtaining images that can be compared even if acquired at different times
- increasing the field of view of the camera to acquire high-resolution images of the whole sample
- visualizing a single image everywhere in-focus, even of deep objects

The main goal of the thesis was to deeply analyze the very early cause of the appearance changing of images, that is the vignetting problem, in both light and fluorescent microscopy. The vignetting has been known in literature for decades, but it was never strongly deepened in microscopy. “Flattening”

the image illumination is an early process and fixing the vignetting problem would be beneficial to most of the everyday analyses carried out through using imaging techniques. In this thesis, sample-oriented solutions for both light and fluorescent microscopy are presented to estimate the intensity curvature to be corrected directly from the images, even considering non-linear effects, never faced before. In particular, in the method proposed to correct brightfield and phase-contrast images, agreeing that most of the vignetting effects have a linear behavior, the images are simply flattened according to the curvature estimated. A similar approach was proposed also for fluorescent images where, however, non-linear effects could be appraisable making the image curvature depending on intensity grey levels. Accordingly, we proposed a second solution where an ensemble of vignetting curves for different grey levels are estimated. In particular, this represents the first method to correct the images in fluorescence microscopy even considering the non-linear behavior of the vignetting. The obtained results proved that the proposed methods perform better than the approaches typically used in literature. Also, it is worth noticing that we proved that in fluorescence using the gold standard (i.e., calibration slides) could even worsen the signal distribution, without user's awareness. This is a very important finding, considering the number of works in literature proposing solutions employing the gold standard.

The second common issue we tackled is due to the limited field of view of the microscope's camera, that prevents from acquiring a single high-detailed image representative of the whole sample. To overcome this limitation, we developed a mosaicing technique for stitching images and building on-line large mosaics, having at least the same pixel resolution of the source images. At the beginning, the mosaicing software was conceived in this thesis just as a tool for testing and comparing different vignetting corrections, registration approaches and warping models. That is, the focus was not the improvement of the state of the art. Rather, we proposed a practical working solution to obtain mosaics with widefield microscopes. Afterwards, we have implemented different transformation models proving that, contrarily to what is often claimed, the most suitable model to create mosaics of images with a widefield microscope is the projective model and not the translative one.

Once studied how to normalize the images and to extend the planar camera's field of view, as the third topic we dealt with the extension of the field of view on the  $z$ -dimension. Although numerous methods have been proposed

in literature to extend the depth of focus of the microscopes, the lack of a validated approach makes it difficult to define the method that can yield the best result for a given application. Yet more in the real world, where reference images to be compared do not exist. After studying the different existing approaches, we developed a method merging the best concepts. Our main contributions in this field can be summarized as follows. First, we validated a metric to compare the outcome of the different methods without requiring a reference image. Second, we developed an effective solution to extend the camera's depth of focus, obtaining single images completely in-focus, even of very deep objects.

Finally, as far as the fluorescence microscopy is concerned, we also dealt with photo-bleaching degradation, arising from multiple acquisition of same field of view, proposing a solution for its characterization and an effective approach to compensate its effects.

For the sake of clarity, running the risk of redundancy, we summarize the main achievements of this thesis as follows.

Scientific:

- the first study regarding the non-linear vignetting correction in microscopy
- to have proved that the projective model, rather than the translative one, is the most suitable to create mosaics of images also with manual widefield microscopes
- a simple yet effective approach to fill in the gaps in the lack of a metric to compare the results of different extended depth-of-focus methods without requiring a reference image

Technical:

- methods and tools to achieve vignetting free images and to compare different vignetting correction approaches
- a method, and its implementation, to achieve a mosaic of microscopic images acquired by moving the holder manually

- implementation of a new effective method to achieve one in-focus image of deep objects, starting from a sequence of images manually acquired at different focus planes

Technological:

- fixed an early processing problem, such as vignetting, this effecting the overall microscope calibration procedures
- extended *via* software the field-of-view of the microscope's camera
- extended *via* software the microscope depth of focus to allow users acquiring sharp images also of deep objects

In particular, the extended depth-of-focus tool and the algorithm regarding the vignetting correction for every light microscope are freely available directly from the websites of the scientific journals where we part submitted our work.

To conclude, it is often stated that the best researches are those closing existing problems, opening new research fields at the same time. Although we do not pretend to have definitively closed the problem of vignetting in microscopy, this thesis starts the studies regarding the non-linearities of vignetting in both light and fluorescence microscopy. Nevertheless, results, software tools and publications born thanks to the work summarized in this thesis have enriched the state of the art. Microscopists and biologists have now at their disposal methods and techniques helping them to better understand the outcome of their researches and, desirably, to extend them with new inquiry, by performing novel experiments thanks to a better exploitation of their microscope.

# Appendix

In the following sections the details of widespread image processing algorithms are reported. Due to the general applicability of these algorithms in many different contexts, it was preferred to create a specific appendix instead of providing the chosen implementation details inside the different Chapters of the thesis.

## Phase correlation

The Phase Correlation algorithm [213] in its original formulation is based on the Fourier Shift Theorem. It states that given a pair of images  $I(x, y)$  and  $J(x, y)$  of the same size, related by a global translation (Eq. a):

$$I(x, y) = J(x - \Delta x, y - \Delta y) \quad (\text{a})$$

their Discrete Fourier Transforms  $F_I(u, v)$ ,  $F_J(u, v)$  obey to Eq. b:

$$F_I(u, v) = F_J(u, v) \cdot e^{-2\pi i(u\Delta x + v\Delta y)} \quad (\text{b})$$

The Normalized Cross Power Spectrum  $R(u, v)$  can be expressed factoring out the phase difference as reported in Eq. c (the symbol \* represents the complex conjugate):

$$R(u, v) = \frac{F_J(u, v) \cdot F_I^*(u, v)}{|F_J \cdot F_I^*|} = \frac{F_J(u, v) \cdot F_J^*(u, v) \cdot e^{+2\pi i(u\Delta x + v\Delta y)}}{|F_J \cdot F_J^*|} = e^{+2\pi i(u\Delta x + v\Delta y)} \quad (\text{c})$$

The magnitude of an imaginary exponential is always one, and the phase of  $F_J \cdot F_J^*$  is always zero. The Correlation Surface  $CS(x, y)$  can be thus obtained

applying the Inverse Fourier Transform (Eq. d):

$$CS(x, y) = F^{-1}(R(u, v)) = F^{-1}(e^{+2\pi i(u\Delta x + v\Delta y)}) = \delta(x + \Delta x, y + \Delta y) \quad (d)$$

The inverse Fourier transform of a complex exponential is a Kronecker delta  $\delta$  (i.e. a single peak). Accordingly, the global translation vector  $(\Delta x, \Delta y)$  can be estimated as the  $x$ - $y$  position of the maximum peak in  $CS(x, y)$  (Eq. e):

$$(\Delta x, \Delta y) = \operatorname{argmax}_{(x,y)} CS(x, y) \quad (e)$$

Practically speaking, in the Phase Correlation algorithm the steps to find the best match between a pair of images are the following [176]:

1. converting to grey levels the two input images  $I(x, y)$  and  $J(x, y)$ , having the same  $M \times N$  (rows  $\times$  columns) size
2. computing their Discrete Fourier Transform, resulting in  $F_I(u, v)$  and  $F_J(u, v)$ , two complex  $M \times N$  matrices
3. computing the Normalized Cross Power Spectrum  $R(u, v)$ , forming the cross power spectrum  $F_I F_J^*$  and dividing it by its modulus
4. computing the Correlation  $M \times N$  Surface  $CS(x, y)$  as Inverse Fourier Transform of the phase difference matrix
5. defining the  $(x, y)$  position of the highest peak in  $CS$  as the  $x$ - $y$  translative shift between the images  $I(x, y)$  and  $J(x, y)$

The output of the Phase Correlation algorithm in his basic version is the global translation components at pixel level accuracy between two input images of the same size. It has been extended also to image rotation [214] and small changes in scale [215], and to subpixel level accuracy [216]. It is quite robust to additive noise, blurring artefacts and changes in lighting conditions (thanks to the normalization in Eq. c). Furthermore, the algorithm has been extended to work also with the contours of the images only to be even more robust and faster [168]. However, the presence of additional geometric distortions, noise and not negligible modifications in the image content can introduce further spurious incoherent peaks in the Correlation Surface, that can even return

wrong results in the estimation of the motion parameters.

In order to handle the presence of multiple peaks, in our Phase Correlation implementation (Matlab code distributable upon request [11]) several additional steps have been implemented:

- every input image is pre-processed subtracting its minimum value. This works to enhance the Signal to Noise Ratio
- the Correlation Surface  $CS(x, y)$  has been denoised setting to 0 all the values lower than the mean value plus 3 times the standard deviation ( $\sigma$ )
- for every region containing values different to 0 only the maximum value is kept. All the other values are set to 0
- only at maximum the 3 higher peaks are analyzed
- a score based on the mean of the fourth-power differences (cost function) on the overlapping areas of the two input images is used to decree who is the best peak (the one with the minimum score), also checking the wrap around of the peak's coordinates
- all the peaks (or their wrap around) that generate a shift higher of the 95% are discarded. This is a control on the maximum shift checked (in both the  $x$  and  $y$  directions) between the two input images

Here, we want to stress that using as the cost function the mean of the fourth-power differences works as a pivot rule in case of input images with a lot of background and few objects: the fourth-power of the differences increases the separability between signal and noise, making the thresholding stage easier. Even though being quite heuristic, this strategy has proved to be quite robust even with images decimated by a factor of two, this being important to speed up the algorithm.

## RANSAC

RANSAC is an abbreviation for “RANdom SAmple by Consensus”. It is a *robust* iterative method to estimate parameters of a mathematical predetermined model using a set of noisy observed data containing also outliers. The meaning of robustness is precisely meant in the sense of good tolerance to *completely erroneous observations* possibly present in the collection of experimental data. In particular, RANSAC is a non-deterministic algorithm that produces a reasonable result only with a certain probability, increasing with the number of iterations. The algorithm was first published by Fischler and Bolles at Stanford Research Institute International in 1981 [170].

The algorithm finds application in a wide spectrum of data analyses related to the estimation of model’s parameters in the field of artificial vision as the feature matching, alignment of images, etc. In particular, we exploited RANSAC to estimate the parameters of the fundamental matrix using a set of noisy data (corresponding features between two different views of the same scene). A basic assumption is that the data consists of “inliers”, i.e., data whose distribution can be explained by some set of model parameters, and “outliers” which are data that do not fit the model. In addition to this, the data contains noise. The outliers can come, e.g., from extreme values of the noise or from erroneous measurements or incorrect hypotheses about the interpretation of data. RANSAC assumes that, given a (usually small) set of inliers, there exists a procedure which can estimate the parameters of a model that optimally explains or fits this data. The algorithm is simple and powerful, it operates in the same time by eliminating outliers while estimating the parameters of the predesigned model. It works iteratively until reaching a termination condition according to the following steps:

- Step 1: sampling of experimental data. The minimum subset of needed observations is uniformly and randomly extracted from the set of available samples. Each observation has the same probability of being selected (the concept of uniform sampling) and the number of needed observations depends on the Degrees Of Freedom (DOF) of the predesigned model. For instance, searching a plane in the space using a set of points requires at least the selection of three points because three are the DOF necessary to uniquely describe a plane in the space. To select a larger

number of observations involves inherent inefficiency of the algorithm, because the likelihood of extracting all inlier samples decreases as the number increases.

- Step 2: parameters estimation. Estimation of the parameters's values related to the DOF of the predesigned model using only the minimum subset of needed data (selected according to the previous step).
- Step 3: evaluation of the estimated parameters. The quality of the estimated parameters's values is evaluated using the whole set of available data. Typically a cost function is used as a metric for comparison of different estimations of the parameters of the predesigned model. A cost function widely used is the count of the number of the experimental data agreeing with the estimated parameters, barring a tolerance threshold. The set of estimated parameters that collects the greater consensus is considered the one most appropriate for the predesigned model.

In particular, these are three fundamental parameters of the RANSAC algorithm:

- Tolerance threshold of the cost function. It determines whether an individual input point supports the computed model (Step 3).
- Percentage of agreement. It is related to the discrimination of a valid set of parameters estimated for the predesigned model. It represents the percentage of consensus achieved when the model is evaluated on the whole data set. It can be used as termination criterion.
- Iteration count. It is the maximum number of iterations before the model with greatest support is finally chosen. It represents a possible termination criterion of the algorithm.

Finally, when the set of estimated parameters achieving the higher consensus is decreed, the final set of parameters is estimated using not only the minimum number of needed observations, but all the input data considered inliers for the last set of parameters estimated. This to obtain a more robust parameter estimation of the predesigned model.

In our experiments, as input data we have  $N$  pairs of corner correspondences

$(x_i^n, x_j^n)$ ,  $n = 1 \dots N$ , between two views ( $X_i$  and  $X_j$ ) of the same scene. RANSAC is exploited to estimate the parameters of the warping model  $H$  (translative, affine or projective) between the two views. As the cost function we use the distance between of the original data  $x_i^n$  and its reprojected version  $H \times x_j^n$ . The tolerance threshold, to consider a pair of corners inlier of the computed model parameters, is set to 2 pixels. The number of inliers for every estimated set of parameters is used as coefficient of agreement. We fixed 1500 as the maximum number of sets of computed parameters, since it has been experimentally determined as being a fair value representing a good trade-off between computational cost and accuracy of the model.

# List of Figures

1.1	Widefield microscope . . . . .	1
1.2	Microscopes taxonomy . . . . .	2
1.3	Microscope and measure . . . . .	3
1.4	Light spectrum . . . . .	4
2.1	Vignetting effect . . . . .	9
2.2	Vignetting sources . . . . .	12
2.3	Background segmentation . . . . .	20
2.4	Algorithm pipeline . . . . .	21
2.5	Automatic and manual background segmentation . . . . .	26
2.6	Depth dimension of mesenchymal stem cells . . . . .	27
2.7	Vignetting, confluence and number of images . . . . .	29
2.8	Vignetting functions shapes . . . . .	31
2.9	Flat-field correction on single images . . . . .	34
2.10	Component images and overlapped parts of the mosaic . . . . .	37
2.11	Flat-field correction on mosaics . . . . .	39
3.1	Vignetting effect in fluorescence microscopy . . . . .	47
3.2	Vignetting effect . . . . .	48
3.3	CellProfiler Correct Illumination modules . . . . .	55
3.4	Model of background . . . . .	60
3.5	Model of foreground . . . . .	61
3.6	Object's intensity depending on the position . . . . .	63
3.7	Non-linear flat-field correction: acquisition strategy . . . . .	63
3.8	Flow chart of the non-linear flat-field correction method . . . . .	64
3.9	Modelling of the photobleaching decay . . . . .	65
3.10	Disadvantage of high intensity gradient pixels . . . . .	66
3.11	Foreground masks . . . . .	69
3.12	Median foreground signal distributions . . . . .	70

3.13	Overlapping image pair . . . . .	71
3.14	Histogram of the sign differences in the image overlapping . . . . .	72
3.15	Overlapping areas where <i>FCSM</i> performed well . . . . .	75
3.16	Histogram score of nLCBM . . . . .	77
4.1	Mosaic of images . . . . .	81
4.2	Curvature of the image's intensity . . . . .	92
4.3	Mosaics built with and without vignetting correction . . . . .	92
4.4	Shi-Tomasi features . . . . .	94
4.5	Correspondence between corner points using LKT . . . . .	95
4.6	Global transformation models . . . . .	100
4.7	The system used in our experiments . . . . .	103
4.8	Images of living mesenchymal stem cells . . . . .	104
4.9	Images of bone tissue . . . . .	104
4.10	Mosaic building path of the SC30 images . . . . .	105
4.11	Mosaic building path of the BT40 images . . . . .	106
4.12	RMSE evaluation approach . . . . .	107
4.13	Mosaic SC30 without flat-field correction . . . . .	109
4.14	Mosaic SC30 with flat-field correction . . . . .	110
4.15	Mosaic SC30 according to the F2F registration . . . . .	111
4.16	Mosaic SC30 according to the F2M registration . . . . .	112
4.17	Comparison between two details of mosaic SC30 . . . . .	112
4.18	Mosaic BT40 without flat-field correction . . . . .	115
4.19	Mosaic BT40 with flat-field correction . . . . .	116
4.20	Comparison between two details of mosaic BT40 . . . . .	122
4.21	Frequency of intensity levels of the SC mosaic . . . . .	123
4.22	Frequency of intensity levels of the BT mosaic . . . . .	123
5.1	Depth of focus . . . . .	125
5.2	Lung cell spheroid (bronchosphere) . . . . .	127
5.3	Brodatz textures . . . . .	137
5.4	Slices from synthetic stacks . . . . .	138
5.5	Slices from real stacks . . . . .	139
5.6	Visual analysis of synthetic images . . . . .	141
5.7	Final in-focus images from real stacks . . . . .	145

# List of Tables

2.1	Threshold values for the background segmentation . . . . .	26
2.2	Comparison of vignetting functions . . . . .	32
2.3	Flat-field correction on single images . . . . .	34
2.4	Quality of mosaics . . . . .	40
2.5	License details by Journal of Microscopy. . . . .	45
3.1	Flatness and std of the foreground distribution . . . . .	68
3.2	Ranking scores evaluated in the whole images . . . . .	73
3.3	RMSEs in the 5 lower-foreground-percentage image pairs . . . . .	74
3.4	Ranking scores evaluated in the background areas . . . . .	75
4.1	Properties of the warping models . . . . .	100
4.2	RMSE values using SC30 . . . . .	109
4.3	NEN values using SC30 . . . . .	114
4.4	RMSE values using BT40 . . . . .	115
4.5	NEN values using BT40 . . . . .	116
4.6	Summary of the RMSE and NEN values . . . . .	117
5.1	Characteristics of the real stacks of images . . . . .	139
5.2	Methods ranking using synthetic stacks . . . . .	140
5.3	Rankings achieved using the UQIN metrics . . . . .	142
5.4	AUQI from the synthetic stacks . . . . .	143
5.5	AUQI from the real stacks . . . . .	146
5.6	Ranking of methods using real stacks . . . . .	146
5.7	License details by Microscopy Research and Technique. . . . .	148



# Bibliography

- [1] M. Kumin. *The Microscope*. HarperCollins Publishers, 1984 (cit. on p. 2).
- [2] B. J. Ford. *Single Lens: The Story of the Simple Microscope*. Harper & Row (New York), 1985 (cit. on p. 2).
- [3] URL: [www.nature.com/milestones/milelight/](http://www.nature.com/milestones/milelight/) (cit. on p. 2).
- [4] URL: [www.microscopyu.com](http://www.microscopyu.com) (cit. on p. 2).
- [5] M. Freebody. “Choosing the right microscopy system”. In: *Biophotonics* 19.10 (2012), pp. 18–21 (cit. on p. 2).
- [6] J. C. Waters. “Accuracy and Precision in Quantitative Fluorescence Microscopy”. In: *The Journal of Cell Biology* 185.7 (2009), pp. 1135–1148 (cit. on pp. 3, 18, 48).
- [7] D. B. Murphy. *Fundamentals of Light Microscopy and Digital Imaging*. John Wiley and Sons, 2001 (cit. on p. 3).
- [8] J. W. Lichtman and J.-A. Conchello. “Fluorescence microscopy”. In: *Nature Methods* 2.12 (2005), pp. 910–919 (cit. on p. 3).
- [9] F. Zernike. “How I discovered phase contrast”. In: *Science* 121 (1955), pp. 345–349 (cit. on p. 3).
- [10] D. E. Wolf, C. Samarasekera, and J. R. Swedlow. “Quantitative Analysis of Digital Microscope Images”. In: *Methods in Cell Biology* 81 (2007), pp. 365–396 (cit. on pp. 4, 10, 48).
- [11] URL: [www.filippopiccinini.altervista.org](http://www.filippopiccinini.altervista.org) (cit. on pp. 7, 23, 30, 58, 120, 131, 133, 136, 147, 155).
- [12] B. Gibaud. “Semantic web: key technologies for bridging imaging and translational medicine”. In: *Imaging in Medicine* 2.6 (2010), 609–611 (cit. on p. 10).

- [13] I. T. Young. *Shading Correction: Compensation for Illumination and Sensor Inhomogeneities*. John Wiley & Sons, Inc., 2001 (cit. on pp. 10, 18).
- [14] F.-M. Leong, M. Brady, and J. O. McGee. “Correction of Uneven Illumination (Vignetting) in Digital Microscopy Images”. In: *Journal of Clinical Pathology* 56.8 (2003), pp. 619–621 (cit. on pp. 10, 13, 15).
- [15] Y.-N. Sun et al. “Live cell tracking based on cellular state recognition from microscopic images”. In: *Journal of Microscopy* 235.1 (2009), pp. 94–105 (cit. on p. 10).
- [16] Z. Bulj et al. “Protein kinase B/AKT isoform 2 drives migration of human mesenchymal stem cells”. In: *International Journal of Oncology* 42.1 (2013), pp. 118–126 (cit. on p. 10).
- [17] S. S. Poon et al. “Intensity calibration and automated cell cycle gating for high-throughput image-based siRNA screens of mammalian cells”. In: *Cytometry Part A* 73A.10 (2008), pp. 904–917 (cit. on p. 10).
- [18] I.-M. Sintorn et al. “Gradient based intensity normalization”. In: *Journal of Microscopy* 240.3 (2010), pp. 249–258 (cit. on p. 10).
- [19] D. Gareau et al. “Confocal mosaicing microscopy in skin excisions: a demonstration of rapid surgical pathology”. In: *Journal of Microscopy* 233.1 (2009), 149–159 (cit. on pp. 10, 85, 89).
- [20] C. Sun et al. “Mosaicing of microscope images with global geometric and radiometric corrections”. In: *Journal of Microscopy* 224.2 (2006), 158–165 (cit. on pp. 10, 82, 85, 89).
- [21] W.-Y. Hsu, P. W. Poon, and Y.-N. Sun. “Automatic Seamless Mosaicing of Microscopic Images: Enhancing Appearance with Colour Degradation Compensation and Wavelet-based Blending”. In: *Journal of Microscopy* 231.3 (2008), pp. 408–418 (cit. on pp. 10, 87–89, 102).
- [22] L. Carozza, A. Bevilacqua, and F. Piccinini. “Mosaicing of Optical Microscope Imagery Based on Visual Information”. In: *Proc. 33<sup>th</sup> annual international conference of the IEEE Engineering in Medicine and Biology Society (EMBS 2011)*. Vol. 1. Boston, MA, U.S.A., Aug. 30–Sept. 3, 2011, pp. 6162–6165 (cit. on pp. 10, 120, 141).
- [23] L. Carozza, A. Bevilacqua, and F. Piccinini. “An Incremental Method for Mosaicing of Optical Microscope Imagery”. In: *Proc. 8<sup>th</sup> annual IEEE Symposium on Computational Intelligence in Bioinformatics and Computational Biology (CIBCB 2011)*. Vol. 1. Paris, France, Apr. 11–15, 2011, pp. 55–60 (cit. on pp. 10, 120).

- [24] A. Köhler. “Ein neues Beleuchtungsverfahren für mikrographische Zwecke”. In: *Zeitschrift für wissenschaftliche Mikroskopie* 10 (1893), 433–440 (cit. on pp. 10, 91).
- [25] M. Spencer. *Fundamentals of Light Microscopy*. Cambridge University Press, New York, 1982 (cit. on p. 10).
- [26] S. Kang and R. Weiss. “Can we calibrate a camera using an image of a flat, textureless lambertian surface?” In: *Proc. 6<sup>th</sup> European Conference on Computer Vision (ECCV 2000)*. Vol. 1843. Dublin, Ireland, June 26–July 1, 2000, pp. 640–653 (cit. on p. 10).
- [27] D. B. Goldman. “Vignette and Exposure Calibration and Compensation”. In: *IEEE Transactions on Pattern Analysis and Machine Intelligence* 32.12 (2010), pp. 2276–2288 (cit. on pp. 10, 13, 16, 18).
- [28] M. Aggarwal, H. Hua, and N. Ahuja. “On cosine-fourth and vignetting effects in real lenses”. In: *Proc. 8<sup>th</sup> IEEE International Conference on Computer Vision (ICCV 2001)*. Vol. 1. Vancouver, BC, Canada, July 7–14, 2001, pp. 472–479 (cit. on p. 10).
- [29] R. G. Willson and S. A. Shafer. “What is the center of the image?” In: *Journal Optics Soc. Am. A* 11.11 (1994), pp. 2946–2955 (cit. on p. 10).
- [30] S. Bolte and F. Cordelieres. “A guided tour into subcellular colocalization analysis in light microscopy”. In: *Journal of Microscopy* 224.3 (2006), pp. 213–232 (cit. on pp. 11, 15).
- [31] B. F. Tek, A. Dempster, and I. Kale. “Computer vision for microscopy diagnosis of malaria”. In: *Malaria Journal* 8.1 (2009), p. 153 (cit. on pp. 11, 12, 15).
- [32] G. D. Marty. “Blank-field Correction for Achieving a Uniform White Background in Brightfield Digital Photomicrographs”. In: *BioTechniques* 42.6 (2007), pp. 716–720 (cit. on pp. 12, 15).
- [33] D. Hasler and S. Süsstrunk. “Colour Handling in Panoramic Photography”. In: *Proc. SPIE 2001*. San Diego, CA, U.S.A., July 29, 2001, pp. 709–712 (cit. on pp. 12, 15, 93).
- [34] P. G. Cavalcanti and J. Scharcanski. “Automated prescreening of pigmented skin lesions using standard cameras”. In: *Computerized Medical Imaging and Graphics* 35.6 (2011), pp. 481–491 (cit. on pp. 12, 15, 19).
- [35] D. H. Rapoport et al. “A Novel Validation Algorithm Allows for Automated Cell Tracking and the Extraction of Biologically Meaningful Parameters”. In: *PLoS ONE* 6.11 (2011), e27315 (cit. on pp. 13, 15).
- [36] Y. Zheng et al. “Single-Image Vignetting Correction Using Radial Gradient Symmetry”. In: *Proc. IEEE Computer Society Conference on*

- Computer Vision and Pattern Recognition (CVPR 2008)*. Anchorage, AK, U.S.A., June 23–28, 2008, pp. 1–8 (cit. on pp. 13, 15).
- [37] Y. Zheng, S. Lin, and S. B. Kang. “Single-Image Vignetting Correction”. In: *Proc. IEEE Computer Society Conference on Computer Vision and Pattern Recognition (CVPR 2006)*. Vol. 1. New York, NY, U.S.A., June 7–22, 2006, pp. 461–468 (cit. on pp. 13, 15).
- [38] A. Shariff et al. “Automated Image Analysis for High-Content Screening and Analysis”. In: *Journal of Biomolecular Screening* 15.7 (2010), pp. 726–734 (cit. on pp. 13, 16, 17, 48).
- [39] V. Ljosa and A. E. Carpenter. “Introduction to the Quantitative Analysis of Two-Dimensional Fluorescence Microscopy Images for Cell-Based Screening”. In: *PLoS Comput Biol* 5.12 (2009), e1000603 (cit. on pp. 13, 16, 18, 49).
- [40] S. J. Kim and M. Pollefeys. “Robust Radiometric Calibration and Vignetting Correction”. In: *IEEE Transactions on Pattern Analysis and Machine Intelligence* 30.4 (2008), pp. 562–576 (cit. on pp. 13, 16, 18).
- [41] A. Can et al. “Multi-modal imaging of histological tissue sections”. In: *Proc. 5<sup>th</sup> IEEE International Symposium on Biomedical Imaging: From Nano to Macro (ISBI 2008)*. Paris, France, May 14–17, 2008, pp. 288–291 (cit. on pp. 13, 16).
- [42] T. R. Jones et al. “Methods for high-content, high-throughput image-based cell screening”. In: *Proc. of the Workshop on Microscopic Image Analysis with Applications in Biology (MIAAB 2006)*. Copenhagen, Denmark, Oct. 5, 2006, pp. 65–72 (cit. on pp. 13, 16, 17, 50).
- [43] M. S. Vokes and A. E. Carpenter. *Using CellProfiler for automatic identification and measurement of biological objects in images*. John Wiley & Sons, Inc., 2008 (cit. on pp. 13, 16, 17, 50, 54).
- [44] C. Baravalle et al. “Microscopic Characterization of Follicular Structures in Letrozole-induced Polycystic Ovarian Syndrome in the Rat”. In: *Archives of Medical Research* 37.7 (2006), pp. 830–839 (cit. on p. 15).
- [45] S. Kumar et al. “Segmentation of microscope cell images via adaptive eigenfilters”. In: *Proc. 11<sup>th</sup> International Conference on Image Processing (ICIP 2004)*. Vol. 1. Singapore, Oct. 24–27, 2004, pp. 135–138 (cit. on p. 15).
- [46] F. Shen et al. “Functional proteometrics for cell migration”. In: *Cytometry Part A* 69A.7 (2006), pp. 563–572 (cit. on p. 15).

- [47] C. Souchier et al. “Data reproducibility in fluorescence image analysis”. In: *Methods in Cell Science* 25.3 (2004), pp. 195–200 (cit. on pp. 15, 19).
- [48] N. R. Salvetti et al. “Cell proliferation and survival mechanisms underlying the abnormal persistence of follicular cysts in bovines with cystic ovarian disease induced by ACTH”. In: *Animal Reproduction Science* 122.1-2 (2010), pp. 98–110 (cit. on p. 15).
- [49] C. Rousselle et al. “Chromatin Texture Analysis in Living Cells”. In: *The Histochemical Journal* 31.1 (1999), pp. 63–70 (cit. on p. 15).
- [50] J. Varayoud et al. “Neonatal Exposure to Bisphenol A Alters Rat Uterine Implantation-Associated Gene Expression and Reduces the Number of Implantation Sites”. In: *Endocrinology* 152.3 (2011), pp. 1101–1111 (cit. on p. 15).
- [51] S. E. Weigum et al. “Cell-based sensor for analysis of EGFR biomarker expression in oral cancer”. In: *Lab Chip* 7.8 (2007), pp. 995–1003 (cit. on pp. 15, 19).
- [52] P. Loetscher et al. “Argon: Neuroprotection in in vitro models of cerebral ischemia and traumatic brain injury”. In: *Critical Care* 13.6 (2009), pp. 1–9 (cit. on p. 15).
- [53] J. Rossaint et al. “Propofol: neuroprotection in an in vitro model of traumatic brain injury”. In: *Critical Care* 13.2 (2009), pp. 1–8 (cit. on p. 15).
- [54] L. Oomen et al. “Immersion oil for high-resolution live-cell imaging at 37C: optical and physical characteristics”. In: *Journal of Microscopy* 232.2 (2008), pp. 353–361 (cit. on p. 15).
- [55] E. Cho and S. Lockett. “Calibration and standardization of the emission light path of confocal microscopes”. In: *Journal of Microscopy* 223.1 (2006), pp. 15–25 (cit. on pp. 15, 89).
- [56] A. Fahlenkamp et al. “Expression analysis of the early chemokine response 4h after in vitro traumatic brain injury”. In: *Inflammation Research* 60.4 (2010), pp. 379–387 (cit. on p. 15).
- [57] S. A. Blant et al. “Uptake and localisation of mTHPC (Foscan) and its<sup>14</sup>C-labelled form in normal and tumour tissues of the hamster squamous cell carcinoma model: a comparative study”. In: *British Journal of Cancer* 87.12 (2002), pp. 1470–1478 (cit. on p. 15).
- [58] Y. Tan et al. “Amniotic membrane inhibits squamous metaplasia of human conjunctival epithelium”. In: *American journal of physiology. Cell physiology* 70.1 (2011), pp. C115–C125 (cit. on p. 15).

- [59] V. L. Bosquiazzo et al. “Effects of Neonatal Exposure to Bisphenol A on Steroid Regulation of Vascular Endothelial Growth Factor Expression and Endothelial Cell Proliferation in the Adult Rat Uterus”. In: *Biology of Reproduction* 82.1 (2010), pp. 96–95 (cit. on pp. 15, 134).
- [60] L. Monje et al. “Exposure of neonatal female rats to bisphenol A disrupts hypothalamic LHRH pre-mRNA processing and estrogen receptor alpha expression in nuclei controlling estrous cyclicity”. In: *Reproductive Toxicology* 30.4 (2010), pp. 625–634 (cit. on p. 15).
- [61] H. A. Rodriguez et al. “Neonatal exposure to bisphenol A reduces the pool of primordial follicles in the rat ovary”. In: *Reproductive Toxicology* 30.4 (2010), pp. 550–557 (cit. on p. 15).
- [62] Y. G. Patel et al. “Confocal reflectance mosaicing of basal cell carcinomas in Mohs surgical skin excisions”. In: *Journal of Biomedical Optics* 12.3 (2007), pp. 034027–1–034027–10 (cit. on pp. 15, 82, 89).
- [63] J. M. Zwier et al. “Image calibration in fluorescence microscopy”. In: *Journal of Microscopy* 216.1 (2004), pp. 15–24 (cit. on pp. 15, 19, 89).
- [64] M. A. Model. *Intensity Calibration and Shading Correction for Fluorescence Microscopes*. John Wiley & Sons, Inc., 2006, pp. 10.14.1–10.14.7 (cit. on pp. 15, 18).
- [65] M. A. Model and J. K. Burkhardt. “A standard for calibration and shading correction of a fluorescence microscope”. In: *Cytometry Part A* 44.4 (2001), pp. 309–316 (cit. on pp. 15, 18, 19).
- [66] Z. Jericevic et al. “Validation of an imaging system: steps to evaluate and validate a microscope imaging system for quantitative studies”. In: *Methods Cell Biol* 30 (1989), pp. 47–83 (cit. on pp. 15, 18, 19).
- [67] T. il Oh et al. “Real-time fluorescence detection of multiple microscale cell culture analog devices in situ”. In: *Cytometry Part A* 71A.10 (2007), pp. 857–865 (cit. on p. 15).
- [68] M. A. Model, J. L. Reese, and G. C. Fraizer. “Measurement of wheat germ agglutinin binding with a fluorescence microscope”. In: *Cytometry Part A* 75A.10 (2009), pp. 874–881 (cit. on pp. 15, 18, 19).
- [69] D. W. Schelshorn et al. “Expression of hemoglobin in rodent neurons”. In: *Journal of Cerebral Blood Flow and Metabolism* 29.3 (2009), pp. 585–595 (cit. on pp. 15, 19).
- [70] A. Burga, M. O. Casanueva, and B. Lehner. “Predicting mutation outcome from early stochastic variation in genetic interaction partners”. In: *Nature* 480.7376 (2011), pp. 250–253 (cit. on p. 15).

- [71] Y.-J. Kwon et al. “High content image analysis for human H4 neuroglioma cells exposed to CuO nanoparticles”. In: *Journal of Biomolecular Screening* 12.5 (2007), pp. 621–627 (cit. on p. 15).
- [72] W. Yu. “Practical anti-vignetting methods for digital cameras”. In: *IEEE Transactions on Consumer Electronics* 50.4 (2004), pp. 975–983 (cit. on pp. 15, 19, 93).
- [73] K. Li et al. “Cell population tracking and lineage construction with spatiotemporal context”. In: *Medical Image Analysis* 12.5 (2008), pp. 546–566 (cit. on p. 15).
- [74] F. L. Gimeno et al. “In vivo lamellar keratoplasty using platelet-rich plasma as a bioadhesive”. In: *Eye* 24.2 (2009), pp. 368–375 (cit. on p. 15).
- [75] Y. Zheng et al. “Single-Image Vignetting Correction”. In: *IEEE Transactions on Pattern Analysis and Machine Intelligence* 31.12 (2009), pp. 2243–2256 (cit. on p. 15).
- [76] W. Yu, Y. Chung, and J. Soh. “Vignetting distortion correction method for high quality digital imaging”. In: *Proc. 17<sup>th</sup> International Conference on Pattern Recognition (ICPR 2004)*. Cambridge, U.K., Aug. 23–26, 2004, pp. 666–669 (cit. on p. 15).
- [77] K. He, P. F. Tang, and R. Liang. “Vignetting image correction based on gaussian quadrics fitting”. In: *Proc. 5<sup>th</sup> International Conference on Natural Computation (ICNC 2009)*. Vol. 5. Tianjian, China, Aug. 14–15, 2009, pp. 158–161 (cit. on p. 15).
- [78] S. Lyu. “Estimating vignetting function from a single image for image authentication”. In: *Proc. 12<sup>th</sup> ACM workshop on Multimedia and security (MM&Sec 2010)*. Roma, Italy, Sept. 9–10, 2010, pp. 3–12 (cit. on p. 15).
- [79] C. Wählby et al. “Algorithms for cytoplasm segmentation of fluorescence labelled cells”. In: *Analytical Cellular Pathology* 24.2-3 (2002), pp. 101–111 (cit. on p. 15).
- [80] G. Karabourniotis et al. “Epicuticular phenolics over guard cells: exploitation for in situ stomatal counting by fluorescence microscopy and combined image analysis”. In: *Annals of Botany* 87.5 (2001), pp. 631–639 (cit. on p. 15).
- [81] S. Bisht et al. “A polymeric nanoparticle formulation of curcumin ameliorates CCl<sub>4</sub>-induced hepatic injury and fibrosis through reduction of pro-inflammatory cytokines and stellate cell activation”. In: *Laboratory Investigation* 91.9 (2011), pp. 1383–1395 (cit. on pp. 16, 19).

- [82] J. Lindblad and E. Bengtsson. “A comparison of methods for estimation of intensity nonuniformities in 2d and 3d microscope images of fluorescence stained cells”. In: *Proc. 12<sup>th</sup> Scandinavian Conference on Image Analysis (SCIA 2001)*. Bergen, Norway, June 11–14, 2001, pp. 264–271 (cit. on pp. 16, 17).
- [83] S. J. Kim and M. Pollefeys. “Radiometric alignment of image sequences”. In: *Proc. IEEE Computer Society Conference on Computer Vision and Pattern Recognition (CVPR 2004)*. Vol. 1. Washington, DC, U.S.A., June 27–July 2, 2004, pp. 645–651 (cit. on pp. 16, 18).
- [84] D. B. Goldman and J.-H. Chen. “Vignette and exposure calibration and compensation”. In: *Proc. 10<sup>th</sup> IEEE International Conference on Computer Vision (ICCV 2005)*. Vol. 1. Beijing, China, Oct. 17–20, 2005, pp. 899–906 (cit. on pp. 16, 18).
- [85] A. Litvinov and Y. Y. Schechner. “Radiometric framework for image mosaicking”. In: *Journal of the Optical Society of America A* 22.5 (2005), pp. 839–848 (cit. on pp. 16, 18, 90).
- [86] A. Litvinov and Y. Y. Schechner. “Addressing radiometric nonidealities: a unified framework”. In: *Proc. IEEE Computer Society Conference on Computer Vision and Pattern Recognition (CVPR 2005)*. Vol. 2. San Diego, CA, U.S.A., June 20–26, 2005, pp. 52–59 (cit. on pp. 16, 18).
- [87] A. E. Carpenter et al. “CellProfiler: image analysis software for identifying and quantifying cell phenotypes”. In: *Genome biology* 7.10 (2006), R100.1–R100.11 (cit. on pp. 17, 50).
- [88] M. R. Lamprecht, D. M. Sabatini, and A. E. Carpenter. “CellProfiler<sup>TM</sup>: free, versatile software for automated biological image analysis”. In: *BioTechniques* 42.1 (2007), pp. 71–75 (cit. on pp. 17, 50).
- [89] G. Babaloukas et al. “Evaluation of three methods for retrospective correction of vignetting on medical microscopy images utilizing two open source software tools”. In: *Journal of Microscopy* 244.3 (2011), pp. 320–324 (cit. on p. 18).
- [90] C. Doutre and P. Nasiopoulos. “Fast Vignetting Correction and Color Matching for Panoramic Image Stitching”. In: *Proc. 16<sup>th</sup> IEEE International Conference on Image Processing (ICIP 2009)*. Cairo, Egypt, Nov. 7–11, 2009, pp. 709–712 (cit. on pp. 19, 87, 89, 93, 102).
- [91] M. H. Wilkinson. “Shading correction and calibration in bacterial fluorescence measurement by image processing system”. In: *Computer Methods and Programs in Biomedicine* 44.2 (1994), pp. 61–67 (cit. on p. 19).

- [92] H.-S. Wu, J. Berba, and J. Gil. “Iterative thresholding for segmentation of cells from noisy images”. In: *Journal of Microscopy* 197.3 (2000), pp. 296–304 (cit. on p. 21).
- [93] M. Eramian et al. “Segmentation of epithelium in H&E stained odontogenic cysts”. In: *Journal of Microscopy* 244.3 (2011), pp. 273–292 (cit. on p. 21).
- [94] N. Otsu. “A threshold selection method from gray-level histograms”. In: *IEEE Transactions on Systems, Man and Cybernetics* 9.1 (1979), pp. 62–66 (cit. on p. 21).
- [95] T. J. Collins. “ImageJ for microscopy”. In: *BioTechniques* 43.S1 (2007), S25–S30 (cit. on pp. 23, 90).
- [96] URL: <http://rsbweb.nih.gov/ij> (cit. on pp. 23, 130).
- [97] URL: [www.gimp.org](http://www.gimp.org) (cit. on p. 23).
- [98] S. Lazzari et al. “Dual solutions for viscous mixed convection flows in a vertical circular duct: a numerical benchmark”. In: *Proc. European COMSOL Multiphysics Conference 2007*. Grenoble, France, Oct. 23–24, 2007, pp. 343–349 (cit. on p. 31).
- [99] K. Loewke et al. “In vivo micro-image mosaicing”. In: *IEEE Transactions on Biomedical Engineering* 58.1 (2011), pp. 159–171 (cit. on pp. 36, 101).
- [100] J. Shi and C. Tomasi. “Good features to track”. In: *Proc. IEEE Computer Society Conference on Computer Vision and Pattern Recognition (CVPR 1994)*. Ithaca, NY, U.S.A., June 21–23, 1994, pp. 593–600 (cit. on pp. 36, 79, 93, 95).
- [101] B. D. Lucas and T. Kanade. “An iterative image registration technique with an application to stereo vision”. In: *Proc. 7<sup>th</sup> International Joint Conference on Artificial Intelligence (IJCAI 1981)*. Vancouver, British Columbia, Canada, Aug. 24–28, 1981, pp. 674–679 (cit. on pp. 36, 95).
- [102] Z. Wang et al. “Image quality assessment: from error visibility to structural similarity”. In: *IEEE Transactions on Image Processing* 13.4 (2004), pp. 600–612 (cit. on p. 37).
- [103] Z. Wang and A. C. Bovik. “Mean squared error: Love it or leave it? A new look at Signal Fidelity Measures”. In: *IEEE Signal Processing Magazine* 26.1 (2009), pp. 98–117 (cit. on pp. 37, 106).
- [104] Q. Wang, D. Yu, and Y. Shen. “An overview of image fusion metrics”. In: *Proc. of IEEE International Instrumentation and Measurement Technology Conference (I2MTC 2009)*. Singapore, May 5–7, 2009, pp. 918–9233 (cit. on p. 38).

- [105] Z. Wang and A. C. Bovik. “A Universal Image Quality Index”. In: *IEEE Signal Processing Letters* 9.3 (2002), pp. 81–84 (cit. on pp. 38, 128, 134, 135).
- [106] G. Piella and H. Heijmans. “A new quality metric for image fusion”. In: *Proc. 10<sup>th</sup> of International Conference on Image Processing (ICIP 2003)*. Vol. 3. Barcelona, Spain, Sept. 14–17, 2003, pp. 173–176 (cit. on pp. 38, 129, 134, 135).
- [107] A. Gherardi, A. Bevilacqua, and F. Piccinini. “Illumination field estimation through background detection in optical microscopy”. In: *Proc. 8<sup>th</sup> annual IEEE Symposium on Computational Intelligence in Bioinformatics and Computational Biology (CIBCB 2011)*. Vol. 1. Paris, France, Apr. 11–15, 2011, pp. 49–54 (cit. on pp. 42, 141).
- [108] A. Bevilacqua, F. Piccinini, and A. Gherardi. “Vignetting correction by exploiting an optical microscopy image sequence”. In: *Proc. 33<sup>th</sup> annual international conference of the IEEE Engineering in Medicine and Biology Society (EMBS 2011)*. Vol. 1. Boston, MA, U.S.A., Aug. 30–Sept. 3, 2011, pp. 6166–6169 (cit. on pp. 42, 141).
- [109] A. Bevilacqua and F. Piccinini. “Is an empty field the best reference to correct vignetting in microscopy?” In: *Proc. 7<sup>th</sup> International Workshop on Biosignal Interpretation (BSI 2012)*. Vol. 1. Como, Italy, July 2–4, 2012, pp. 267–270 (cit. on pp. 42, 91).
- [110] F. Piccinini et al. “Multi-image based method to correct vignetting effect in light microscopy images”. In: *Journal of Microscopy* 248.1 (2012), pp. 6–22 (cit. on pp. 42, 44).
- [111] A. E. Carpenter. “Software opens the door to quantitative imaging”. In: *Nature Methods* 4.2 (2007), pp. 120–121 (cit. on pp. 49, 89).
- [112] S. E. Mohr and N. Perrimon. “RNAi screening: new approaches, understandings, and organisms”. In: *Wiley Interdisciplinary Reviews: RNA* (2011) (cit. on p. 49).
- [113] W. M. Ahmed et al. “State of the Art in Information Extraction and Quantitative Analysis for Multimodality Biomolecular Imaging”. In: *Proceedings of the IEEE* 96.3 (2008), pp. 512–531 (cit. on p. 49).
- [114] F. Piccinini et al. “Vignetting and photo-bleaching correction in automated fluorescence microscopy from an array of overlapping images”. In: *Accepted to 10<sup>th</sup> IEEE International Symposium on Biomedical Imaging (ISBI 2013)*. San Francisco, CA, U.S.A., Apr. 7–11, 2013 (cit. on p. 79).

- [115] W. Tong. “Subpixel image registration with reduced bias”. In: *Optics Letters* 36.5 (2011), pp. 763–765 (cit. on p. 82).
- [116] A. Bevilacqua and P. Azzari. “High-Quality Real Time Motion Detection Using PTZ Cameras”. In: *Proc. IEEE International Conference on Video and Signal Based Surveillance (AVSS 2006)*. Sydney, Australia, Nov. 22–24, 2006, p. 23 (cit. on p. 82).
- [117] K. A. Frenkel. “Panning for science”. In: *Science* 330.6005 (2010), pp. 748–749 (cit. on p. 82).
- [118] F. Guillemin, M.-F. Devaux, and F. Guillon. “Evaluation of plant histology by automatic clustering based on individual cell morphological features”. In: *Image Analysis & Stereology* 23.1 (2004), pp. 13–22 (cit. on p. 82).
- [119] R. Hartley and A. Zisserman. *Multiple View Geometry In Computer Vision*. Cambridge University Press, New York, 2000 (cit. on pp. 82, 97, 98).
- [120] M. Emmenlauer et al. “XuvTools: free, fast and reliable stitching of large 3D datasets”. In: *Journal of Microscopy* 233.1 (2009), pp. 42–60 (cit. on pp. 83, 85, 90).
- [121] A. Behrens et al. “Real-time image composition of bladder mosaics in fluorescence endoscopy”. In: *Computer Science, Research and Development* 26.1-2 (2011), pp. 51–64 (cit. on p. 83).
- [122] B. Zitová and J. Flusser. “Image registration methods: a survey”. In: *Image and Vision Computing* 21.11 (2003), pp. 977–1000 (cit. on pp. 83, 85).
- [123] D. P. Capel. “Image Mosaicing and Super Resolution”. PhD thesis. Department of Engineering Science, University of Oxford, 2001 (cit. on pp. 83, 85, 89).
- [124] D. L. G. Hill et al. “Medical image registration”. In: *Physics in Medicine and Biology* 46.3 (2001), R1–R45 (cit. on pp. 83, 85).
- [125] R. Szeliski. “Image alignment and stitching: a tutorial”. In: *Foundations and Trends R in Computer Graphics and Vision* 2.1 (2006), pp. 1–104 (cit. on p. 83).
- [126] S. Preibisch, S. Saalfeld, and P. Tomancak. “Globally optimal stitching of tiled 3D microscopic image acquisitions”. In: *Bioinformatics* 25.11 (2009), 1463–1465 (cit. on pp. 83, 85, 90).
- [127] M. Brown and D. G. Lowe. “Automatic Panoramic Image Stitching using Invariant Features”. In: *International Journal of Computer Vision* 74.1 (2007), pp. 59–73 (cit. on pp. 83, 88, 90).

- [128] P. Thevenaz and M. Unser. “User-friendly semiautomated assembly of accurate image mosaics in microscopy”. In: *Microscopy research and techniques* 70 (2007), 131–146 (cit. on pp. 83, 90).
- [129] E. Flaberg et al. “Extended Field Laser Confocal Microscopy (EFLCM): Combining automated Gigapixel image capture with in silico virtual microscopy”. In: *BMC Medical Imaging* 8 (2008), pp. 8–13 (cit. on pp. 83, 89).
- [130] R. Clements, E. Mintz, and J. Blank. “High resolution stereoscopic volume visualization of the mouse arginine vasopressin system”. In: *Journal of biomolecular screening* 187.1 (2010), pp. 41–45 (cit. on p. 83).
- [131] L. G. Brown. “A survey of image registration techniques”. In: *ACM computing surveys* 24.4 (1992), pp. 325–376 (cit. on p. 85).
- [132] A. Bevilacqua and P. Azzari. “A Fast and Reliable Image Mosaicing Technique with Application to Wide Area Motion Detection”. In: *Proc. 4<sup>th</sup> International Conference on Image Analysis and Recognition (ICIAR 2007)*. Vol. 4633. Montreal, Canada, Aug. 22–24, 2007, pp. 501–512 (cit. on pp. 85, 101).
- [133] Q. Zhi and J. R. Cooperstock. “Wide-baseline image mosaicing for indoor environments”. In: *Proc. 18<sup>th</sup> International Conference on Pattern Recognition (ICPR 2006)*. Vol. 1. Hong Kong, China, Aug. 20–24, 2006 (cit. on pp. 85, 90).
- [134] N. Bedard et al. “Real-time video mosaicing with a high-resolution microendoscope”. In: *Biomedical Optics Express* 3.10 (2012), pp. 2428–2435 (cit. on p. 85).
- [135] E. Trucco and A. Verri. *Introductory Techniques for 3-D Computer Vision*. Prentice Hall, 1998 (cit. on p. 85).
- [136] E.-Y. Kang, I. Cohen, and G. Medioni. “A graph-based global Registration for 2D mosaics”. In: *Proc. 15<sup>th</sup> International Conference on Pattern Recognition (ICPR 2000)*. Vol. 1. Barcelona, Spain, Sept. 3–7, 2000, pp. 257–260 (cit. on pp. 85, 89).
- [137] D. Steckhan et al. “Efficient large scale image stitching for virtual microscopy”. In: *Proc. 30<sup>th</sup> annual international conference of the IEEE Engineering in Medicine and Biology Society (EMBS 2008)*. Vancouver, British Columbia, Canada, Aug. 20–25, 2008, pp. 4019–4023 (cit. on p. 85).
- [138] V. Rankov et al. “An algorithm for image stitching and blending”. In: *Proc. SPIE 2005*. San Diego, CA, U.S.A., Feb. 12–17, 2005, pp. 190–199 (cit. on pp. 85, 89, 102).

- 
- [139] Z. Xu. “Consistent image alignment for video mosaicing”. In: *Signal, Image and Video Processing* (2011), pp. 1–7 (cit. on pp. 85, 89).
- [140] V. M. Roberto Marzotto Andrea Fusiello. “High resolution video mosaicing with global alignment”. In: *Proc. IEEE Computer Society Conference on Computer Vision and Pattern Recognition (CVPR 2004)*. Vol. 1. Washington, DC, U.S.A., June 27–July 2, 2004, pp. 692–698 (cit. on pp. 85, 89).
- [141] T. Vercauteren et al. “Mosaicing of Confocal Microscopic In Vivo Soft Tissue Video Sequences”. In: *Proc. 8<sup>th</sup> Medical Image Computing and Computer-Assisted Intervention (MICCAI 2005)*. Vol. 3749. Palm Springs, CA, U.S.A., Oct. 26–29, 2005, pp. 753–760 (cit. on p. 85).
- [142] A. Eden, M. Uyttendaele, and R. Szeliski. “Seamless Image Stitching of Scenes with Large Motions and Exposure Differences”. In: *Proc. IEEE Computer Society Conference on Computer Vision and Pattern Recognition (CVPR 2006)*. Vol. 2. New York, NY, U.S.A., June 7–22, 2006, pp. 2498–2505 (cit. on p. 85).
- [143] J. Jia and C.-K. Tang. “Image registration with global and local luminance alignment”. In: *Proc. 9<sup>th</sup> IEEE International Conference on Computer Vision (ICCV 2003)*. Vol. 1. Nice, France, Oct. 13–16, 2003, pp. 156–163 (cit. on p. 85).
- [144] B. Glocker et al. “Deformable medical image registration: setting the state of the art with discrete methods”. In: *Annual review of biomedical engineering* 13 (2011), pp. 219–244 (cit. on p. 85).
- [145] T. Tuytelaars and K. Mikolajczyk. “Local invariant feature detectors: a survey”. In: *Foundations and Trends in Computer Graphics and Vision* 3.3 (2007), pp. 219–244 (cit. on pp. 86, 89).
- [146] G. D. Evangelidis and E. Z. Psarakis. “Parametric image alignment using enhanced correlation coefficient maximization”. In: *IEEE Transactions On Pattern Analysis And Machine Intelligence* 30.10 (2008), pp. 1858–1865 (cit. on p. 87).
- [147] A. Bevilacqua and P. Azzari. “A High Performance Exact Histogram Specification Algorithm”. In: *Proc. 14<sup>th</sup> International Conference on Image Analysis and Processing (ICIAP 2007)*. Modena, Italy, Sept. 10–14, 2007, pp. 623–628 (cit. on p. 87).
- [148] P. J. Burt and E. H. Adelson. “ACM Transactions on Graphics”. In: *Journal of Biomedical Optics* 2.4 (1983), pp. 217–236 (cit. on p. 88).
- [149] H.-Y. Shum and R. Szeliski. “Construction and refinement of panoramic mosaics with global and local alignment”. In: *Proc. 6<sup>th</sup> International*
-

- Conference on Computer Vision (ICCV 1998)*. Bombay, India, Jan. 4–7, 1998, pp. 953–956 (cit. on p. 88).
- [150] S. Coorg and S. Teller. “Spherical mosaics with quaternions and dense correlation”. In: *International Journal of Computer Vision* 37.3 (2000), pp. 259–273 (cit. on pp. 88, 89).
- [151] C. Sun et al. “Mosaicing of microscope images”. In: *Proc. Digital Image Computing: Techniques and Applications (DICTA 2005)*. Cairns, Australia, Dec. 6–8, 2005, p. 50 (cit. on pp. 88, 89).
- [152] S. K. Chow et al. “Automated microscopy system for mosaic acquisition and processing”. In: *Journal of Microscopy* 222.2 (2006), 76–84 (cit. on pp. 88, 89).
- [153] F. Lu and S. Xia. “Microscopic image mosaicing algorithm based on normalized moment of inertia”. In: *Advanced Intelligent Computing Theories and Applications* 2.21 (2007), 1010–1017 (cit. on p. 89).
- [154] C. Harris and M. Stephens. “A combined corner and edge detector”. In: *Proc. 4<sup>th</sup> Alvey Vision Conference*. Vol. 1. Manchester, UK, Aug. 31–Sept. 2, 1988, 147–151 (cit. on p. 89).
- [155] A. Elibol et al. “A new global alignment method for feature based image mosaicing”. In: *Proc. 4<sup>th</sup> International Symposium Visual Computing (ISVC 2008)*. Vol. 5359. Las Vegas, NV, U.S.A., Dec. 1–3, 2008, pp. 257–266 (cit. on p. 89).
- [156] B. Ma et al. “Use of Autostitch for automatic stitching of microscope images”. In: *Micron* 38.5 (2007), pp. 492–499 (cit. on pp. 89, 90).
- [157] K. Loewke et al. “Real-time image mosaicing with a hand-held dual-axes confocal microscope”. In: *Proc. SPIE 2008, Endoscopic Microscopy III*. Vol. 6851. San Jose, CA, U.S.A., Feb. 5, 2008, 68510F–68519F (cit. on pp. 89, 93, 102).
- [158] P. F. McLauchlan and A. Jaenicke. “Image mosaicing using sequential bundle adjustment”. In: *Image and Vision Computing* 20.9-10 (2002), pp. 751–759 (cit. on p. 89).
- [159] R. C. G. D. Medeiros, J. D. Soares, and F. B. D. Sousa. “Natural enamel caries in polarized light microscopy: differences in histopathological features derived from a qualitative versus a quantitative approach to interpret enamel birefringence”. In: *Journal of Microscopy* 246.2 (2012), pp. 177–189 (cit. on p. 89).
- [160] J. Schindelin et al. “Fiji: an open-source platform for biological-image analysis”. In: *Nature Methods* 9.7 (2012), 676–682 (cit. on p. 90).

- [161] D. Hasler and S. Ssstrunk. “Mapping colour in image stitching applications”. In: *Journal of Visual Communication and Image Representation* 15.1 (2004), pp. 65–90 (cit. on p. 93).
- [162] J. Jang and J. Ra. “Pseudo-color image fusion based on intensity-hue-saturation color space”. In: *Proc. IEEE International Conference on Multisensor Fusion and Integration for Intelligent Systems (MFI 2008)*. Seoul, Korea, Aug. 20–22, 2008, pp. 366–371 (cit. on p. 93).
- [163] A. Toet and J. Walraven. “New false color mapping for image fusion”. In: *Optical Engineering* 35.650 (1996) (cit. on p. 93).
- [164] E. Zagrouba, W. Barhoumi, and S. Amri. “An efficient image-mosaicing method based on multifeature matching”. In: *Machine Vision and Applications* 20.3 (2009), pp. 139–162 (cit. on p. 93).
- [165] C. Tomasi and T. Kanade. “Detection and Tracking of Point Features”. In: *Carnegie Mellon University Technical Report CMU-CS-91-132* (1991) (cit. on p. 95).
- [166] S. Baker and I. Matthews. “Lucas-Kanade 20 years on: a unifying framework”. In: *International Journal of Computer Vision* 56.3 (2004), 221–255 (cit. on p. 95).
- [167] J.-Y. Bouguet. “Pyramidal implementation of the Lucas Kanade feature tracker: Description of the algorithm”. In: *Intel Research Laboratory Technical Report* (1999) (cit. on p. 96).
- [168] J. Zhang et al. “Image automatic mosaics based on contour phase correlation”. In: *Frontiers of Mechanical Engineering in China* 2.2 (2007), pp. 228–234 (cit. on pp. 96, 154).
- [169] S. Preibisch et al. “Bead-based mosaicing of single plane illumination microscopy images using geometric local descriptor matching”. In: *Proc. SPIE 2009*. Vol. 7259. Orlando, Florida, U.S.A., Feb. 7–12, 2009, 72592S–1–72592S–10 (cit. on p. 98).
- [170] M. A. Fischler and R. C. Bolles. “Random sample consensus: a paradigm for model fitting with applications to image analysis and automated cartography”. In: *Magazine Communications of the ACM* 24.6 (1981), pp. 98–117 (cit. on pp. 98, 156).
- [171] F. Winkelman and I. Patras. “Online globally consistent mosaicing using an efficient representation”. In: *Proc. IEEE International Conference on Systems, Man and Cybernetics (SMC 2004)*. Vol. 4. The Hague, The Netherlands, Oct. 10–13, 2004, pp. 3116–3121 (cit. on p. 101).
- [172] P. Azzari, L. D. Stefano, and A. Bevilacqua. “An effective real-time mosaicing algorithm apt to detect motion through background subtraction

- using a PTZ camera”. In: *Proc. IEEE Conference on Advanced Video and Signal Based Surveillance (AVSS 2005)*. Como, Italy, Sept. 15–16, 2005, pp. 511–516 (cit. on p. 101).
- [173] D.-W. Kim and K.-S. Hong. “Practical Background Estimation for Mosaic Blending with Patch-based Markov Random Fields”. In: *Pattern Recognition* 41.7 (2008), pp. 2145–2155 (cit. on p. 102).
- [174] W. Xu and J. Mulligan. “Performance Evaluation of Color Correction Approaches for Automatic Multi-view Image and Video Stitching”. In: *Proc. IEEE Computer Society Conference on Computer Vision and Pattern Recognition (CVPR 2010)*. San Francisco, CA, June 13–18, 2010, pp. 263–270 (cit. on p. 105).
- [175] P. Azzari and A. Bevilacqua. “Joint Spatial and Tonal Mosaic Alignment for Motion Detection with PTZ Camera”. In: *Proc. International Conference on Image Analysis and Recognition (ICIAR 2006)*. Vol. 4142. Póvoa de Varzim, Portugal, Aug. 18–Sept. 20, 2006, pp. 764–775 (cit. on p. 105).
- [176] L. Carozza. “Algorithms for On-Line Image Registration from Multiple Views”. PhD thesis. Via Toffano 2/2, 40125, Bologna, Italy: Advanced Research Center on Electronic Systems, University of Bologna, 2011 (cit. on pp. 121, 154).
- [177] L. Tessens et al. “Extending the Depth of Field in Microscopy Through Curvelet-Based Frequency-Adaptive Image Fusion”. In: *Proc. 32<sup>th</sup> IEEE International Conference on Acoustics, Speech and Signal Processing (ICASSP 2007)*. Vol. 1. Vienna, Austria, Apr. 15–20, 2007, pp. 861–864 (cit. on pp. 126, 128, 131, 133).
- [178] J. F. Brenner et al. “An automated microscope for cytologic research a preliminary evaluation”. In: *Journal of Histochemistry & Cytochemistry* 24.1 (1976), pp. 100–111 (cit. on pp. 126, 128).
- [179] L. Firestone et al. “Comparison of autofocus methods for automated microscopy”. In: *Cytometry* 12.3 (1991), pp. 195–206 (cit. on pp. 126, 128, 132).
- [180] H. Harms and H. M. Aus. “Comparison of digital focus criteria for a TV microscope system”. In: *Cytometry* 5.3 (1984), pp. 236–243 (cit. on p. 126).
- [181] N. Cvejic et al. “A novel metric for performance evaluation of image fusion algorithms”. In: *Proc. World Academy of Science, Engineering and Technology (WASET 2005)*. Vol. 7. Aug. 2005, pp. 80–85 (cit. on p. 126).

- [182] F. Aguet, D. van de Ville, and M. Unser. “Model-based 2.5-D deconvolution for extended depth of field in brightfield microscopy”. In: *IEEE Transactions on Image Processing* 17.7 (2008), pp. 1144–1153 (cit. on pp. 126, 130, 131, 137–139).
- [183] K. Itoh, A. Hayashi, and Y. Ichioka. “Digitized optical microscopy with extended depth of field”. In: *Applied Optics* 28.16 (1989), pp. 3487–3493 (cit. on p. 126).
- [184] A. Valdecasas et al. “On the extended depth of focus algorithms for bright field microscopy”. In: *Micron* 32.6 (2001), pp. 559–569 (cit. on pp. 126, 128, 132).
- [185] N. T. Goldsmith. “Deep focus; a digital image processing technique to produce improved focal depth in light microscopy”. In: *Image Analysis & Stereology* 19.3 (2000), pp. 163–167 (cit. on pp. 126, 128, 130, 141).
- [186] B. Forster et al. “Complex wavelets for extended depth-of-field: A new method for the fusion of multichannel microscopy images”. In: *Microscopy research and technique* 65.1–2 (2004), pp. 33–42 (cit. on pp. 127, 128, 130–133, 137–139).
- [187] A. Tesei et al. “Isolation of stem/progenitor cells from normal lung tissue of adult humans”. In: *Cell Proliferation* 42.3 (2009), pp. 298–308 (cit. on pp. 127, 138).
- [188] V. Tympel. “New high-level image capture system for conventional light microscopy”. In: *Proc. SPIE 1996 (SPIE 1996)*. Vol. 2707. Newport Beach, CA, U.S.A., Feb. 11, 1996, pp. 529–536 (cit. on p. 128).
- [189] A. A. Goshtasby and S. Nikolov. “Guest editorial: Image fusion: Advances in the state of the art”. In: *Information Fusion* 8.2 (2007), pp. 114–118 (cit. on p. 128).
- [190] T. Yeo et al. “Autofocusing for tissue microscopy”. In: *Image and Vision Computing* 11.10 (1993), pp. 629–639 (cit. on pp. 128, 132).
- [191] R. Pieper and A. Korpel. “Image processing for extended depth of field”. In: *Applied Optics* 22.10 (1983), pp. 1449–1453 (cit. on p. 128).
- [192] S. A. Sugimoto and Y. Ichioka. “Digital composition of images with increased depth of focus considering depth information”. In: *Applied Optics* 24.14 (1985), pp. 2076–2080 (cit. on p. 128).
- [193] P. J. Burt, K. Hanna, and R. J. Kolczynski. “Enhanced image capture through fusion”. In: *Proc. 4<sup>th</sup> International Conference on Computer Vision (ICCV 1993)*. Berlin, Germany, May 11–14, 1993, pp. 173–182 (cit. on p. 128).

- [194] H. Li, B. Manjunath, and S. Mitra. “Multisensor Image Fusion Using the Wavelet Transform”. In: *Graphical Models and Image Processing* 57.3 (1995), pp. 235–245 (cit. on pp. 128, 132).
- [195] Z. Liu et al. “Objective Assessment of Multiresolution Image Fusion Algorithms for Context Enhancement in Night Vision: A Comparative Study”. In: *IEEE Transactions on Pattern Analysis and Machine Intelligence* 34.1 (2012), pp. 94–109 (cit. on pp. 128, 134).
- [196] E. Blasch et al. “Image quality assessment for performance evaluation of image fusion”. In: *Proc. 11<sup>th</sup> International Conference on Information Fusion (FUSION 2008)*. Cologne, Germany, June 30–July 3, 2008, pp. 1–6 (cit. on pp. 128, 136).
- [197] Y. Chen and R. S. Blum. “A new automated quality assessment algorithm for image fusion”. In: *Image and Vision Computing* 27.10 (2009), pp. 421–432 (cit. on p. 128).
- [198] N. Cvejic, T. Seppanen, and S. J. Godsill. “A Nonreference Image Fusion Metric Based on the Regional Importance Measure”. In: *IEEE Journal of Selected Topics in Signal Processing* 3.2 (2009), pp. 212–221 (cit. on p. 128).
- [199] N. Cvejic et al. “A Similarity Metric for Assessment of Image Fusion Algorithms”. In: *International Journal of Signal Processing* 2.3 (2006), pp. 178–182 (cit. on pp. 129, 134).
- [200] M. A. Bueno et al. “Polychromatic image fusion algorithm and fusion metric for automatized microscopes”. In: *Optical Engineering* 44.9 (2005), pp. 093201.1–093201.7 (cit. on pp. 129, 134).
- [201] URL: <http://bigwww.epfl.ch/demo/edf> (cit. on p. 130).
- [202] URL: <http://rsbweb.nih.gov/ij/plugins/stack-focuser.html> (cit. on p. 130).
- [203] URL: <http://rsbweb.nih.gov/ij/plugins/depth-from-focus/> (cit. on p. 130).
- [204] E. Candés et al. “Fast Discrete Curvelet Transforms”. In: *Multiscale Modeling and Simulation* 5.3 (2006), pp. 861–899 (cit. on p. 131).
- [205] URL: [www.curvelet.org](http://www.curvelet.org) (cit. on p. 131).
- [206] E. Krotkov. “Focusing”. In: *International Journal of Computer Vision* 1.3 (1988), pp. 223–237 (cit. on p. 132).
- [207] M. Hossny, S. Nahavandi, and D. Creighton. “A Quadtree Driven Image Fusion Quality Assessment”. In: *Proc. 5<sup>th</sup> IEEE International Conference on Industrial Informatics (INDIN 2007)*. Vol. 1. Vienna, Austria, June 23–27, 2007, pp. 419–424 (cit. on p. 136).

- [208] M. Hossny, S. Nahavandi, and D. Crieghton. “Feature-Based Image Fusion Quality Metrics”. In: *Proc. 1<sup>st</sup> International Conference Intelligent Robotics and Applications (ICIRA 2008)*. Vol. 5314. Wuhan, China, Oct. 15–17, 2008, pp. 469–478 (cit. on p. 136).
- [209] URL: <http://www.ux.uis.no/~tranden/brodatz.html> (cit. on pp. 136, 137).
- [210] S. F. Gibson and F. Lanni. “Experimental test of an analytical model of aberration in an oil-immersion objective lens used in three-dimensional light microscopy”. In: *Journal of the Optical Society of America A* 9.1 (1992), pp. 154–166 (cit. on p. 144).
- [211] F. Piccinini et al. “Extended depth of focus in optical microscopy: assessment of existing methods and a new proposal”. In: *Microscopy Research and Technique* 75.11 (2012), pp. 1582–1592 (cit. on pp. 147, 148).
- [212] F. Piccinini et al. “Extending the Universal Quality Index to assess N-image fusion in light microscopy”. In: *International Journal of Bioelectromagnetism* 14.4 (2012), pp. 217–222 (cit. on p. 147).
- [213] C. D. Kuglin and D. C. Hines. “The phase correlation image alignment method”. In: *Proc. IEEE International Conference on Cybernetics and Society*. New York, NY, U.S.A., 1975, 163–165 (cit. on p. 153).
- [214] E. De-Castro and C. Morandi. “Registration of translated and rotated images using finite Fourier transforms”. In: *IEEE Transactions on Pattern Analysis and Machine Intelligence* 9.5 (1987), pp. 700–703 (cit. on p. 154).
- [215] Y. Keller, A. Averbuch, and M. Isreali. “Pseudo-polar based estimation of large translations rotations and scalings in images”. In: *IEEE Transactions on Image Processing* 14.1 (2005), pp. 12–22 (cit. on p. 154).
- [216] H. Foroosh, J. Zerubia, and M. Berthod. “Extension of phase correlation to subpixel registration”. In: *IEEE Transactions on Image Processing* 11.3 (2002), pp. 188–200 (cit. on p. 154).



# Personal publications

## Journal Articles:

1. Z. Bulj, S. Duchi, A. Bevilacqua, A. Gherardi, B. Dozza, F. Piccinini, G. A. Mariani, E. Lucarelli, S. Giannini, D. Donati and S. Marmioli, Protein kinase B/AKT isoform 2 drives migration of human mesenchymal stem cells. *International Journal of Oncology*, Vol. 42, Num. 1, January 2013, pp. 118-126
2. F. Piccinini, A. Tesei, W. Zoli and A. Bevilacqua, Extending the Universal Quality Index to assess N-image fusion in light microscopy. *International Journal of Bioelectromagnetism*, Vol. 14, Num. 4, December 2012, pp. 217-222
3. F. Piccinini, A. Tesei, W. Zoli and A. Bevilacqua, Extended depth of focus in optical microscopy: assessment of existing methods and a new proposal. *Microscopy Research and Technique*, Vol. 15, Num. 11, November 2012, pp. 1582-1592
4. F. Piccinini, E. Lucarelli, A. Gherardi and A. Bevilacqua, Multi-image based method to correct vignetting effect in light microscopy images. *Journal of Microscopy*, Vol. 248, Num. 1, October 2012, pp. 6-22

## Conference Proceedings:

1. F. Piccinini, A. Bevilacqua, K. Smith and P. Horvath, Vignetting and photo-bleaching correction in automated fluorescence microscopy from an array of overlapping images. Accepted to the 10th IEEE International

- Symposium on Biomedical Imaging (ISBI), San Francisco, CA, USA, April 7-11, 2013
2. A. Bevilacqua and F. Piccinini, Is an empty field the best reference to correct vignetting in microscopy? In Proceedings of the 7th International Workshop on Biosignal Interpretation (BSI), Como, Italy, July 2-4, 2012, pp. 267 - 270
  3. L. Carozza, A. Bevilacqua and F. Piccinini, Mosaicing of Optical Microscope Imagery Based on Visual Information. In Proceedings of the 33rd Annual International Conference of the IEEE Engineering in Medicine and Biology Society (EMBS), Boston, USA, August 30 - September 3, 2011, pp. 6162 - 6165
  4. A. Bevilacqua, F. Piccinini and A. Gherardi, Vignetting correction by exploiting an optical microscopy image sequence. In Proceedings of the 33rd Annual International Conference of the IEEE Engineering in Medicine and Biology Society (EMBS), Boston, USA, August 30 - September 3, 2011, pp. 6166 - 6169
  5. A. Gherardi, A. Bevilacqua and F. Piccinini, Illumination field estimation through background detection in optical microscopy. In Proceedings of the 8th annual IEEE Symposium on Computational Intelligence in Bioinformatics and Computational Biology (CIBCB), Paris, France, April 11-15, 2011, pp. 49 - 54
  6. L. Carozza, A. Bevilacqua and F. Piccinini, An Incremental Method for Mosaicing of Optical Microscope Imagery. In Proceedings of the 8th annual IEEE Symposium on Computational Intelligence in Bioinformatics and Computational Biology (CIBCB), Paris, France, April 11-15, 2011, pp. 55 - 60
  7. S. Lazzari, A. Barletta, E. Magyari and F. Piccinini, Dual solutions for viscous mixed convection flows in a vertical circular duct: a numerical benchmark. In Proceedings of the European Comsol Conference 2007, Grenoble (Paris), France, October 23-24, 2007, pp. 343 - 349

# Thanks

Many people contributed to the work of this thesis and in general supported me in these years, helping me when I needed a hand and being happy for me every time I reached an objective. It would be impossible to create a list where all the names of the people my heart would like to thank are included. Nevertheless, I want to say a few words about some of you that have been really important in some moments of my life.

**Alessandro Bevilacqua**, you gave me the opportunity to pursue a career in a fascinating research environment and you guided me in exploring the frontiers of the scientific knowledge. With your great expertise, you mentored me in every step of my PhD, sharing my joy for every result and being of fundamental help in the difficulties. Your perspectives and ideas constantly made the research activity really challenging. I thank you for your supervision: whatever I learned in my work is thanks to you, and now, thanks to your teachings, I have a great dream for my future. Moreover, I thank **Alessandro Gherardi** and **Silvia Malavasi**, my colleagues, that have always been ready to help, contributing to create a pleasant atmosphere and to promote productivity.

**Mauro Ursino**, my co-supervisor, an important, kind and willing person. I think that you should be an example for every young researcher. Your university lessons are always fascinating and perfectly clear, and your suggestions are always balanced and useful. I remember with pleasure the week we spent together in Boston for a conference. I really have to thank you, because your presence and your suggestions have been important to me since my master thesis. I also thank two other Professors I met during the courses of Biomedical Engineering: **Emanuele Domenico Giordano**, a really kind person. I hope in the future to have the opportunity to work and share projects with Emanuele. **Stefano Lazzari**, supervisor of my bachelor thesis. I shared with

you many moments of my life that I will never forget. In particular I will remember forever the day when you told me what was the name you had chosen for your son. I wish the best for you, **your wife** and **Filippo**, your son (and also **Matteo** just arrived!)

**Enrico Lucarelli**, the first person I met after the university lessons and that showed me what to be a researcher means. Enrico you are is a fantastic person with knowledge, tactfulness and understanding. You were the one that first taught me the basics of biology and group working. My way of doing research has been oriented from your teachings. I really thank you: you are an important person for my life, maybe much more than you think. Moreover, I thank **Barbara Dozza**, **Michela Pierini**, **Serena Duchi**, **Zrinka Buji**, **Elisa Martella** and **Chiara Bellotti**, people that have always been kind with me. I also thank another person of the laboratory, **Panagiota Dimopoulou**. Since the first moment I saw you I have had a friendly feeling: you are a person with a very big heart. I wish for you, **Marcello** and **Dimitris** all the best of this life!

**Peter Horvath**, a very nice person I met and that I hope I will never lose contact with! Peter, you are an example for me, you are one of the most intelligent and hard-working people I know. I shared with you around seven months of my life during my staying in Zurich and I really think that you are a genius. Now you are very young, but I hope you will soon become a Professor in an important University. You are an example for me, but a friend as well. I also thank **Gábor Csúcs**, **Kevin Smith**, **Justine Kusch**, **Csaba Balazs**, **Andreas Kaufmann**, **Tobias Schwarz**, **Joachim Hehl** and **Michael Stebler**, very smart people whom I am proud to have met.

**Anna Tesei**, **Rolando Polico**, **Wainer Zoli**, **Anna Sarnelli**, **Sara Bravaccini**, **Chiara Arienti**, **Sara Pignatta**, **Giulia Paganelli**, **Francesca Ceroni**, **Lucia Bandiera** and **Alice Pasini**, people I'm meeting now during a new project and with whom I will be happy to work in the years to come.

Now a short overview of the friends who have been with me for a lifetime: **Nicolas Bandini**, **Marco Lucchi**, **Marco Donati**, **Davide Angeli**, **Denis Di Paolo**, **Massimo Geminiani**, **Gianluca Tassinari**, **Nicola Garavini**, **Matteo Farinelli**, **Andrea Montanari**, **Loris Berti**, **Mattia Ricci**, **Filippo Fanti**, **Pierfrancesco Bassetti**, **Andrea Cantore**, **Andrea Ghetti**,

**Alberto Cavina, Emanuele Ciani, Alberto Amadio, Francesco Sbarzaglia and Angelica and Giulio, Raffaele Vassura and Veronica, Filippo Caranti and Giulia, Mattia Verbeni e Gaia, Manuel Varoli and Gaia, Roberto Montevecchi and Antonia, Nicola Fabbri and Elena, Lucilla Galanti and Manuel, Federica Sartoni, Ludovica Flamini, Antonella Dotti, Roberta Casadio, Elisabetta Calderoni, Silvia Castellari, Monica Raccagni, Alessandra Andaló, Elena Carosi, Chiara Canuti, Alice Rondinini, Mattia Tassinari, Maicol Cavina, Carlo Mosca, Mirco Magnani, Patrik Assirelli, Alberto Bedeschi, Marco Vignoli, Simone Vignodelli, Gabriele Cornacchia, Davide Ricci, Davide Lasi, Ludovico Carozza, Valentina D'Angeli, Claudia Spagnolo, Maria Luigia Colucci, Ilenia De Padova, and Valentina Rossetti**, a very good friend with whom I shared a wonderful house in Zurich for around seven months.

Here I list another group of friends with different characteristics: funny **Camilla** and **Carriola**, loving **Robertone**, studious **Anacleto**, proud **Champagne**, the intelligent **Ramulis**.

I also thank my neighbors **Lilli, Maria** and **Giordano, Lisa** and **Aurelio, Lele** and his **wife**, the **Ragnis**, because we are like a big family.

Then I thank all **my relatives**, in particular my aunts **Paola, Fiorella, Floriana, Alessandra, Federica**, my uncles **Giorgio, Graziano, Andrea, Massimiliano, Maurizio**, my cousins **Alan, Sarah, Carolina** and **Federica**, with whom I am lucky to live near.

Finally, I thank three people that have a special place in my heart.

**Alessandra**, who is sharing with me his life. You are the most beautiful thing I have.

**My mother** and **my father**. What I am is thanks to you. I thank you for every day, every effort, every hug of your lives. Remember that you will stay with me forever because you will always be with me in my heart.

Finally, I thank all of you that trust me and are my strength...

6. *Thanks*

---

*As every year, to conclude the concert*

*Radetzky March of Johann Strauss I*

(in memory of Arturo Piccinini)

# THESIS END

## **Filippo Piccinini**

Biomedical Engineer

PhD in Information Technology (2010-2012)

Master's degree in Biomedical Engineering (2009, 110/110 Cum Laude)

Bachelor's degree in Biomedical Engineering (2007, 110/110 Cum Laude)

E-mail: [f.piccinini@unibo.it](mailto:f.piccinini@unibo.it); [piccila@libero.it](mailto:piccila@libero.it)

Research group website: <http://cvg.deis.unibo.it>

Personal website: [www.filippopiccinini.altervista.org](http://www.filippopiccinini.altervista.org)

(Curriculum Vitae available on the personal website)

### **Office address:**

Via Toffano 2/2, IT-40125, Bologna, Italy

### **Home address:**

Via Pola 6/2, IT-48018, Faenza (RA), Italy